論文 / 著書情報
Article / Book Information

題目(和文)	
Title(English)	Influence of Calcium Phosphate Coatings on Corrosion Resistance, Biocompatibility and Mechanical Integrity of Mg-Zn-Zr alloy
著者(和文)	Le Thi Trang
Author(English)	Le Thi Trang
出典(和文)	学位:博士(工学), 学位授与機関:東京工業大学, 報告番号:甲第12549号, 授与年月日:2023年9月22日, 学位の種別:課程博士, 審査員:小林 郁夫,史 蹟,藤居 俊之,多田 英司,村石 信二
Citation(English)	Degree:Doctor (Engineering), Conferring organization: Tokyo Institute of Technology, Report number:甲第12549号, Conferred date:2023/9/22, Degree Type:Course doctor, Examiner:,,,,
学位種別(和文)	博士論文
Type(English)	Doctoral Thesis

DOCTORAL THESIS

Influence of Calcium Phosphate Coatings on Corrosion Resistance, Biocompatibility and Mechanical Integrity of Mg-Zn-Zr alloy

LE THI TRANG

Department of Materials Science and Engineering

Tokyo Institute of Technology

2023

Table of Contents

Chapter 1:

General Introduction

1.1. Background of metallic biomaterials

Orthopedic implant devices, or fracture management and joint replacement devices, include wires, screws, pins, plates and other artificial ligaments. Their functions are to support bones to bear loads and to promote the bone healing process so that patients can turn back to normal life. Over the last decades, the rising of human demand for implants, which is a main result of aging population, makes it essential to accelerate the evolution of biomaterials.

From materials science view, there were four primary classifications of biomaterials: metals, ceramics and polymers and composites. Among these groups, metallic biomaterials usually prefer to be applicable for load-bearing implantation due to their outstanding mechanical properties and machinability through various production methods (casting, machining, extrusion and others) [1].

Three generation have been developed throughout the evolution of metallic biomaterials [2]. The emergence of new generations does not eliminate the previous one. In fact, they are all further developed to meet different practical purposes and requirements.

The first generation (1-gen) contains bioinert materials which basically replace damaged tissues [2]. Stainless steel, titanium (Ti)-based alloys, and cobalt-chromium (Co-Cr) alloys are three typical alloy systems of the 1-gen biomaterials. Bioactive materials, as the second generation (2-gen), are those can interact with host tissue to improve biological responses [2]. However, during the time that the 2-gen materials are designed, none of the base metallic materials are bioactive. Hence, in this generation, various bioactive coatings (bioactive glasses, polymers, calcium phosphate compounds, etc.), accompanies with coating techniques, are mainly studied.

During the development for the long-term orthopedic implantation, the 1-gen and 2-gen biomaterials have shown two serious limitations: the need for removal surgeries and the occurrence of the stress shielding effect. Stainless steel, Ti alloys and Co-Cr alloys are bioinert materials because those materials have significantly high corrosion resistance. It means that those implant materials will stay permanently in human body. After the fractured bone is healed completely, the existence of the implant, as a foreign body, cause persistent pain for patients in the implanted region [3]. Therefore, secondary surgery for implant removal is needed after bone fixation. This removal surgery causes pain, economic-cost and infection for patients [4]. In addition, the long-term implantation of those alloy systems also leads to the occurrence of the stress shielding effect due to a huge mismatch in elastic modulus between the implant material and human bone, see Table 1.1 [5]. The stress shielding effect reduces stimulation of new bone growth and remodeling and may lead to osteoporosis in a long-term usage [5], [6]. A minor limitation of those current metallic

biomaterials is the possibility of releasing toxic metallic ions and/or particles due to corrosion or wear processes although they are high wear and corrosion resistance alloys [7]. This may lead to inflammatory cascades which reduce biocompatibility and cause tissue loss [5].

To overcome one of the limitations of the existing metallic biomaterials, the third generation (3-gen) shifts to biodegradable metals. The term "biodegradable" and "biodegradability" describes the ability to self-dissolve in the biological environment. The 3-gen biomaterials are ideally expected to degrade gradually in the physiological environment while still supporting the healing tissues for bearing forces; at the same time, the loss of the implant is replaced by the new tissues [2]. The characteristic materials of this generation include magnesium (Mg) alloys, iron (Fe) alloys and zinc (Zn) alloys because the base metals of those alloys can be degraded in the corrosive environment [8], [9].

Table 1.1: Density and mechanical properties of various implant materials in comparison to human bone [5].

Properties	Human bone	Mg alloys	Ti alloys	Co-Cr alloys	Stainless steels
Density (g/cm^3)	1.8 – 2.1	1.74 – 2.0	4.4 – 4.5	8.3 – 9.2	7.9 – 8.1
Elastic modulus (GPa)	3 – 20	41 – 45	110 – 117	230	189 – 205
Compressive yield strength (MPa)	130 – 180	65 – 100	758 – 1117	450 – 1000	170 – 310
Fracture toughness (MPa.m$^{1/2}$)	3 – 6	15 – 40	55 – 115	N/A	50 – 200

In the 3-gen biomaterials, Mg-based alloys have been the most attractive biomaterial for temporary implant devices owing to their outstanding properties. Mg alloys are dissolved in the physiological environment due to the highly negative electrochemical potential (-2.37 V) of Mg metal [10]. It means Mg-based implants are biodegradable, leading to the unnecessity of the implant-removal surgery. This notably decreases the medical cost and burden to the patients. Furthermore, Mg alloys possess a relatively low density (ρ = 1.74 – 2 g/cm^3) and high specific strength with a low elastic modulus (E = 41 – 45 GPa), which was close to those values of human bone, i.e., ρ = 1.8 – 2.1 g/cm^3 and E = 3 – 20 GPa; respectively [5]. This similarity prevents the occurrence of the stress shielding effect, which cause concerns in the long-term usage of the 1-gen metallic biomaterials. The comparison of density and elastic modulus of the 1-gen, Mg-based

materials and human bone is shown in Table 1.1. In addition, the Mg element is a well-known biocompatible metal, which plays an essential role in human body since Mg^{2+} ions are involved in many metabolic reactions and biological mechanisms [11]. So far there are no reports on toxic reactions caused by the excessive amount of Mg [11]. Also, Mg metal itself was shown to simulate the new bone formation since its ions enhance the attachment and proliferation of cells, and new bone was observed to be formed in direct contact with Mg [12]. Generally, the use of Mg alloys is expected to cause non-toxic reactions and might overcome the two major problems (the removal surgery and the stress shielding effect) that are caused by the 1-gen biomaterials. Therefore, Mg alloys are prospective metallic biomaterials for temporary load-bearing implants.

1.2. Development of Magnesium alloys for implant materials

Owning to its hexagonal close packed structure with limited slip systems, their mechanical properties of pure Mg is under requirement for load-bearing implant devices, as shown in Table 1.1. As the result, alloying elements have been introduced into the Mg matrix to improve its mechanical properties and; also, its corrosion resistance. The challenge for the element selection in developing biological Mg alloys is considerations of both elemental toxicity and strengthening ability.

Based on toxicity level, alloying elements are classified into [13]:

- Toxic elements: Be, Ba, Pb, Cd, Th
- Elements that might cause hepatotoxicity or allergic problems: Al, V, Co, Cr, Ni, Cu
- Nutrient elements in human: Ca, Mn, Zn, Sn, Si
- Nutrient elements in plants and animals: Al, Bi, Li, Ag, Sr, Zr

Based on strengthening ability, alloying elements are classified into [13], [14]:

- Impurities: Fe, Cu, Ni, Co
- Elements that improve strength: Al, Zn, Ca, Ag, Ce, Ni, Cu, Th, Zr
- Elements that improve ductility: Th, Zn, Ag, Ce, Ca, Al, Ni, Cu

From these classifications, several Mg-based alloys developed for biomedical uses are Mg-Zn-based, Mg-Si-based, Mg-Zr-based and Mg-RE-based and so on [13]. Among those alloy systems, Mg-RE-based alloys normally exhibit the highest strength and elongation; also, their corrosion is commonly the lowest [13]. Though, rare earth elements are concerned with their effect on human health regarding cytotoxicity [15]. On the other hand, Mg-Zn-based alloys are highly potential biomaterials thanks to their second highest strength and ductility [13].

In Mg-Zn-based alloy system, Mg-Zn-Zr (ZK) series stands out as a potential candidate for orthopedic applications due to the two major advantages. Firstly, the alloy elements are biocompatible. As mentioned above, Zn is an essential nutrient element found in human muscle and bone [16]. Although Zn is a nutrient element in plant, histological and cytological studies proved that Zr showed good biocompatibility with an amount less than 0.8 wt% in Mg alloys [17], [18]. Therefore, the release of alloying ions, as a result of the corrosion reactions, may cause no harm or any of clinical diseases. Additionally, numerous studies showed that ZK series alloys own a good biocompatible property [19], [20]. Secondly, this alloy owns desirable mechanical properties for load-bearing applications. Both Zn and Zr are indicated to be a powerful grain finer to improve both strength and ductility of Mg alloys [13].

Mg-6 wt%-0.5 wt%Zr (ZK60) alloy is a well-known alloy in Mg-Zn-Zr series due to its high strength and ductility and extruded alloy shows even better mechanical properties. Also, this alloy has become commercially for the industrial command. Therefore, extruded ZK60 alloy is selected to be a substrate for further investigation in this study.

1.3. Corrosion behavior of Magnesium alloys

Mg alloys have been extensively considered as biodegradable materials for orthopedic implantation because of their similar mechanical properties to natural bone, good biocompatibility and lower densities compared to other metallic biomaterials. However, throughout the history of Mg and its alloys, although Mg wires were first applied to stop bleeding vessels of human patients in 1878 by Edward C. Huse [12], until now Mg-based implant materials have not been clinically used worldwide because the problem of controlling the corrosion of this material *in vivo* has not been sufficiently solved. This is the principal drawback of Mg alloys that limits their applications in biological use.

1.3.1. Corrosion mechanism

There are two main reasons leading to the poor corrosion resistance of Mg-based materials. Firstly, Mg metal is very chemically active owing to its highly electronegative potential allowing corrosion to occur even in conditions lack of oxygen. Secondly, the nature quasi-passive $MgO/Mg(OH)_2$ film on Mg also has a poor corrosion protectiveness, especially in a dilute chlorine solution.

In physiological conditions, the degradation of Mg and its alloys occur under the form of the electrochemical reactions. Typically, immediately after exposed to the moisture/body fluids, Mg is

oxidized randomly over the entire surface to form Mg^{2+} ions following the anodic reaction (1.1). The reduction reaction of water is then proceeded by the generation of electrons as shown in the cathodic reaction (1.2). These electrochemical reactions result in the formation of a $Mg(OH)_2$ layer on the surface of the Mg implant material, following the overall reaction (1.3). However, this layer is only stable in the highly alkaline solutions of pH≥11 [21]. In the physiological environment, the pH value of body fluid is just about ±7.4. Furthermore, the body fluid also contains a high amount of chlorine (Cl^-) ions (~104mmol/L) [21]. Therefore, the $Mg(OH)_2$ layer is very susceptible to breakdown by the Cl^- ions, as shown in reaction (1.4). Subsequently, the dissolution of this hydroxide layer decreases the protected areas, exposes the active Mg surface and then promotes further corrosion of Mg.

$$Mg \rightarrow Mg^{2+} + 2e^- \text{ (anodic reaction)} \quad (1.1)$$

$$2H_2O + 2e^- \rightarrow 2OH^- + H_2 \text{ (cathodic reaction)} \quad (1.2)$$

$$Mg + 2H_2O \rightarrow Mg(OH)_2 + H_2 \text{ (overall reaction)} \quad (1.3)$$

$$Mg(OH)_2 + 2Cl^- \rightarrow MgCl_2 + 2OH^- \quad (1.4)$$

1.3.2. Corrosion types

Because even in high-purity Mg, impurities (Fe, Cu, Ni, etc.) are always present and in Mg alloys, not only impurities but also second phases/intermetallic compounds of Mg with alloying elements are present, localized corrosion will take place instead of uniform corrosion. Some typical localized corrosion types in biological applications are reviewed as the follows:

Galvanic corrosion of Mg alloys is the primary issue for orthopedic applications. This corrosion occurs when there is a difference in electrochemical potentials of two contacted metals/phases. In the galvanic cells, Mg is always an active anode owing to its low negative electrochemical potential. Impurities and second phases/intermetallic compounds act as stable cathodes. In ZK series alloys, the second phases/intermetallic compounds include mainly Mg_xZn_y and few Zn_nZr_m [22]. Hence, Mg is preferential corroded.

Pitting is another form of localized corrosion which is associated with the breakdown of passivation layer in corrosive environment. When Mg alloys are exposed to a Cl^--containing solution, after the occurrence of the galvanic corrosion, a corrosion pit grows in a hemi-spherical direction [23].

Filiform is also a localized corrosion that occurs on the metal surface having an applied protective coating. It is caused by active galvanic cells and can propagate the whole surface, leading to detachment of the coating [23]. Filiform is accompanied with the occurrence of pitting corrosion.

Stress corrosion cracking (SCC), a form of localized corrosion, takes place due to the combination of susceptible materials under adequate stress, especially under constant stress. This type of corrosion damage is extremely dangerous since SCC causes slow, sub-critical crack growth under mechanical loads. SCC can be initiated by pitting since the pitting tips can act as stress magnifiers. When the crack reaches its critical size, a sudden and fast fracture can take place due to crack propagation under the applied stress [24]. This leads to an unexpected failure of the implant materials.

1.3.3. Negative impacts of corrosion in biological use

The subsequent impacts resulting from the corrosion of Mg materials cause some serious concerns in the biomedical use of Mg-based materials. Those negative impacts are described as follows:

a. Hydrogen gas evolution:

According to the overall corrosion reaction (1.3) of Mg materials, the dissolution of Mg metal is always coupled with the generation of hydrogen (H_2) gas. The H_2 gas is proved to exchange through the skin and/or accumulate in fatty tissue [25]. However, once the hydrogen saturation becomes exceeded, the generated gas then locally builds up in the tissue cavities or gas cavities [26]. In the subcutaneous implantation of porous pure Mg in rats, the excessive H_2 gas caused massive emphysema, prolonged discomfort and even decreased the survival rate of the rats [27]. The subcutaneous gas cavities can be punctured out, but this method may not be applicable for the internal surgeries [27]. Moreover, pressure created by the excessive H_2 evolution creates induces some mechanical disturbances of the bone generation, resulting in more severe foreign body reactions [28]. On the other hand, another implantation study in mice proved that toxicity of the gas cavities caused by the degradation of Mg and its alloys may not be an insurmountable problem in the clinical use since H_2 was exchanged quickly after implantation [25]. These contradictable results may not persuade surgeons to use Mg alloys in the practical case.

b. Rapid alkaline change:

The second concern of Mg alloys is the strong alkaline shift near the surface of the implant because of the OH^- generation when Mg degrades, shown in reaction (1.2 or 1.4). Human body maintains pH condition at 7.4-7.6; hence the local pH increase may be considered undesirable.

Although the physiological pH condition may be automatically adjusted to some extent, the rapid pH rise due to the fast corrosion of Mg alloys may lead to an alkaline poisoning effect when pH exceeds 7.8 in that region [29]. Also, it is proved that the cell density decreased with an increase of pH value of the culturing medium [30].

c. **Loosen of mechanical integrity**:

Another concern relevant to the dissolution of Mg alloys is the deterioration of mechanical integrity of the implant under prolonged mechanical loads. The implant material is supposed to support the fractured bone to bear loads during the healing process. During human daily activities, the produced mechanical loads accelerate the deterioration process because both corrosion and stress are present [31]. This leads to the occurrence of stress corrosion cracking (SCC). As mentioned above, SCC causes a sudden and fast failure of the implant. This unpredictable destruction reduced the feasibility of Mg alloys.

1.4. Strategies to reduce corrosion of ZK series alloy

To avoid the occurrence of the mentioned negative consequences following the corrosion of the Mg implant, control of the degradation rate is extremely necessary. The applied controlling methods include alloying addition, plastic deformations, heat treatment and surface modification. In numerous studies, not only the individual method but also the combination of those methods is investigated to provide an optimizing routeway to enhance effectively the corrosion resistance of ZK series alloys.

The mechanism of the alloying addition, plastic deformation and heat treatment methods for reducing corrosion rate is basically to change grain size and second phases inside the materials. It is well-known that a decrease in grain size improves mechanical properties through the Hall-Petch equation [32]. Hence, it is desired that decreasing grain size also improves corrosion resistance. However, the effects of grain size on controlling corrosion rate is more complicated and controversial among reports where some stated decrease in grain size improves corrosion resistance and some stated oppositely [33]. In addition, the effect of the second phases regards galvanic corrosion formed between the second phases and the corroded Mg matrix. Either an increase in the potential difference between the second phases and the matrix or an increase in the second phase fraction provide more active galvanic cells, resulting in higher corrosion rate [33]. The size and distribution of the second phase also play an important role in controlling corrosion rate but the mechanism of those factors has not been understood clearly [34], [35]. Generally, the influence of the intrinsic change caused by these three methods is complicated and varies among reports.

Surface modification is more simple and effective method to reduce corrosion rate. The mechanism of this method is to provide a protective layer on the material surface to prevent corrosion, especially at the beginning stages after the implantation. Moreover, applying a biocompatible coating might integrate better into local tissues and improve clinical performance. Among a majority of biocompatible coatings, calcium phosphate coatings stands out attractively because these coating materials also show osseointegration and osteoconduction [36]. Calcium phosphate is a family includes a great number of minerals consisting Ca and PO_4 in their chemical structure. Some of the calcium phosphate phases that applied often as a coating in orthopedic devices are given in Table 1.2 [36]. Although in the same family, the calcium phosphate phases differ in characteristic, chemical formula, solubility; consequently, biological response of the host tissue.

Due to the effective corrosion protection and excellent biocompatibility, calcium phosphate surface treatment is selected to be applied to control the corrosion rate of ZK60 alloy in this study.

Table 1.2: Common types of calcium phosphate coatings used in orthopedic implantation [36].

Name	Formula	Ca/P ratio
Hydroxyapatite (HAp)	$Ca_{10}(PO_4)_6(OH)_2$	1.67
Octcalcium phosphate (OCP)	$Ca_8H_2(PO_4)_6.5H_2O$	1.33
Calcium phosphate dihydrate (brushite)	$CaHPO_4.2H_2O$	1.0
Anhydrous calcium phosphate (monetite)	$CaHPO_4$	1.0
Tricalcium phosphate (TCP)	$Ca_3(PO_4)_2$	1.5
Fluorapatite	$Ca_{10}(PO_4)_6F_2$	1.67

1.5. Objectives of this thesis

To sum up, though ZK60 alloy has good biocompatibility and strength, its corrosion resistance is under concerned for load-bearing implantation. Hence, calcium phosphate coating layer is selected to improve its poor corrosion resistance.

The objectives of this doctoral thesis are described as follows:

(1) Surface modification for ZK60 alloy by several calcium phosphate coatings and investigation of their corrosion behavior

(2) Investigate *in vitro* and *in vivo* biocompatibility of coated samples through cell culture tests and animal tests (rabbit model)

(3) Evaluate mechanical intergrity of coated ZK60 samples after different time periods of corrosion

References

[1] N. Sezer, Z. Evis, S.M. Kayhan, A. Tahmasebifar, M. Koç, Review of magnesium-based biomaterials and their applications, Journal of Magnesium and Alloys. 6 (2018) 23–43. https://doi.org/10.1016/j.jma.2018.02.003.

[2] L.L. Hench, J.M. Polak, Third-Generation Biomedical Materials, Science. 295 (2002) 1014–1017. https://doi.org/10.1126/science.1067404.

[3] R.B. Minkowitz, S. Bhadsavle, M. Walsh, K.A. Egol, Removal of painful orthopaedic implants after fracture union, J Bone Joint Surg Am. 89 (2007) 1906–1912. https://doi.org/10.2106/JBJS.F.01536.

[4] H. Zhou, B. Liang, H. Jiang, Z. Deng, K. Yu, Magnesium-based biomaterials as emerging agents for bone repair and regeneration: from mechanism to application, Journal of Magnesium and Alloys. 9 (2021) 779–804. https://doi.org/10.1016/j.jma.2021.03.004.

[5] M.P. Staiger, A.M. Pietak, J. Huadmai, G. Dias, Magnesium and its alloys as orthopedic biomaterials: A review, Biomaterials. 27 (2006) 1728–1734. https://doi.org/10.1016/j.biomaterials.2005.10.003.

[6] J. Nagels, M. Stokdijk, P.M. Rozing, Stress shielding and bone resorption in shoulder arthroplasty, J Shoulder Elbow Surg. 12 (2003) 35–39. https://doi.org/10.1067/mse.2003.22.

[7] J.J. Jacobs, J.L. Gilbert, R.M. Urban, Current Concepts Review - Corrosion of Metal Orthopaedic Implants*, JBJS. 80 (1998) 268. https://journals.lww.com/jbjsjournal/Citation/1998/02000/Current_Concepts_Review___Corrosion_of_Metal.15.aspx (accessed April 17, 2023).

[8] G. Li, H. Yang, Y. Zheng, X.-H. Chen, J.-A. Yang, D. Zhu, L. Ruan, K. Takashima, Challenges in the use of zinc and its alloys as biodegradable metals: Perspective from biomechanical compatibility, Acta Biomaterialia. 97 (2019) 23–45. https://doi.org/10.1016/j.actbio.2019.07.038.

[9] R. Gorejová, L. Haverová, R. Oriňaková, A. Oriňak, M. Oriňak, Recent advancements in Fe-based biodegradable materials for bone repair, J Mater Sci. 54 (2019) 1913–1947. https://doi.org/10.1007/s10853-018-3011-z.

[10] A. Atrens, M. Liu, N.I. Zainal Abidin, Corrosion mechanism applicable to biodegradable magnesium implants, Materials Science and Engineering: B. 176 (2011) 1609–1636. https://doi.org/10.1016/j.mseb.2010.12.017.

[11] G. Song, S. Song, A Possible Biodegradable Magnesium Implant Material, Advanced Engineering Materials. 9 (2007) 298–302. https://doi.org/10.1002/adem.200600252.

[12] F. Witte, The history of biodegradable magnesium implants: A review, Acta Biomaterialia. 6 (2010) 1680–1692. https://doi.org/10.1016/j.actbio.2010.02.028.

[13] Y. Chen, Z. Xu, C. Smith, J. Sankar, Recent advances on the development of magnesium alloys for biodegradable implants, Acta Biomaterialia. 10 (2014) 4561–4573. https://doi.org/10.1016/j.actbio.2014.07.005.

[14] R. Kumar, P. Katyal, Effects of alloying elements on performance of biodegradable magnesium alloy, Materials Today: Proceedings. 56 (2022) 2443–2450. https://doi.org/10.1016/j.matpr.2021.08.233.

[15] A.A. Brouziotis, A. Giarra, G. Libralato, G. Pagano, M. Guida, M. Trifuoggi, Toxicity of rare earth elements: An overview on human health impact, Frontiers in Environmental Science. 10 (2022). https://www.frontiersin.org/articles/10.3389/fenvs.2022.948041 (accessed May 16, 2023).

[16] L.M. Plum, L. Rink, H. Haase, The Essential Toxin: Impact of Zinc on Human Health, International Journal of Environmental Research and Public Health. 7 (2010) 1342–1365. https://doi.org/10.3390/ijerph7041342.

[17] K. Kumar, R.S. Gill, U. Batra, Challenges and opportunities for biodegradable magnesium alloy implants, Materials Technology. 33 (2018) 153–172. https://doi.org/10.1080/10667857.2017.1377973.

[18] S. Ghosh, A. Sharma, G. Talukder, Zirconium. An abnormal trace element in biology, Biol Trace Elem Res. 35 (1992) 247–271. https://doi.org/10.1007/BF02783770.

[19] Z.G. Huan, M.A. Leeflang, J. Zhou, L.E. Fratila-Apachitei, J. Duszczyk, In vitro degradation behavior and cytocompatibility of Mg–Zn–Zr alloys, J Mater Sci: Mater Med. 21 (2010) 2623–2635. https://doi.org/10.1007/s10856-010-4111-8.

[20] X.N. Gu, N. Li, Y.F. Zheng, L. Ruan, In vitro degradation performance and biological response of a Mg–Zn–Zr alloy, Materials Science and Engineering: B. 176 (2011) 1778–1784. https://doi.org/10.1016/j.mseb.2011.05.032.

[21] G. Song, A. Atrens, Understanding Magnesium Corrosion—A Framework for Improved Alloy Performance, Advanced Engineering Materials. 5 (2003) 837–858. https://doi.org/10.1002/adem.200310405.

[22] J. Chen, L. Tan, K. Yang, Effect of heat treatment on mechanical and biodegradable properties of an extruded ZK60 alloy, Bioactive Materials. 2 (2017) 19–26. https://doi.org/10.1016/j.bioactmat.2016.12.002.

[23] R. Zeng, J. Zhang, W. Huang, W. Dietzel, K.U. Kainer, C. Blawert, W. Ke, Review of studies on corrosion of magnesium alloys, Transactions of Nonferrous Metals Society of China. 16 (2006) s763–s771. https://doi.org/10.1016/S1003-6326(06)60297-5.

[24] N. Winzer, A. Atrens, G. Song, E. Ghali, W. Dietzel, K.U. Kainer, N. Hort, C. Blawert, A Critical Review of the Stress Corrosion Cracking (SCC) of Magnesium Alloys, Advanced Engineering Materials. 7 (2005) 659–693. https://doi.org/10.1002/adem.200500071.

[25] J. Kuhlmann, I. Bartsch, E. Willbold, S. Schuchardt, O. Holz, N. Hort, D. Höche, W.R. Heineman, F. Witte, Fast escape of hydrogen from gas cavities around corroding magnesium implants, Acta Biomaterialia. 9 (2013) 8714–8721. https://doi.org/10.1016/j.actbio.2012.10.008.

[26] F. Witte, V. Kaese, H. Haferkamp, E. Switzer, A. Meyer-Lindenberg, C.J. Wirth, H. Windhagen, In vivo corrosion of four magnesium alloys and the associated bone response, Biomaterials. 26 (2005) 3557–3563. https://doi.org/10.1016/j.biomaterials.2004.09.049.

[27] D. Noviana, D. Paramitha, M.F. Ulum, H. Hermawan, The effect of hydrogen gas evolution of magnesium implant on the postimplantation mortality of rats, Journal of Orthopaedic Translation. 5 (2016) 9–15. https://doi.org/10.1016/j.jot.2015.08.003.

[28] T. Kraus, S.F. Fischerauer, A.C. Hänzi, P.J. Uggowitzer, J.F. Löffler, A.M. Weinberg, Magnesium alloys for temporary implants in osteosynthesis: In vivo studies of their degradation and interaction with bone, Acta Biomaterialia. 8 (2012) 1230–1238. https://doi.org/10.1016/j.actbio.2011.11.008.

[29] G. Song, Control of biodegradation of biocompatable magnesium alloys, Corrosion Science. 49 (2007) 1696–1701. https://doi.org/10.1016/j.corsci.2007.01.001.

[30] F. Seuss, S. Seuss, M.C. Turhan, B. Fabry, S. Virtanen, Corrosion of Mg alloy AZ91D in the presence of living cells, Journal of Biomedical Materials Research Part B: Applied Biomaterials. 99B (2011) 276–281. https://doi.org/10.1002/jbm.b.31896.

[31] S. Agarwal, J. Curtin, B. Duffy, S. Jaiswal, Biodegradable magnesium alloys for orthopaedic applications: A review on corrosion, biocompatibility and surface modifications, Materials Science and Engineering: C. 68 (2016) 948–963. https://doi.org/10.1016/j.msec.2016.06.020.

[32] Z.C. Cordero, B.E. Knight, C.A. Schuh, Six decades of the Hall–Petch effect – a survey of grain-size strengthening studies on pure metals, International Materials Reviews. 61 (2016) 495–512. https://doi.org/10.1080/09506608.2016.1191808.

[33] A. Bahmani, S. Arthanari, K.S. Shin, Formulation of corrosion rate of magnesium alloys using microstructural parameters, Journal of Magnesium and Alloys. 8 (2020) 134–149. https://doi.org/10.1016/j.jma.2019.12.001.

[34] L. Li, T. Wang, Y. Wang, C. Zhang, H. Lv, H. Lin, W. Yu, C. Huang, Effects of ytterbium addition and heat treatment on the mechanical properties and biocorrosion behaviors of Mg–Zn–Zr alloy, Journal of Magnesium and Alloys. 8 (2020) 499–509. https://doi.org/10.1016/j.jma.2019.11.013.

[35] Y. Song, E.-H. Han, D. Shan, C.D. Yim, B.S. You, The role of second phases in the corrosion behavior of Mg–5Zn alloy, Corrosion Science. 60 (2012) 238–245. https://doi.org/10.1016/j.corsci.2012.03.030.

[36] S. Shadanbaz, G.J. Dias, Calcium phosphate coatings on magnesium alloys for biomedical applications: A review, Acta Biomaterialia. 8 (2012) 20–30. https://doi.org/10.1016/j.actbio.2011.10.016.

Chapter 2:

Formation and Corrosion Behavior of Calcium Phosphate coating layers on ZK60

2.1. Introduction

Biodegradable magnesium (Mg) alloys have been studied widely as prospective implant devices in the evolution of biomaterials. Compared to commercial biomaterials, including stainless steels, cobalt-chromium(Co-Cr) alloys and titanium (Ti) alloys, the use of Mg alloys can avoid the occurrence of the stress shielding effect [1] and eliminate the secondary surgery after recovery because of their comparable elastic modules to that of human bone and their biodegradability, respectively [2]. Moreover, Mg was proved to stimulate new bone formation since Mg^{2+} ions enhance the attachment and proliferation of cells [3]. However, until present, Mg alloys have been mainly applied at unload-bearing positions as clinical screws [4], [5].

To be a load-bearing implant, Mg alloys need to meet the requirements for mechanical properties (e.g., ultimate tensile strength (UTS)≥250MPa, elongation (EL)≥15%), biocompatibility and corrosion resistance to ensure the implant could stay at least 12 weeks [6]. Mg-6mass% Zn-0.5mass%Zr (ZK60) alloy stands out as a potential candidate for load-bearing applications because of its good mechanical properties (UTS=300MPa and EL=19.6% [7]) and its bio-safe alloying elements [8], [9]. The extruded ZK60 alloy also exhibited good osteoconductivity and osteoinductivity in mice [10]. However, ZK60 alloy still encounters severe corrosion in the corrosive body fluid since this alloy possesses a relatively high corrosion rate. This fast degradability causes some drawbacks, such as the accumulation of hydrogen gas and/or the deterioration of the mechanical integrity between the implant and human bone [11]. Therefore, it is crucial to enhance the corrosion resistance of ZK60 alloy for clinical orthopedic applications.

An effective approach to reduce the high corrosion rate of ZK60 alloy is the use of calcium phosphate coating layers. It is stated that the calcium phosphate layers provided good biocompatibility and osteoconduction for bone repair applications [12], [13]. Xia *et al.* proved that the calcium phosphate coating layers with a wide range of Ca/P ratios showed different levels of corrosion resistance on ZK60 alloy [14]. Another study stated that the transformation of dicalcium phosphate dihydrate (DCPD) by heat treatment produced a coating layer that reduced the degradation rate of ZK60 in Hanks' solution and enhanced its cytocompatibility more notably than the primary DCPD layer [15]. Therefore, the composition of the calcium phosphate coating layers plays an essential role in improving both corrosion resistance and bioactivity of ZK60 alloy. Hiromoto *et al.* succeeded in producing different calcium phosphate coating layers by utilizing a chemical conversion method [16]. The calcium phosphate coating layer deposited in form of octacalcium phosphate (OCP) and/or hydroxyapatite (HAp) by controlling coating conditions [16],

[17]. In addition, it is stated that the properties of the calcium phosphate coating layers were also affected by the initial corrosion resistance of the substrate [18], [19]. However, the formation of the calcium phosphate coating layers on ZK60 alloy and their *in vitro* corrosion response have not been studied yet.

Therefore, this study aimed to investigate the formation and corrosion protectiveness of different types of calcium phosphate layers coated on ZK60 alloy. The calcium phosphate coating layers were prepared by adjusting the pH over a wide range in the chemical conversion method. In addition, the *in vitro* corrosion behavior in a culture medium of calcium phosphate coated ZK60 alloy was investigated by immersion tests with Mg^{2+} ion quantification.

2.2. Experiment procedure

2.2.1. Materials preparation

Round disks with 2 mm in thickness were machined from commercially extruded ZK60 rods with 20 mm in diameter (Osaka Fuji Industry, Japan) and utilized as substrates for the coating process. The chemical composition of the alloy is shown in Table 2.1. The microstructure of the as-extruded ZK60 alloy is illustrated in Figure 2.1. The surfaces of each disk were grounded with abrasive papers with grit from #500 to #4000, cleaned with ethanol, and then dried completely in air.

Table 2.1: Chemical composition of ZK60 alloy (mass%).

Mg	Zn	Zr	Al	Mn	Fe	Si	Cu	Ni
Bal.	5.28	0.521	0.0032	0.006	0.0006	0.0025	0.0007	0.0006

2.2.2. Coating process

The coating treatment was followed the chemical conversion method published by Hiromoto *et al.* [16]. The coating solution was prepared by mixing the same volume of 0.5 mol/L ethylenediaminetetraacetic acid calcium disodium salt hydrate ($C_{10}H_{12}CaN_2Na_2O_8$, Ca-EDTA) solution and 0.5 mol/L potassium dihydrogen phosphate (KH_2PO_4) solution. And then, 1 mol/L NaOH solution was added into the solution to adjust its pH value to 6.5, 7.0, 7.8 and 10.2. Disk specimens were immersed in the treatment solution when the solution reached a temperature of 90 ^{0}C. The temperature was kept stably at 90 ^{0}C during a coating period of 2 h. Finally, the specimens

were retrieved from the coating solution, rinsed quickly in distilled water and dried completely in air at room temperature. The dried specimens were then used for further analysis and investigation.

2.2.3. *In vitro* immersion test

Immersion tests were carried out to investigate the *in vitro* degradation behavior of the calcium phosphate-coated specimens. The uncoated specimens were used as a comparison. Three specimens for each treatment condition were utilized (n=3) and the average values were reported. Initially, the specimens were sterilized in acetone and dried thoroughly. The specimens were then immersed in a α-minimum essential medium (α-MEM; 12571-063, Gibco-Thermo Fisher Scientific) supplemented with 10 % fetal bovine serum (FBS; S1820-500, Biowest) and 1 % penicillin/streptomycin solution (P/S; 168-23191, Wako). The specimens were kept in an incubator humidified with 5 % CO_2 environment to maintain physiological pH at approximately 7.4. During the immersion tests, the temperature of the incubator was maintained at 37^0 C. The ratio of the volume of the testing solution and the total surface area of the specimen was 30 mL:1 cm^2. On the scheduled day 1, 3, 5, 7, 10, 14, 21, and 28 of the immersion tests, an insignificant portion, 100 μL, of the testing solution was sampled to quantify the Mg^{2+} ions using a test kit (Magnesium B-test Wako, FUJIFILM Wako, Tokyo, Japan) which employs a colorimetric method using xylidyl blue-I [20, 21]. A microplate spectrophotometer (Thermo Scientific, Multiskan Go) was used to measure the absorbance at 520 nm, the absorption wavelength of the chelate of xylidyl blue-I and Mg. After the immersion interval, the specimens were retrieved from the testing medium for specimen characterization.

2.2.4. Materials characterization

X-ray diffractometry (XRD; Rigaku, RINT-Ultima III) using Cu-K_α radiation was used to characterize the crystal phase of the calcium phosphate coatings and corrosion products deposited on the immersed specimens. A backscattered electron microscope (SEM; TM-6060, Hitachi) and a field-emission scanning electron microscope (FE-SEM; JSM-7200F, JEOL) equipped with an energy dispersion X-ray spectrometer (EDS) were utilized to analyze the surface morphology and cross-sectional structure of the coated and immersed specimens. For the cross-sectional observation, both as-coated specimens and immersed specimens were embedded in epoxy resin, grounded with abrasive papers with grits up to #4000 and then cleaned with ethanol.

2.3. Results

2.3.1. Characterization of calcium phosphate coating layers

Figure 2.2 (a) shows the X-ray diffraction patterns of the specimens coated at pH 6.5, 7.0, 7.8 and 10.2. The XRD pattern of the uncoated specimen was used as a reference. In the patterns of the sample coated at pH 6.5 and 7.0, the presence of the characteristic peak from $(010)_{OCP}$ at 4.7^0 indicates the formation of OCP crystals. Because the characteristic peak from $(002)_{HAp}$ and the peak from $(002)_{OCP}$ are around 26.0^0, Fig. 2.2 (b) with the magnified patterns is carried out to distinguish the difference between the peak position. According to the powder diffraction file of OCP (No. 44-0778) and HAp (No. 00-009-0432), the diffraction angle from the $(002)_{HAp}$ reflection is at nearly 26.0^0, which is slightly lower than that from the $(002)_{OCP}$ reflection at 26.1^0. Therefore, at pH 6.5, only OCP crystals were formed. However, at pH 7.0, not only the characteristic peak from $(010)_{OCP}$ but also the characteristic peak from $(002)_{HAp}$ was observed, indicating that both OCP and HAp were formed. At pH 7.8 and 10.2, only the characteristic peak from $(002)_{HAp}$ was observed, indicating the formation of HAp. Moreover, the formation of $Mg(OH)_2$ together with the HAp coating layer at pH 10.2 was confirmed by a relatively high-intensity peak at 18.5^0, according to the powder diffraction file of the hexagonal structure $Mg(OH)_2$ (No. 7-239). The results demonstrate that the pH conditions influenced significantly on the crystal phase of the calcium phosphate coating layers form on ZK60 alloy.

Figure 2.3 illustrates the surface and cross-sectional SEM images of the coating layers formed at various pH conditions. In Fig. 2.3 (a) to (c), the coating layers were formed homogeneously from pH 6.5 to 7.8. Meanwhile, the pH 10.2 coating was observed with cracks of the micrometer-size, which were indicated by red arrows in Fig. 2.3 (d). The morphology of the different coating layers was shown with high magnification images in Fig. 2.3 from (e) to (h). At pH 6.5, plate-shaped crystals specific to OCP were formed. Because the pH 7.0 coating layer contained both OCP and HAp crystals, plate-shaped crystals specific to OCP and rod-shaped crystals specific to HAp were observed. Rod-shaped HAp crystals were observed in the pH 7.8 coating layer, while agglomerates of needle-shaped HAp crystals with a sharp tip were formed in the pH 10.2 coating layer. The displacement among the agglomerates, as shown in Fig. 2.3 (h), may influence the corrosion protectiveness of the pH 10.2 coating layer.

Figure 2.3 (i) to (l) show the cross-sectional structure and thickness of the coated specimens. The calcium phosphate coating layers formed on ZK60 alloy consisted of two sub-layers including a dense inner layer and a porous outer layer. In addition, it could be seen that the coating layers

formed at pH 6.5 and pH 7.0 exhibited a thin inner layer with a thickness of approximately 1.0 μm, covered by the outer crystals with a length from 0.8 or 0.9 μm to 3.4 μm. In comparison, the thickness of the inner layers formed at pH 7.8 and pH 10.2 was thicker, approximately 1.8 μm and 1.9 μm, respectively. The length of the rod-shaped HAp crystals formed at pH 7.8 was longer than that of the needle-shaped HAp crystals formed at pH 10.2, about 3.0 μm and 1.4 μm, respectively

2.3.2. *In vitro* immersion results

Figure 2.4 shows the accumulated amount of Mg^{2+} ion release of the specimens in the medium solution during the immersion period. Initially, the Mg^{2+} ion concentration that released from the specimens increased at a high rate, suggesting the fast corrosion. Thereafter, the release rate reduced substantially. This reduction was attributed to the corrosion products which deposited on the surface of the substrates and acted as a barrier to restrict the further corrosion. A portion of released Mg^{2+} ions reacted with anions in the immersion solution to form corrosion products that deposited in the bottom of the containers. The specimens coated at pH 6.5, 7.0 and 7.8 showed a relatively low corrosion rate in the first 1 or 3 days. This period corresponds to an induction time for corrosion initiation. Compared to these three specimens, the specimens that were uncoated and coated at pH 10.2 showed a shorter induction time, indicating the faster corrosion initiation. During the immersion period, the uncoated specimen showed the highest release rate, whereas the specimen coated at pH 7.8 showed the lowest rate. The release rates of the specimens coated at pH 6.5 and 7.0 show no statistically meaningful difference. Even though the corrosion rate of the specimen coated at pH 10.2 was the second highest in the first 7 days, the subsequent rate reduced notably. The initial rapid rate of this specimen occurred due to the existence of micrometer-sized defects in its coating layer, as shown in Fig. 2.3 (d) and (h). All the pores in the outer layers are gaps between plate, rod or needle-like crystals growing from the inner layer, so all these pores penetrate from the immersion solution side to the inner layer, allowing easy penetration of the solution. It is reported that the non-through pores contributed insignificantly to the corrosion of micro-arc oxidation coatings during the initial stage of immersion, whereas the through-pores or micro-cracks provided pathways for the solution to reach the interface of the coating and ZK60 alloy [22]. Therefore, the initial corrosion rate of the specimens is considered to depend on the protectiveness of the inner layer.

Figure 2.5 illustrates the surface appearance of the specimens retrieved after the immersion period. In Fig. 2.5 (a), the uncoated specimen was covered with a light grey layer of corrosion products, which was peeled off due to the drying and characterizing processes. The round edge of

this specimen was collapsed due to corrosion. It suggests an occurrence of the most severe corrosion. The coated specimens were less corroded under the protection of the calcium phosphate coating layers. On the surface of the specimen coated at pH 6.5, numerous visible pits were observed. It implies the occurrence of localized pitting corrosion. In comparison, severe filiform corrosion and visible pitting occurred more severely on the specimen coated at pH 7.0, in Fig. 2.5 (c), indicating the lower corrosion resistance of this specimen. Nevertheless, the coating layers formed at pH 7.8 and 10.2 demonstrated much better corrosion protection, evidenced in the remaining of the coating after the immersion test, in Fig. 2.5 (d) and (e).

Figure 2.6 (a) to (e) depict the surface backscattered SEM images of the uncoated and coated specimens after the immersion test. The dark gray region of the uncoated specimen in Fig. 2.5 (a) was mainly covered by randomly oriented crystals in a columnar shape of the corrosion products. The specimens coated at pH 6.5 and 7.0 showed a similarity in the corrosion morphology. Cracks and corrosion products were observed around locally corroded positions. Nevertheless, on the surface of the specimens coated at pH 7.8 and 10.2, no obvious presence of the corrosion products was observed. Compared to the specimen coated at pH 7.8, that coated at pH 10.2 showed numerous cracks on its surface. Some of the cracks may form owing to the high vacuum environment during SEM observation.

Figure 2.6 (f) to (i) show the cross-sectional backscattered SEM images of the calcium phosphate-coated specimens after 28 days of immersion. It could be seen that dark gray regions of $Mg(OH)_2$ were observed beneath the coating layers formed at pH 6.5, 7.0 and 10.2. The $Mg(OH)_2$ regions were formed during the immersion test when the immersion solution penetrated through the coating layer and corroded the substrate. The $Mg(OH)_2$ regions presumably caused the detachment of the coating layer from the substrate during the grinding process, in Fig. 2.6 (f) and (i). The local presence of $Mg(OH)_2$ indicates the formation of pitting, in Fig. 2.6 (f), (g) and (i). On the other hand, the corrosion on the specimen coated at pH 7.8 was negligible as there was no noticeable existence of $Mg(OH)_2$ under the coating layer. The results indicate that the specimen coated at pH 7.8 exhibited the highest corrosion resistance.

Figure 2.7 (a) demonstrates the X-ray diffraction patterns of all the specimens after the immersion period. The patterns were compared with those of the as-prepared uncoated and coated specimens shown in Fig. 2.1. The diffraction pattern of the uncoated specimen included numerous peaks of corrosion products, which contain $Mg(OH)_2$, $CaCO_3$, $Mg_3(PO_4)_2$ and $Ca_xMg_y(PO_4)_z$. The presence of the corrosion products showed an agreement with previous studies about the degradation behavior of Mg-based materials under physiological conditions [23], [24], [25]. In Fig.

2.7 (b), EDS analysis on the surface of the uncoated specimen demonstrates the presence of mostly Mg and O elements at position #1, while Ca, P, C and S elements were acquired together with Mg and O elements at position #2. The result indicates that the randomly oriented columnar crystals of corrosion products observed in Fig. 2.5 (a) and Fig. 2.6 (a) were $Mg(OH)_2$ crystals. Other corrosion products observed in the XRD patterns were presumably formed underneath the $Mg(OH)_2$ layer. In the pattern of the specimen coated at pH 6.5, only one peak at 43.4^0 of $CaCO_3$ as a corrosion product was detected. In the case of the specimen coated at pH 7.0, high-intensity peaks of corrosion products of $Mg(OH)_2$ and $CaCO_3$ were obtained at 39.2^0 and 43.4^0, respectively. The EDS analysis on the cross section of this specimen in Fig. 2.7 (c) showed that the position #1 contained mainly Mg, O and C elements, indicating the formation of the corrosion products of $Mg(OH)_2$ and carbonate salt. At the position #2, Mg, O, Ca and P elements were mainly presented. The Ca/P was approximately 1.0, which is lower than the ratio of OCP (Ca/P=1.33) or HAp (Ca/P=1.67). The high percentage of Mg and the decrease in the Ca/P ratio suggest a capability of the presence of $Mg_3(PO_4)_2$, which lead to an increase in the percentage of P element. Interestingly, after the immersion period, the specimen coated at pH 7.8 showed a new diffraction peak of HAp at approximately 10.8^0. The extra precipitation of HAp crystals is attributed to the ability of the original HAp crystals to directly react with the immersion solution [26]. Nevertheless, there was no significant change in the pattern of the specimen coated at pH 10.2.

2.4. Discussion

2.4.1. Coating mechanism on Mg materials

The coating mechanism and the formed morphology of the calcium phosphate coating via the chemical conversion method was illustrated in Figures 2.8. Following the exposure of Mg alloy into the coating solution, the dissolution of Mg metal occurs immediately, as shown in equations (1) and (2). The dissolution of the Mg-based substrate plays an essential role since the dissolved areas act as nuclei in the formation of calcium phosphate coatings [18]. Simultaneously, Ca^{2+} ions were generated during the dissolution of $Ca(edta)^{2-}$ chelate in the coating solution under a hydrothermal condition, as shown in equation (3) [18]. As the results of the reaction (2), a great amount of OH^- was generated, leading to a rapid pH increase in local surface area of the substrate. This local pH increase promotes a rapid precipitation of calcium phosphate, including OCP and HAp int this study, with simultaneous formation of $Mg(OH)_2$ on the substrate surface, according to equations (4), (5) and (6), respectively. Due to $Mg(OH)_2$ has a much higher solubility [27], the

OCP and/or HAp formation was more preferentially than the $Mg(OH)_2$ formation. The formation of calcium phosphate proceeded rapidly thanks to the rapid dissolution of the Mg substrate in the initial stage, resulting in the formation of calcium phosphate film consisting of spherical particles. As the coating time progressed, this dense inner layer of OCP and/or HAp formed and thickened. The inner layer then moderated or prevent the further dissolution of Mg. Subsequently, OCP and HAp gradually precipitates to develop into the plate-like and rod-like/needle-like particles, respectively. It is noted that the $Mg(OH)_2$ formation is continuous gradually as the coating process progresses. Also, according to the equation (2) in the dissolution of Mg, hydrogen gas (H_2) is evolved. This evolution of H_2 gas is believed to cause defects, such as micro pores, in the formed calcium phosphate coating layers [28].

(1) $Mg \rightarrow Mg^{2+} + 2e^-$

(2) $2H_2O + 2e^- \rightarrow 2OH^- + H_2$

(3) $Ca(edta)^{2-} \rightarrow Ca^{2+} + edta^{4-}$

(4) OCP: $8Ca^{2+} + 6HPO_4^{2-} + 4OH^- + H_2O \rightarrow Ca_8(PO_4)_4(HPO_4)_2.5H_2O$

(5) HAp: $10Ca + 6PO_4^{3-} + 2OH^- \rightarrow Ca_{10}(PO_4)_6(OH)_2$

(6) $Mg + 2OH \rightarrow Mg(OH)_2$

2.4.2. Formation of calcium phosphate coatings on ZK60 alloy

Figures 2.2 and 2.3 illustrate that various calcium phosphate coating layers were formed on the surface of as-extruded ZK60 alloy by applying the chemical conversion method. The results also pointed out that pH conditions influenced significantly the crystal phase and morphology of the calcium phosphate coating layers. The calcium phosphate crystals changed from plate-shaped to needle-shaped crystals as the pH value increased from 6.5 to 10.2. The structure of the calcium phosphate coating layers on ZK60 alloy was in a similar manner to the structure of the coating layers on the other types of Mg-based materials [16], [28], [29], [30], suggesting the same formation mechanism, which reported previously on pure Mg and AZ31 alloy [17], [30]. OCP was formed in the solution of pH 6.5 and HAp was formed in the solutions of pH 7.0, 7.8 and 10.2 because OCP and HAp phases are chemically stable in each pH solution [28]. Because the corrosion rate of the Mg alloys reduced as the pH value increased [28], ZK60 alloy corroded faster at pH 7.0 than at pH 7.8 and 10.2, leading to more abundant Mg ion release. It is reported that at a high concentration of Mg ions, the HAp formation was much more strongly inhibited than the OCP formation [32]. Therefore, initially, the formation of HAp was inhibited at pH 7.0, so OCP was

formed. As the precipitated OCP covered the surface of ZK60 alloy, the corrosion of the alloy was delayed, conditioned for the formation of HAp. Additionally, it is reported that during a direct hydrolysis of OCP without catalysts at a temperature above 60 ^{0}C, the transformation of OCP to HAp occurred at a pH of about 6.7 [33]. Hence, both OCP and HAp were present at pH 7.0.

The $Mg(OH)_2$ peak in XRD patterns was observed at pH 10.2 in this study, while it only appeared at pH above 11 in the case of pure Mg and AZ alloys [16]. The formation of $Mg(OH)_2$ during the coating process was due to the initial corrosion of the substrate caused by the coating solution [27]. This indicates that the corrosion rate of ZK60 alloy is higher than that of pure Mg and AZ alloys. The original corrosion rate of the substrate also plays an important role in the corrosion resistance performance when the corrosive solution penetrates through the coating layer. Therefore, it is also necessary to enhance the original corrosion resistance of ZK60 alloy, in addition to the surface coating treatment. Additionally, it should be noted that the second phases of the as-extruded ZK60 alloy have a fine particle size, approximately 1.3 μm or less, as shown in Fig. 2.1. These fine second phase particles can limit the crack formation and delamination of the coating layer, which was caused by the coarse particles of more than a few tens of micrometers in size as reported in the case of Mg-Zn alloys [30].

2.4.3. *In vitro* corrosion behavior of immersed samples

The results from the Mg^{2+} ion quantification and the surface and the cross-sectional observation of all the specimens after 28 days of immersion prove that the calcium phosphate coating layers delayed notably the degradation of ZK60 alloy. However, localized corrosions, such as filiform and pitting, still took place because nano-scale defects, such as pores and cracks, always exist in the HAp or OCP coating layers [27], [30]. Among various coatings, the HAp coating layer formed at pH 7.8 showed the most effective corrosion protection ability because this coating layer was highly uniform and its inner layer was relatively thick, about 1.8 μm. In comparison, the pH 10.2 coating layer exhibited lower corrosion protection even though its inner layer was slightly thicker, approximately 1.9 μm. This is mainly due to the existence of micrometer-sized cracks in this coating layer, as depicted in Fig. 2.3 (d) and (h). The cracks also caused the short induction time for the corrosion initiation of this specimen as in Fig. 2.4. In addition, the EDS line scan profiles of various elements along the cross section of the specimen coated at pH 10.2 in Figure 2.9 revealed that a thin intermediate layer of $Mg(OH)_2$ was formed during the coating process, indicated by the co-existence of Mg and O elements, with no other elements detected. The

$Mg(OH)_2$ intermediate layer also caused lower corrosion resistance of the specimen coated at pH 10.2, compared to that coated at pH 7.8.

On the other hand, the specimens coated at pH 6.5 and 7.0 showed lower levels of corrosion resistance, compared to those coated at pH 7.8 and 10.2. This is due to the thinner inner layer of the coating layers shown in Fig. 2.2 and a higher dissolution rate of the OCP crystals than the HAp crystals [28]. The higher corrosion protection ability of the HAp coating layer than the OCP and OCP+HAp coating layers was also reported previously [28]. Due to the lower corrosion protection of the OCP-containing coating layer, localized corrosion, including pitting and filiform, was observed obviously on the surface and underneath the coating layers formed at pH 6.5 and 7.0, in Fig. 2.5 and 2.6. When the corrosive immersion solution reached the coating/substrate interface through the existing defects of the coating layers, localized corrosion occurred, which led to filiform and pitting corrosion. The growth of the pits took place due to the changeable positions of micro-cathodes and anodes [34]. Pitting corrosion could also be initiated when the secondary phase particles were present at the localized-corrosion sites [35].

The OCP+HAp coating layer formed at pH 7.0 showed slightly lower corrosion protection compared to the OCP coating layer formed at pH 6.5, as depicted in Fig. 2.4 and 2.5. It is reported that during the hydrolysis of OCP, before transforming into HA crystals, the first-formed crystalline OCP phase became so unstable [36]. Therefore, it is strongly believed that this unstable OCP phase exists in the OCP+HAp coating layer and are the main reason for the lower corrosion protection of this coating layer, in comparison with the OCP coating layer.

2.5. Conclusion

In this study, the calcium phosphate coating layers were formed on the surface of the extruded ZK60 substrate. The morphology and crystal phase of the coating layers were influenced by pH conditions. The OCP single phase layer and the OCP+HAp mixture layer were formed at pH 6.5 and 7.0, respectively. The HAp single phase layer and the HAp layer with an intermediate $Mg(OH)_2$ layer were formed at pH 7.8 and 10.2, respectively. This resulted in the different *in vitro* degradation performance of the calcium phosphate-coated specimens. The induction time for the corrosion initiation of the specimens coated at pH 6.5, 7.0 and 7.8 was longer than that of the specimens that uncoated and coated at pH 10.2. The corrosion rates of the specimens coated at pH 6.5 and 7.0 were high due to their thin inner layers and their OCP-containing coating layers. The localized corrosion was observed in these two specimens after the immersion test. In comparison, the corrosion rate of the specimen coated at pH 10.2 was lower at the end of the immersion interval,

but this rate was rapid in the first 7 days mainly because of the pH 10.2 coating layer containing micrometer-sized defects. The specimen coated at pH 7.8 exhibited the lowest corrosion rate, owing to its uniform-crystallized HAp coating layer. Furthermore, the deposition of biocompatible HA crystals was observed only on this specimen after the immersion test. The results indicated that ZK60 alloy coated in the solution of pH 7.8 is the most suitable degradable material for implantation. However, to be successfully applied as a load-bearing implant in the clinical use, the initial corrosion resistance of as-extruded ZK60 alloy should be improved before the coating treatment and the electrochemical behavior of each coating layer should be studied in the future.

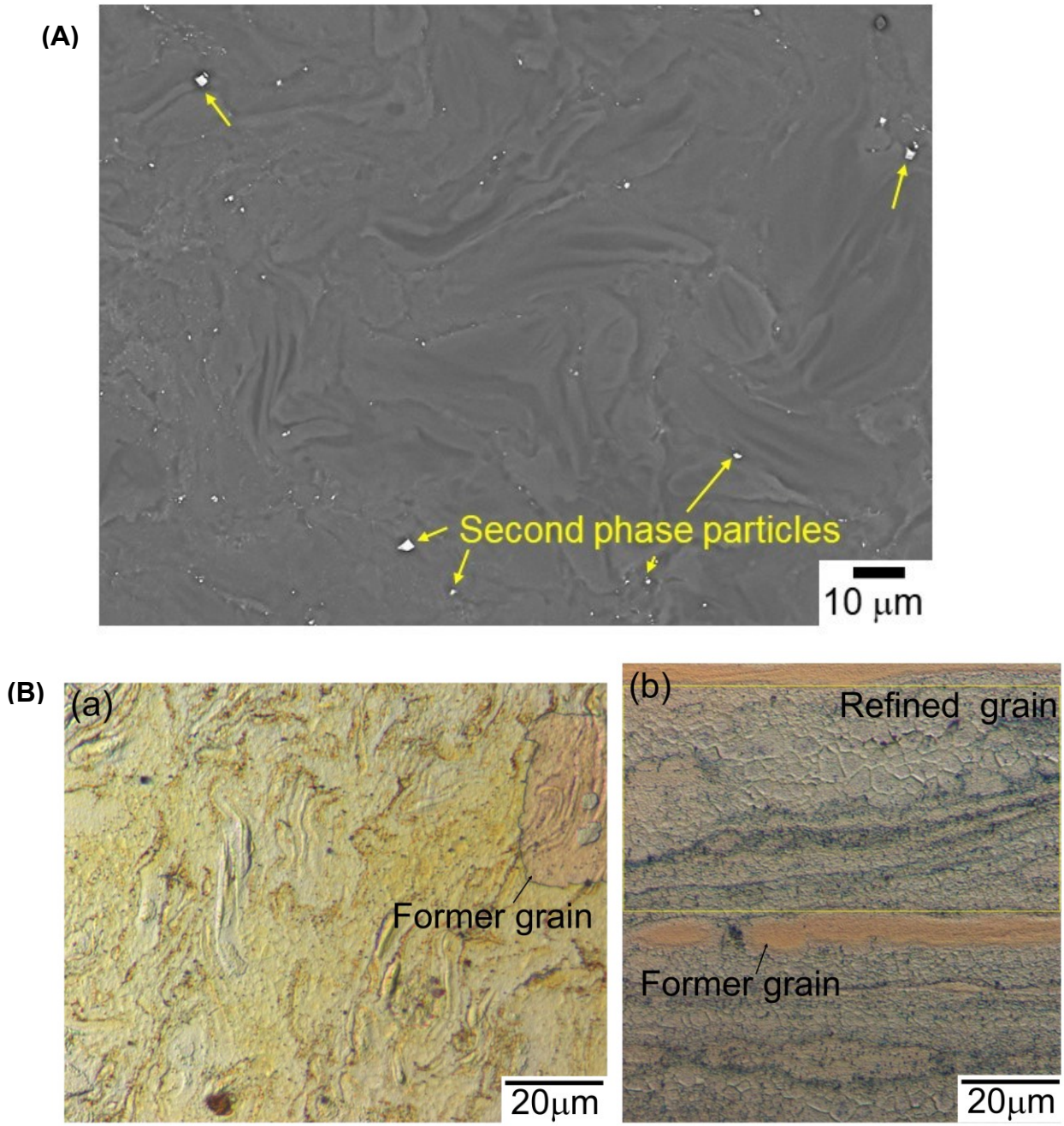

Fig. 2.1: (A) SEM micrograph of as-extruded ZK60 alloy. (B) Optical microscope images of (a) cross section and (b) longitudinal section of the as-extruded ZK60 rod. The yellow square in (b) shows a region containing refined grains after extrusion of the alloy.

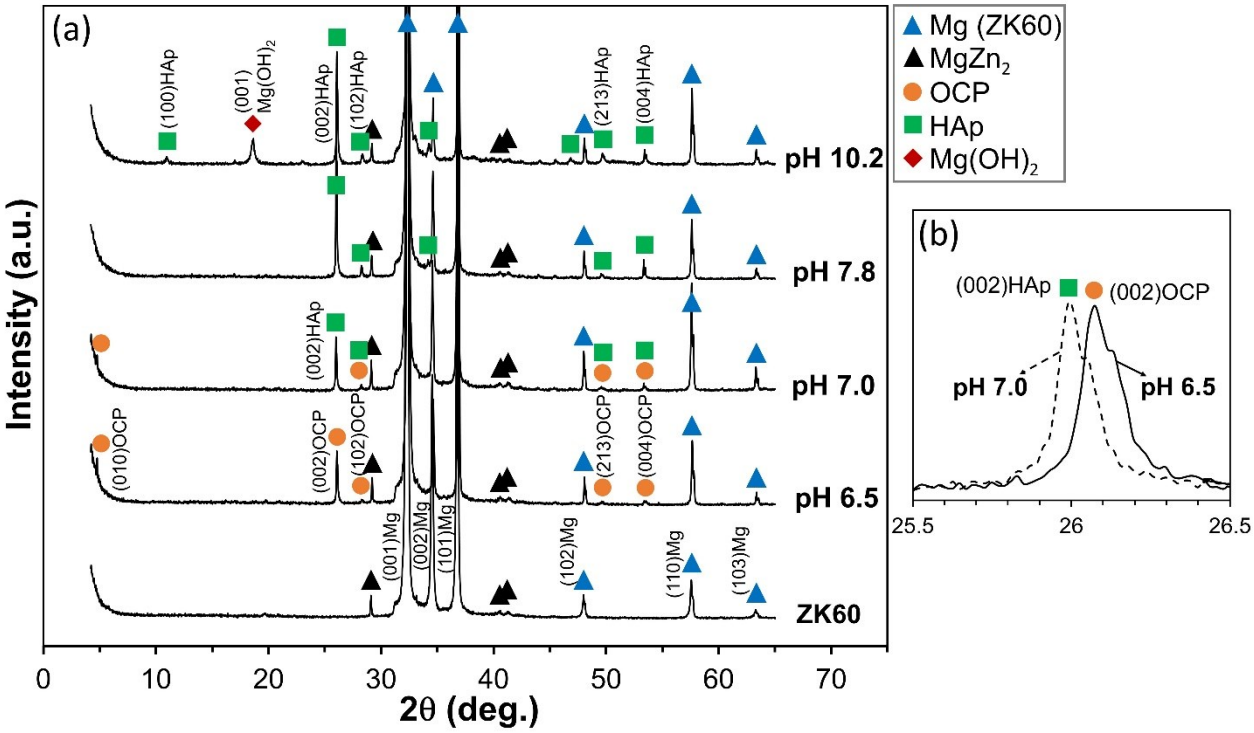

Fig. 2.2: (a) XRD patterns of ZK60 specimens coated at various pH conditions. (b) Magnified XRD patterns of the specimens coated at pH 6.5 and 7.0 to distinguish the characteristic peak of $(002)_{HAp}$ and the peak of $(002)_{OCP}$ at about 26.0^0.

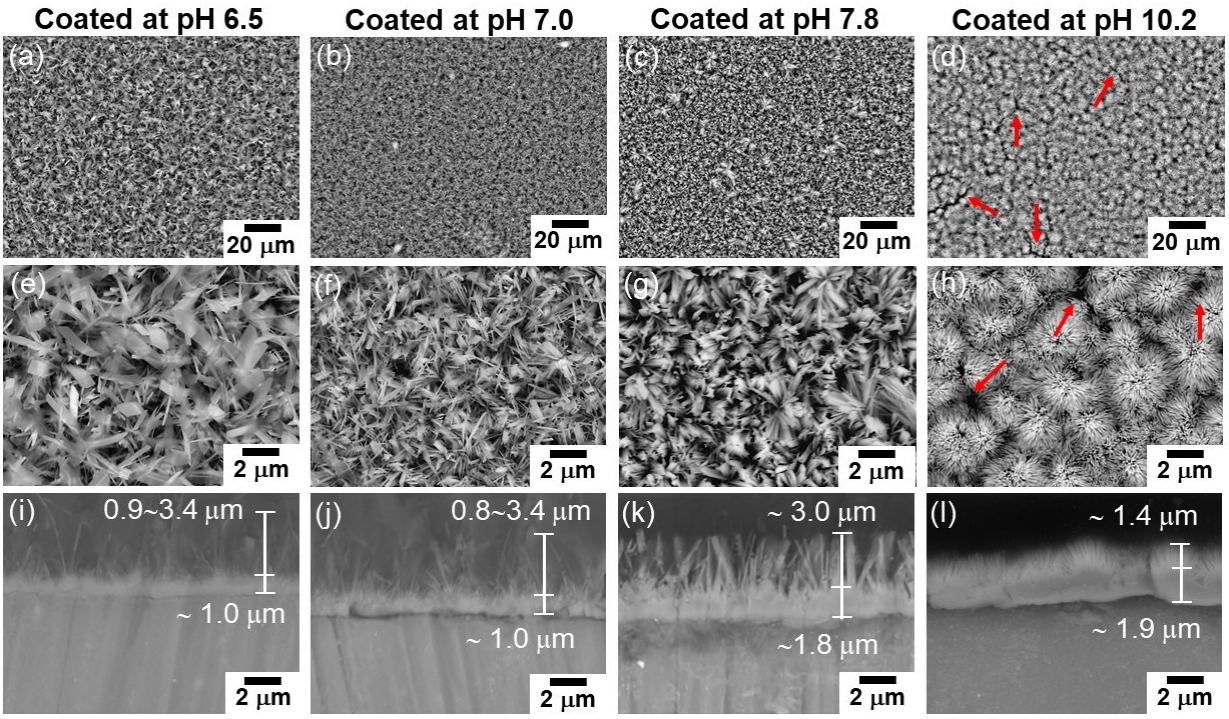

Fig. 2.3: Surface and cross-sectional SEM images of the specimens coated at pH 6.5 (a, e and i), at pH 7.0 (b, f and j), at pH 7.8 (c, g and k) and at pH 10.2 (d, h and l). Red arrows point out the micrometer-sized defects of the pH 10.2 coating layer.

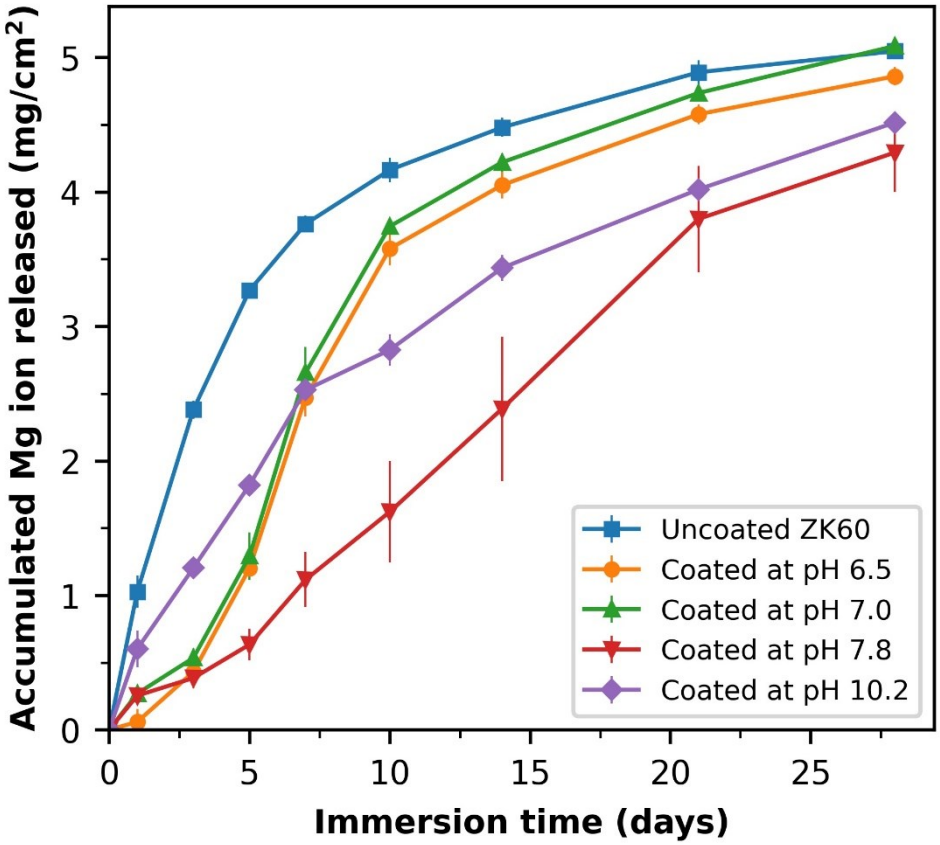

Fig. 2.4: The amount of Mg^{2+} ion released in α-MEM+FBS medium during 28 days of immersion. The values represent the mean ± standard deviation (n=3).

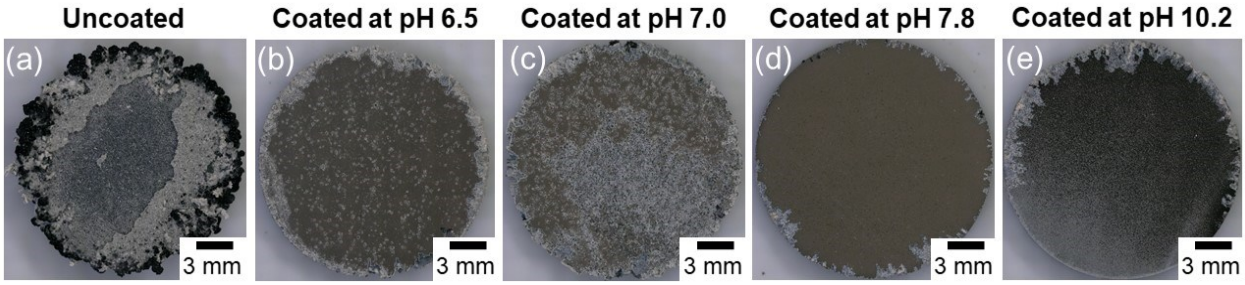

Fig. 2.5: Surface appearance of uncoated specimen (a) and specimens coated at pH 6.5 (b), at pH 7.0 (c), at pH 7.8 (d) and at pH 10.2 (e) after 28 days of immersion.

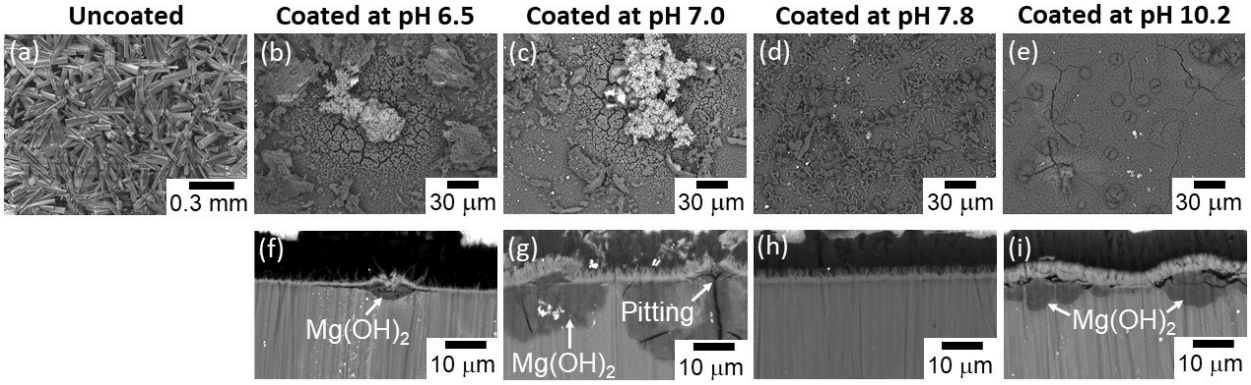

Fig. 2.6: Surface and cross-sectional SEM images of immersed specimen: uncoated (a), coated at pH 6.5 (b and f), at pH 7.0 (c and g), at pH 7.8 (d and h) and at pH 10.2 (e and i).

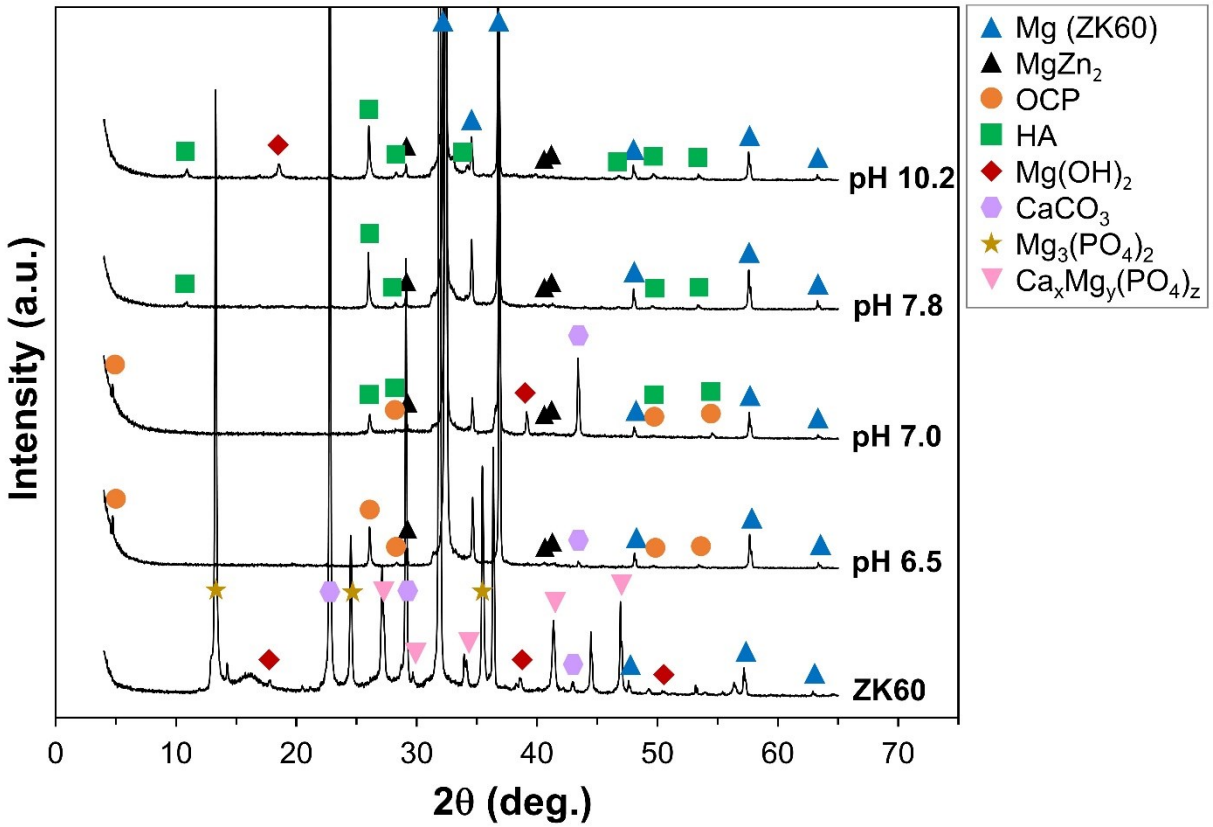

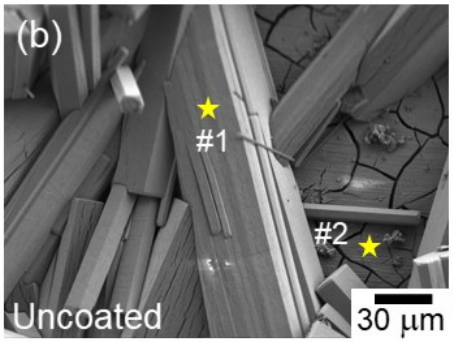

At %	#1	#2
Mg	23.00	12.40
Ca	—	6.59
Zn	0.03	2.71
P	0.02	9.67
O	75.61	60.69
C	1.34	5.06
S	—	2.88

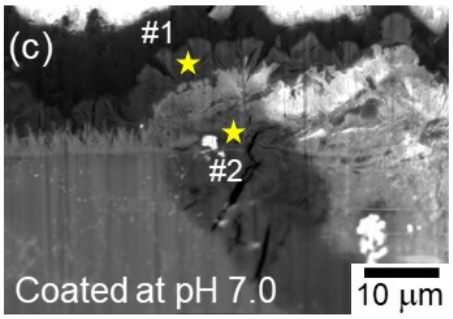

At %	#1	#2
Mg	25.28	14.35
Ca	0.87	11.55
Zn	1.69	1.35
P	1.39	11.07
O	48.28	55.84
C	19.58	4.24
S	2.91	1.60

Fig. 2.7: (a) XRD patterns of the specimens after 28 days of immersion. The EDS analysis on (b) the surface of the uncoated specimen and (c) the cross section of the specimen coated at pH 7.0.

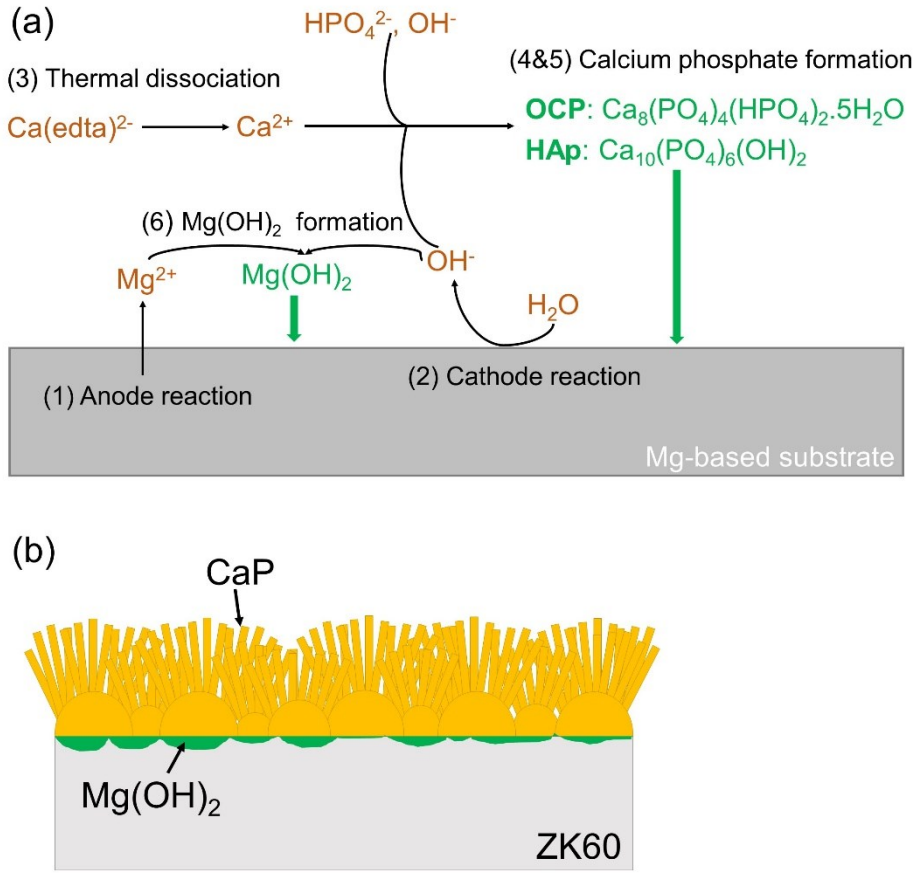

Fig. 2.8: (a) Coating mechanism of calcium phosphate on Mg-based substrates. (b) Coating morphology of the formed calcium phosphate coating.

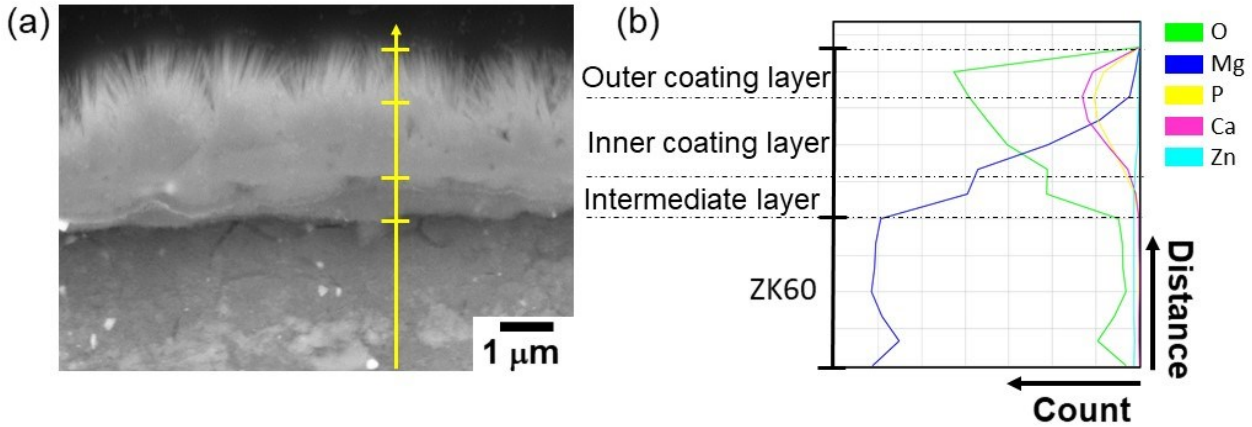

Fig. 2.9: EDS line scan along a drawn line in the cross section of the specimen coated at pH 10.2.

References

[1] S. Kamrani, C. Fleck, Biodegradable magnesium alloys as temporary orthopaedic implants: a review, Biometals. 32 (2019) 185–193. https://doi.org/10.1007/s10534-019-00170-y.

[2] A. Atrens, M. Liu, N.I. Zainal Abidin, Corrosion mechanism applicable to biodegradable magnesium implants, Materials Science and Engineering: B. 176 (2011) 1609–1636. https://doi.org/10.1016/j.mseb.2010.12.017.

[3] F. Witte, The history of biodegradable magnesium implants: A review, Acta Biomaterialia. 6 (2010) 1680–1692. https://doi.org/10.1016/j.actbio.2010.02.028.

[4] J.-M. Seitz, A. Lucas, M. Kirschner, Magnesium-Based Compression Screws: A Novelty in the Clinical Use of Implants, JOM. 68 (2016) 1177–1182. https://doi.org/10.1007/s11837-015-1773-1.

[5] D. Zhao, S. Huang, F. Lu, B. Wang, L. Yang, L. Qin, K. Yang, Y. Li, W. Li, W. Wang, S. Tian, X. Zhang, W. Gao, Z. Wang, Y. Zhang, X. Xie, J. Wang, J. Li, Vascularized bone grafting fixed by biodegradable magnesium screw for treating osteonecrosis of the femoral head, Biomaterials. 81 (2016) 84–92. https://doi.org/10.1016/j.biomaterials.2015.11.038.

[6] X.N. Gu, N. Li, Y.F. Zheng, L. Ruan, In vitro degradation performance and biological response of a Mg–Zn–Zr alloy, Materials Science and Engineering: B. 176 (2011) 1778–1784. https://doi.org/10.1016/j.mseb.2011.05.032.

[7] J. Chen, L. Tan, K. Yang, Effect of heat treatment on mechanical and biodegradable properties of an extruded ZK60 alloy, Bioactive Materials. 2 (2017) 19–26. https://doi.org/10.1016/j.bioactmat.2016.12.002.

[8] L.M. Plum, L. Rink, H. Haase, The Essential Toxin: Impact of Zinc on Human Health, International Journal of Environmental Research and Public Health. 7 (2010) 1342–1365. https://doi.org/10.3390/ijerph7041342.

[9] D.B.N. Lee, M. Roberts, C.G. Bluchel, R.A. Odell, Zirconium: Biomedical and Nephrological Applications, ASAIO Journal. 56 (2010) 550–556. https://doi.org/10.1097/MAT.0b013e3181e73f20.

[10] Z.-R. Qi, Q. Zhang, L.-L. Tan, X. Lin, Y. Yin, X.-L. Wang, K. Yang, Y. Wang, Comparison of degradation behavior and the associated bone response of ZK60 and PLLA in vivo, Journal of Biomedical Materials Research Part A. 102 (2014) 1255–1263. https://doi.org/10.1002/jbm.a.34795.

[11] D. Zhao, F. Witte, F. Lu, J. Wang, J. Li, L. Qin, Current status on clinical applications of magnesium-based orthopaedic implants: A review from clinical translational perspective, Biomaterials. 112 (2017) 287–302. https://doi.org/10.1016/j.biomaterials.2016.10.017.

[12] S.V. Dorozhkin, M. Epple, Biological and Medical Significance of Calcium Phosphates, Angewandte Chemie International Edition. 41 (2002) 3130–3146. https://doi.org/10.1002/1521-3773(20020902)41:17<3130::AID-ANIE3130>3.0.CO;2-1.

[13] R. Bosco, E.R.U. Edreira, J.G.C. Wolke, S.C.G. Leeuwenburgh, J.J.J.P. van den Beucken, J.A. Jansen, Instructive coatings for biological guidance of bone implants, Surface and Coatings Technology. 233 (2013) 91–98. https://doi.org/10.1016/j.surfcoat.2013.02.039.

[14] K. Xia, H. Pan, T. Wang, S. Ma, J. Niu, Z. Xiang, Y. Song, H. Yang, X. Tang, W. Lu, Effect of Ca/P ratio on the structural and corrosion properties of biomimetic CaP coatings on ZK60 magnesium alloy, Materials Science and Engineering: C. 72 (2017) 676–681. https://doi.org/10.1016/j.msec.2016.11.132.

[15] K. Li, B. Wang, B. Yan, W. Lu, Microstructure, in vitro corrosion and cytotoxicity of Ca-P coatings on ZK60 magnesium alloy prepared by simple chemical conversion and heat treatment, J Biomater Appl. 28 (2013) 375–384. https://doi.org/10.1177/0885328212453958.

[16] S. Hiromoto, A. Yamamoto, High corrosion resistance of magnesium coated with hydroxyapatite directly synthesized in an aqueous solution, Electrochimica Acta. 54 (2009) 7085–7093. https://doi.org/10.1016/j.electacta.2009.07.033.

[17] S. Hiromoto, M. Tomozawa, Hydroxyapatite coating of AZ31 magnesium alloy by a solution treatment and its corrosion behavior in NaCl solution, Surface and Coatings Technology. 205 (2011) 4711–4719. https://doi.org/10.1016/j.surfcoat.2011.04.036.

[18] Y. Fujishiro, T. Sato, A. Okuwaki, Coating of hydroxyapatite on metal plates using thermal dissociation of calcium-EDTA chelate in phosphate solutions under hydrothermal conditions, J Mater Sci: Mater Med. 6 (1995) 172–176. https://doi.org/10.1007/BF00120295.

[19] S. Hiromoto, E. Nozoe, K. Hanada, T. Yoshimura, K. Shima, T. Kibe, N. Nakamura, K. Doi, In vivo degradation and bone formation behaviors of hydroxyapatite-coated Mg alloys in rat femur, Materials Science and Engineering: C. 122 (2021) 111942. https://doi.org/10.1016/j.msec.2021.111942.

[20] 寛人渡辺, 裕晃田中, キシリジルブルーi と非イオン性界面活性剤を用いるマグネシウムの二波長吸光光度定量, 分析化学. 26 (1977) 635–639. https://doi.org/10.2116/bunsekikagaku.26.9_635.

[21] C.K. Mann, J.H. Yoe, Spectrophotometric Determination of Magnesium with Sodium 1-Azo-2-hydroxy-3-(2,4-dimethylcarboxanilido)-naphthalene-1′-(2-hydroxybenzene-5-sulfonate), Anal. Chem. 28 (1956) 202–205. https://doi.org/10.1021/ac60110a016.

[22] L.-Y. Cui, R.-C. Zeng, S.-K. Guan, W.-C. Qi, F. Zhang, S.-Q. Li, E.-H. Han, Degradation mechanism of micro-arc oxidation coatings on biodegradable Mg-Ca alloys: The influence of porosity, Journal of Alloys and Compounds. 695 (2017) 2464–2476. https://doi.org/10.1016/j.jallcom.2016.11.146.

[23] J. Gonzalez, R.Q. Hou, E.P.S. Nidadavolu, R. Willumeit-Römer, F. Feyerabend, Magnesium degradation under physiological conditions – Best practice, Bioactive Materials. 3 (2018) 174–185. https://doi.org/10.1016/j.bioactmat.2018.01.003.

[24] S. Zhang, Y. Bi, J. Li, Z. Wang, J. Yan, J. Song, H. Sheng, H. Guo, Y. Li, Biodegradation behavior of magnesium and ZK60 alloy in artificial urine and rat models, Bioactive Materials. 2 (2017) 53–62. https://doi.org/10.1016/j.bioactmat.2017.03.004.

[25] D. Tie, F. Feyerabend, N. Hort, R. Willumeit, D. Hoeche, XPS Studies of Magnesium Surfaces after Exposure to Dulbecco's Modified Eagle Medium, Hank's Buffered Salt Solution, and Simulated Body Fluid, Advanced Engineering Materials. 12 (2010) B699–B704. https://doi.org/10.1002/adem.201080070.

[26] H.-M. Kim, T. Himeno, T. Kokubo, T. Nakamura, Process and kinetics of bonelike apatite formation on sintered hydroxyapatite in a simulated body fluid, Biomaterials. 26 (2005) 4366–4373. https://doi.org/10.1016/j.biomaterials.2004.11.022.

[27] M. Tomozawa, S. Hiromoto, Growth mechanism of hydroxyapatite-coatings formed on pure magnesium and corrosion behavior of the coated magnesium, Applied Surface Science. 257 (2011) 8253–8257. https://doi.org/10.1016/j.apsusc.2011.04.087.

[28] M. Tomozawa, S. Hiromoto, Microstructure of hydroxyapatite- and octacalcium phosphate-coatings formed on magnesium by a hydrothermal treatment at various pH values, Acta Materialia. 59 (2011) 355–363. https://doi.org/10.1016/j.actamat.2010.09.041.

[29] S. Hiromoto, S. Itoh, N. Noda, T. Yamazaki, H. Katayama, T. Akashi, Osteoclast and osteoblast responsive carbonate apatite coatings for biodegradable magnesium alloys, Science and Technology of Advanced Materials. 21 (2020) 346–358. https://doi.org/10.1080/14686996.2020.1761237.

[30] D.N. Pham, S. Hiromoto, M. O, E. Kobayashi, Influence of substrate microstructure on hydroxyapatite coating and corrosion behavior of coated MgZn alloys, Surface and Coatings Technology. 421 (2021) 127414. https://doi.org/10.1016/j.surfcoat.2021.127414.

[31] N.Q. Cao, H.M. Le, K.M. Pham, N.V. Nguyen, S. Hiromoto, E. Kobayashi, In Vitro Corrosion and Cell Response of Hydroxyapatite Coated Mg Matrix in Situ Composites for Biodegradable Material Applications, Materials. 12 (2019) 3474. https://doi.org/10.3390/ma12213474.

[32] M.H. Salimi, J.C. Heughebaert, G.H. Nancollas, Crystal growth of calcium phosphates in the presence of magnesium ions, Langmuir. 1 (1985) 119–122. https://doi.org/10.1021/la00061a019.

[33] S. Graham, P.W. Brown, Reactions of octacalcium phosphate to form hydroxyapatite, Journal of Crystal Growth. 165 (1996) 106–115. https://doi.org/10.1016/0022-0248(95)00994-9.

[34] S. Hiromoto, M. Inoue, T. Taguchi, M. Yamane, N. Ohtsu, In vitro and in vivo biocompatibility and corrosion behaviour of a bioabsorbable magnesium alloy coated with octacalcium phosphate and hydroxyapatite, Acta Biomaterialia. 11 (2015) 520–530. https://doi.org/10.1016/j.actbio.2014.09.026.

[35] R. Zeng, K.U. Kainer, C. Blawert, W. Dietzel, Corrosion of an extruded magnesium alloy ZK60 component—The role of microstructural features, Journal of Alloys and Compounds. 509 (2011) 4462–4469. https://doi.org/10.1016/j.jallcom.2011.01.116.

[36] J.L. Meyer, E.D. Eanes, A thermodynamic analysis of the amorphous to crystalline calcium phosphate transformation, Calc. Tis Res. 25 (1978) 59–68. https://doi.org/10.1007/BF02010752.

Chapter 3:

In vitro biocompatibility and in vivo degradation behavior of calcium phosphate coated ZK60 alloy

3.1. Introduction

Magnesium (Mg) alloys have evolved as potential materials for biodegradable implant devices due to their outstanding properties: comparable density and elastic modulus to those of human bones, biocompatibility and biodegradability [1], [2]. In biomedical use, the biosafety of the alloying elements contained in a Mg alloy system is taken into consideration. In Mg-6mass% Zn-0.5mass% Zr (ZK60) alloy, both Zn and Zr alloying elements with the designated amount are proved to be biocompatible [3], [4]. The addition of Zn and Zr enhance the mechanical properties to meet the requirement of load-bearing applications [3], [5], [6]. However, the low corrosion resistance of ZK60 alloy has limited its clinical feasibility [7], [8], [9].

To improve the corrosion resistance and enhance the biocompatibility of Mg/Mg alloys, surface treatment with calcium phosphate (Ca-P) coatings is extensively studied because of their excellent biocompatibility, low solubilities and good antibacterial performance which avoids serious biofilm-associated infections caused by bacteria [10], [11], [12]. The Ca-P coatings also showed good bioactivity because their surface contains negatively charged functional groups which strongly induce biomineralization of Ca-P crystallites on the implant [13]. Among various coating methods, the chemical conversion method introduced by Hiromoto et al. is a simple and cost-effective single-step process using environmentally friendly reagents and can apply to any shape of the device [14]. The Ca-P coating can be in the form of octacalcium phosphate (OCP, $Ca_8(PO_4)_4(HPO_4)_2.5H_2O$) with its specific plate-shaped crystals, or hydroxyapatite (HAp, $Ca_{10}(PO_4)_6(OH)_2$) with rod-/needle-shaped crystals [15]. Numerous studies proved that cell behavior on a Ca-P coated material depends strongly on the type, morphology and corrosion property of the coating [16], [17], [18], [19]. It is reported that the corrosion property of different types of the Mg-based alloy substrate influenced the morphology and corrosion protectiveness of the Ca-P coating deposited in the chemical conversion method [20], [21]. In our previous study, we investigated the formation and corrosion behavior of different Ca-P coatings formed on ZK60 alloy [22]. The type, morphology and corrosion protectiveness of the formed coatings varied at different pH coating conditions. However, the influence on cellular biocompatibility of the Ca-P coatings with different surface properties formed on ZK60 alloy have not been investigated yet.

Therefore, in this work, the cell viability of those Ca-P coatings formed at pH 6.5, 7.8 and 10.2 on ZK60 alloy was investigated. Furthermore, animal tests were carried out in rabbits to provide a comprehensive view of the *in vivo* degradation behavior of ZK60 alloy that uncoated and coated with the optimum Ca-P coating to determine the feasibility of use.

3.2. *In vitro* cell behavior

3.2.1. Cell interaction with biomaterials

Osteoblasts are critically important for bone formation and remodelling since they synthesize and secrete bone matric and promote the mineralization of bone [23], [24]. Osteoblasts at the bone surface are classified into three types: preosteoblast, active and inactive osteoblasts. In which, preosteoblasts are those cells that differentiate into active bone-secreting osteoblasts. Also, not only active osteoblasts, preosteoblasts already produce collagen type I forming 90 % of the organic bone mass [25]. Hence, the understanding of conditions of preosteoblasts adhering on a surface is crucial. The most popular preosteoblast cell line is MC3T3-E1 derived from mice, but it is often used to represent osteoblasts in vitro [26]. Therefore, in this study, MC3T3-E1 pre-osteoblasts were selected to investigate the in vitro biocompatibility of the coated ZK60 samples.

The major of cell types, including osteoblastic cells, are required to adhere to extracellular matric to survive. Thus the quality of adhesion is critical for their survival and functional performance. The fact is that immediately after explored to the culture medium or body fluids, a protein layer is adsorbed on material surfaces; after that, cells respond to that material through the adsorbed layer [18]. The initial surface properties of the material define amount, conformation and types of the adsorbed proteins [27]. After sensing the protein layer, cells then (1) adhere to it by forming focal contacts, (2) when the number and size of the focal contacts increase, cells will spread out and orientate themselve according to the surface features, (3) cells will proliferate, which means cells divide to increase their number and (4) cells will differentiate, which means cells change into their phenotypical type to perform their functions [18]. Generally, the material surface properties are the key factors for cell survival since they control the quality of cell adhesion.

Recently, the growing interest in cell-matrix interfaces has motivated numerous studies of surface parameters, such as topography or roughness, wettability, chemical composition and charge, elasticity and so on [28], [29], [30]. In various parameters, surface chemistry and topography are the most two important parameters. Owing to difference in ion concentration across cell membrane, all cells exhibit negative potential varying from -10 to -90 mV [31]. As a result, a positive potential surface benefits in the cell attachment. The surface topography showed a significant effect on both proliferation and differentiation. It is shown that an increase in surface roughness and disorder decreased cell proliferation [32].

In this study, ZK60 samples were coated at three pH conditions. The surface charge of the coated materials is properly different from that of the uncoated materials. Moreover, the formed

coating layers varied in type and composition (which resulted differently in corrosion protection) and morphology (or surface roughness). The influences of those surface parameters on osteoblasts are discussed later.

3.2.2. Experiment procedure

a. Sample preparation

In this chapter, the used ZK60 substrates were as same as the substrates in the previous chapter. The uncoated ZK60 samples were prepared by grinding mechanically with SiC abrasive papers from 500 grits to 4000 grits, cleaned with ethanol and then dried in air. The coated samples were prepared by applying the chemical conversion coating method with the coating solutions of pH 6.5, 7.8 and 10.2. The samples were kept in a vacuum environment for further use.

b. Cell culture tests

To examine the *in vitro* biocompatibility of the samples coated at different pH conditions, initially, osteoblastic MC3T3-E1 cells (RIKEN Cell Bank) were prepared through thawing and passaged 4 to 5 times. A α-minimum essential medium (α-MEM) supplemented with 10% fetal bovine serum and 1% penicillin/streptomycin solution was used as a culture medium. Before cell seeding, the uncoated and coated samples were sterilized in acetone, then placed in the 12-well plates. The cells were seeded on the samples at a density of 2×10^4 cells/cm^2 in 3 ml of the culture medium in each well and incubated at 37^{0}C with 5% CO_2 for 24 h and 72 h. The cells were also seeded in 12-well plates which is made by polystyrene, functioning as negative control groups. Each type of the samples and the negative control groups were triplicated in the culture test. After the incubation, the cells were fixed on the surface of the samples by methanol and stained by Giemsa solution for cell counting and observation. After this staining process, the samples were cleaned by the purified water, dried completely and kept in a vacuum environment for further investigation. To calculate the cell density, five regions with the same area on the surface of the cultured samples, as illustrated in figure 1, were captured by optical microscope (OM, VHX-5000, Keyence). The number of cells in each region was counted by using ImageJ software. The average cell densities were compared using a one-way analysis of variance (ANOVA). A post hoc test with Bonferroni correction was employed to analyze significant differences between samples. Additionally, the pH value of the culture medium was also measured. Mg ion concentration was quantified by a colorimetric method using xylidyl blue-I [33], [34] using a test kit, Magnesium B-test Wako (FUJIFILM Wako, Japan). The absorption wavelength of the chelate of xylidyl blue-I and Mg ions at 520 nm was measured by a microplate spectrophotometer (Thermo Scientific,

Multiskan Go). The cell morphology and *in vitro* corrosion on the cultured samples were observed by a FE-SEM equipped with an EDS. The ImageJ software was used to measure the nucleus area of the randomly selected cells (n=30) on each type of the samples.

3.2.3. Results

a. Coating results

The XRD and SEM results were taken from the results of the last chapter and shown in figure 3.2 and 3.3, respectively. The precipitated Ca-P coatings have a dual-layer structure, including a dense inner layer and a porous outer layer containing Ca-P crystals. An OCP single phase layer was formed at pH 6.5. This OCP coating has a 1.0 μm inner layer and a porous outer layer containing plate-shaped OCP crystals with a length from 0.9 to 3.6 μm, as shown in figure 3.3 (d) and (g). A HAp single phase layer was formed at pH 7.8, while a HAp layer with an intermediate $Mg(OH)_2$ layer were formed at pH 10.2. In comparison to the OCP coating, the HAp coatings formed at pH 7.8 and 10.2 have a thicker inner layer and a more frequent distribution of the outermost crystals, in figure 3.3 (h) and (i). Rod-shaped HAp crystals with a length of 3.0 μm were observed at pH 7.8, whereas agglomerates of needle-shaped HAp crystals with a length of 1.4 μm were observed at pH 10.2. The needle-shaped crystals of HAp were depicted to have a diameter of several tens of nanometers with a very sharp tip [15]. Moreover, on the surface of the pH 10.2 coating, cracks and displacement among the agglomerates were observed, which were highlighted by black arrows.

b. In vitro cell and corrosion behavior of different coated samples

Figure 3.4 shows the whole surface OM images of the samples with and without calcium phosphate coatings cultured with MC3T3-E1 cells retrieved after 24 h and 72 h. Figure 3.5 indicates the average cell density that counted on the corresponding samples in figure 4 after the cell culture test. After 24 h, the cell density on the uncoated sample showed no statistically significant difference with either the seeding density or the density of the negative control group. However, no cells were observed after 72 h. The cell densities of the samples coated at pH 6.5 and 7.8 were comparable to each other, but both were significantly higher than the seeding density approximately 50 % and 100 % after 24 h and 72 h, respectively. Compared with the negative control group, the cell densities on these two samples showed negligible difference after 24 h but were about twice lower after 72 h. Nevertheless, a decreasing trend of the cell density was observed in the sample coated at pH 10.2. Only about 26.4 % of the seeded cells remained on this sample

after 72 h. The results indicate that the sample coated at pH 6.5 and 7.8 showed a better condition for cell adhesion and proliferation.

Figure 3.6 (a) to (p) reveal the morphology of the cells that adhered to the samples after 24 h and 72 h of the cell culture. On the uncoated sample, the cells showed a small nucleus after 24 h but no cells were observed after 72 h owning to the covered layer of crystallized corrosion products. On the sample coated at pH 10.2, a shrinkage of the cell body was observed since 24 h of the culture test, shown in the cell extension and small nucleus. After 72 h, the cells shrunk severely. On the other hand, the cells which adhered on the sample coated at pH 6.5 and 7.8 manifested elongated morphology and a large nucleus after 24 h and 72 h, suggesting better cell morphology [35]. Figure 3.6 (q) depicts that the average nucleus area of the cells on the sample coated at pH 7.8 is larger than that of the cells on the sample coated at pH 6.5 after either 24h or 72h. It demonstrates that the sample coated at pH 7.8 has a more suitable surface for the osteoblastic cells than that coated at pH 6.5 [35].

In vitro corrosion morphology of the cultured samples after 24 h and 72 h is demonstrated in figure 3.7. After 24 h, localized corrosion was observed on the uncoated sample with microcracks, shown in figure 7 (a). In figure 3.7 (i), dark grey regions of corrosion product of $Mg(OH)_2$ and pits with a depth of 1.9-2.7 μm were observed underneath the surface. After 72 h, the uncoated sample was covered by a layer of corrosion products with a thickness of 3.8-12.1 μm, shown in figure 3.7 (e) and (m). Localized corrosion was observed on the surface of the samples coated at pH 6.5, in figure 3.7 (b) and (f), and at pH 7.8, in figure 3.7 (c) and (g), both after 24 h and 72 h. A thin layer of $Mg(OH)_2$ corrosion product was more clearly observed in the cross-section of the sample coated at pH 6.5, in figure 3.7 (j) and (n), than that of the sample coated at pH 7.8 in figure 3.7 (k) and (o). In the case of the sample coated at pH 10.2, filiform corrosion occurred with the formation of the corrosion product of $Mg(OH)_2$ underneath the coating after 24 h and 72 h. This localized corrosion detached the coating from the substrate, which caused various cracks in a high vacuum environment during SEM observation, shown in figure 3.7 (d) and (h).

Figure 3.8 and 3.9 show the corrosion behavior of the samples under the cell adhesion. Figure 8 demonstrates the pH change of the culture medium for each type of the sample after two culture intervals. After 24 h, the pH value of the medium for the samples coated at pH 6.5 and 7.8 slightly increased to 7.7 and 7.6, respectively. Meanwhile, the pH value of the medium for the samples that was uncoated and coated at pH 10.2 increased notably to 8.2 and 8.1, respectively. After 72 h, the medium for all the samples showed a significant increase in the pH value, compared to the original

pH value (pH = 7.4). The highest increase was observed for the sample coated at pH 10.2, to 8.9, whereas the lowest increase was observed for the sample coated at pH 7.8, to 8.3.

Figure 3.9 depicts the Mg^{2+} ion concentration released into the culture medium owing to the corrosion of the samples. After 24 h, the released amount of the Mg^{2+} ions from the samples coated at pH 6.5 and 7.8 was comparable and approximately triple lower than the released amount from the two other samples. However, the released amount from the samples coated at pH 6.5 and 7.8 showed a great increase after 72 h, to 7.9×10^{-2} and 6.2×10^{-2} mg/cm^2, respectively. Nonetheless, the released amount from the uncoated sample and the sample coated at pH 10.2 raised slightly, to about 10.1×10^{-2} mg/cm^2.

3.2.4. Discussion

It is stated that the cells do not contact directly on the bare surface of a material, but on the surface that previously was adsorbed by water or proteins from the cell culture medium [18]. The cells adhere to the surface of the biomaterial by forming focal contacts based on the adsorbed layer, then spread out, proliferate and eventually differentiate. Therefore, the adsorbed protein layer plays an essential role in the cell response to the biomaterials. In the case of the uncoated samples, the cell density showed no statistically significant difference with the seeding density and the density of the negative control group after 24 h (figure 3.5) even though the sample was corroded to some extent, shown in figure 3.7 (a) and (i). This is because (1) the proteins in the culture medium inhibit the initial corrosion of ZK60 alloy by the discontinuously adsorbed layer and the formation of an insoluble salt layer acts as a local corrosion barrier [36], (2) the abundant amount of Mg ions due to Mg corrosion can result in rapid protein adsorption [36] and (3) Mg ions promote the cells to synthesize protein and DNA and then proliferate [37]. However, it is noted that the cell nucleus was much smaller than the nucleus of the cells adhered to the coated samples, as in figure 3.6 (e). After 72 h, no cells survived on the uncoated sample, shown in figure 3.5. This is attributed to the fast degradation of ZK60 alloy since the adsorbed protein layer is discontinuous, leading to a drastic pH increase in figure 3.8, hydrogen gas evolution and the formation of a thick layer of corrosion products, as in figure 3.7 (e) and (m). Those events limited the cell adhesion, consequently caused the cell death [38], [39].

In contrast, the ZK60 samples covered by the calcium phosphate coatings showed good *in vitro* biocompatibility because organic macromolecules, such as amino acids and proteins, have a high affinity for calcium phosphate apatite surface due to the active Ca and P sites [40] [41] [42], leading to a notable increase in the adsorbed protein layer. The outer layer of the coatings exhibited

high micro-sized porosity, as in figure 3.3, which also benefits for the protein absorption [19]. Hence, the coated samples provided a favorable surface for cell adhesion and then proliferation. Additionally, the calcium phosphate coatings also delayed the occurrence of corrosion, shown in figure 3.8 and 3.9. Therefore, the samples coated at pH 6.5 and 7.8 showed good biocompatibility with a remarkable increase in the average cell density and the extension of the cell body on their surface. However, the cells manifested more elongated shape, which characterizes for the osteoblastic cell line, and a larger nucleus on the sample coated at pH 7.8, as in figure 3.6 (q) although the average cell density showed no statistical significance between the two samples. This is because the formation of focal contacts of the pre-osteoblasts on the rod-shaped HAp crystals of the pH 7.8 coating was better than on the plate-shaped OCP crystals of the pH 6.5 coating [39]. In addition, the sample coated at pH 7.8 was less corroded than that coated at pH 6.5, shown in figures 3.7, 3.8 and 3.9 because of both the lower solubility [43] and a thinner inner layer of the OCP coating compared to those of the HAp coating, shown in figure 3.3 (g) and (h). Therefore, the sample coated at pH 7.8 provided a preferential surface for cell adhesion and growth.

However, the sample coated at pH 10.2 showed low biocompatibility for the osteoblastic cells, although the sample was coated with a HAp layer. The average cell density showed a decreasing trend in figure 3.5 and the cells shrunk severely after 72h in figure 3.6 (p). In our previous study, the induction time for corrosion initiation of this sample is much shorter than the sample coated at pH 6.5 and 7.8 but longer than the uncoated sample [22]. This fast occurrence of filiform corrosion caused the low biocompatibility for the sample coated at pH 10.2. The filiform corrosion caused the formation of large regions of the corrosion product of $Mg(OH)_2$ underneath the coating, in figure 3.7 (l) and (p), the notable increase in the pH value in figure 3.8 and Mg^{2+} ion concentration in the culture medium in figure 3.9, and the H_2 gas evolution. The cell death was caused by the H_2 gas, Mg^{2+} and OH^- ion release (the pH increase), which permeated through the coating layer and cracks [39]. Furthermore, it is noted that in the outermost layer of the pH 10.2 coating, the needle-shaped HAp crystals possessed a diameter of tens of nanometers with a very sharp tip [15]. It is proved that the sharp-tip nanotopography was harmful to the elongation of the cells and led to a decreased in the cell density and cell shrinkage [44]. Moreover, the surface containing high-density nano-particles caused a drastic decrease in the number of the osteoblasts [45]. Hence, the morphology of the pH 10.2 coating also plays an essential role on the low cell proliferation on this sample.

In addition, compared the cell density and corrosion among the samples, it is believed that the coating morphology is more dominant for cell adhesion and proliferation than the corrosion protectiveness of the coating.

3.3. *In vivo* subcutaneous implantation in rabbits

3.3.1. Host response to implant biomaterials

When an implant is introduced, following the tissue injury caused by surgery and blood-material interaction, an adsorption of plasma proteins on the implant surface occurs. The presence of the foreign implant is then recognized by the innate immune system based on the binding and interaction of that adsorbed layer with immune cells [46]. The implant recognition then triggers the inflammation response, including acute and chronic inflammations. Hence, as discussed in the cell-material interaction in Section 3.2.1, *in vivo* environment, the implant surface is also extremely essential for the adherence of the immune cells, which determines the outcome of the implantation.

The acute phase starts the inflammatory response by the presence of neutrophils and monocytes/macrophages (pro-inflammatory M1 phenotype) and usually resolves quickly within one week [46]. Afterward, the chronic phase, where monocytes, macrophages (anti-inflammatory M2 phenotype) and foreign body giant cells (FBGCs) are present, takes place [47]. Monocytes differentiate into macrophages. The fusion of multiple macrophages leads to the formation of FBGCs. M2 macrophages can recruit fibroblasts to the implant surface. The capsule tissue is created by the combination of macrophages/FBGCs, fibroblasts and a build-up extracellular matrix [48]. The formation of this capsule isolates the implant to prevent the surrounding tissues.

The presence of macrophages and FBGCs is said to be the main factor to cause degradation of the implant [49]. As their name, macrophages tend to phagocytize (means “eat”) any foreign body (<5 μm). With larger particles, a group of macrophages fuse into FBGCs with a greater phagocytosis capacity. Another degradation mechanism is macrophages and FBGCs produce erosive enzymes, reactive oxygen and nitrogen species which degrade the implant. Those cells will present at the interface between the local tissues and the implant for the lifetime of the implant, so the degradation is a continuous process [47].

In this study, we simply conducted a subcutaneous implantation in rabbits to estimate the *in vivo* degradation of the alloys to determine their feasibility in clinal use. Based on the results from corrosion and cell culture tests, the alloys coated at pH 7.8 were selected to be examined. The uncoated alloys were also implanted for comparison.

3.3.2. Experiment procedure

The animal experiments were approved by the Science Council of Vietnam Military Medical University, Ministry of National Defense, Hanoi, Vietnam (No. 838/QD-HVQY) and performed at the Animal Center of Vietnam Military Medical University, Ministry of National Defense, Hanoi, Vietnam. The animal (rabbits) were cared according to "Guidelines on Experimental Food or Water Restriction or Manipulation in Laboratory Animals" proposed by University of Michigan, Michigan, America.

The samples uncoated and coated at pH 7.8 were used for the implantation tests. A total of 8 healthy and domestic white rabbits of about 2-2.5 kg in weight and 6-8 months in age were housed in separate cages under controlled living and feeding conditions. The rabbits were randomly divided into two groups, each containing 4 individuals who were employed for one type of samples. Before the surgery, the rabbits were anesthetized with propofol (15-25 mg/kg/h). One side of the hindquarter knees of the rabbits was shaved, then disinfected with betadine 10 % solution. The skin and subcutaneous tissue were opened carefully layer after layer. The samples were placed in the hindquarter knee muscle. One sample was implanted in one rabbit. The subcutaneous tissue was closed by an absorbable bio-suture, while the skin was closed by a nonabsorbable bio-suture. After the wound was closed, the surgical sites were disinfected again with the betadine 10% solution. The rabbits were then returned to their cages. They were looked after carefully and periodically after the surgery. At either the fourth week or twelfth week post-implantation, a secondary surgery was performed to retrieve the samples from the rabbits. Before the secondary surgery, the implanted position on each rabbit was scanned by X-ray radiography (Siemens 100, Germany). The retrieved samples were dried in air, kept under a vacuum condition and characterized by OM, FE-SEM and EDS.

3.3.3. Results

Figure 3.10 (a) to (d) demonstrates radiographic images of the rabbits implanted with the uncoated and coated samples at two different periods post-surgery. At four weeks post-surgery, both kinds of the implanted samples showed a large volume of gas around the sample (figure 3.10 (a) and (b)). The formation of gas cavities around the implanted samples indicates the occurrence of encapsulation of the samples during implantation. Figure 3.10 (e) shows the subcutaneous appearance of the implantation site of the uncoated sample at four weeks post-surgery as an example. The gas cavity formation was observed to cause a local swelling of the host tissue

surrounding the implantation site. At twelve weeks post-surgery, a large volume of gas entrapped in the capsule was still observed around the uncoated sample (figure 3.10 (c)), whereas the gas volume reduced significantly around the coated sample (figure 3.10 (d)).

Figure 3.11 shows microscopy images of the samples implanted in the rabbits for different implantation periods. Since the samples were retrieved without cleaning, the trace of the blood and surrounding soft tissue that adhered tightly to the samples was obviously seen, especially after twelve weeks of implantation, shown in figure 3.11 (c) and (d). After four weeks, the surface of the uncoated sample was observed with some severely corroded regions. On the coated sample, large cracks were visibly observed, pointed out by white arrows. The HAp coating was partly collapsed, in which the remaining region of the coating is in white color, and the collapsed region is in dark color. After twelve weeks, not only the surface but also the edge of the uncoated sample was corroded severely, leading to an irregular shape of the sample. Nonetheless, the coated sample was covered by an inhomogeneous layer. The shape of this sample was kept as the original. The results indicate that the coated sample showed higher corrosion resistance than the uncoated sample.

Figure 3.12 shows the surface and cross-sectional corrosion morphology of the implanted samples. Figure 3.12 (a-1) and (a-2) correspond to the areas 1 and 2 on the sample shown in figure 3.11 (a). Other surface images (b-1) to (d-2) are also in the same manner. The images (e-1) to (h-2) are the cross-sectional view of the areas 1 and 2 on the samples (a) to (d) also in figure 3.11. EDS analyses were carried out on the white frame in the (c-1) to (d-2). For the uncoated sample, there was a highly rough layer of corrosion products in the area 1, whereas the area 2 had a flat surface with numerous cracks. The observed cracks may be caused by the high vacuum condition during SEM observation. For the coated sample, a part of the coating was collapsed at four weeks post-surgery, while localized corrosion was observed on the remaining coating layer, in figure 3.12 (b-1) and (b-2). At twelve weeks post-surgery, this sample was covered by a layer of corrosion products with no observation of the coating, in figure 3.12 (d-1) and (d-2).

In the cross-section observation, for the uncoated sample, pits with a depth of 90–125 μm were observed during implantation, shown in figure 3.12 (e-1) and (g-1). On the other hand, even though pitting corrosion was also observed for the coated sample, the pits were shallower with a depth less than 75 μm, in figure 3.12 (f-1) and (h-1). It indicates a higher corrosion resistance of the coated sample. At twelve weeks post-surgery, a corrosion product layer with a thickness of about 11 μm was covered the coating layer, in figure 3.12 (h-2).

By EDS analysis, the corrosion products containing mainly Mg, Ca, P and O deposited on the surface of the samples, indicating the deposition of Ca/Mg inorganic salts. The high concentration of C might be from soft tissue, protein, amino acid, etc., in the rabbits. The presence of Al element was considered as a contamination because of the use of aluminum tweezer and container during the surgeries. Additionally, $Mg(OH)_2$ corrosion product was found mainly in the pitting area. The formation of $Mg(OH)_2$ underneath the HAp coating layer indicates the penetration of the body fluid through the coating, which led to the corrosion of the ZK60 alloy, in figure 3.12 (f-2) and (h-2). Regarding to the composition of the corrosion product layer in figure 3.12 (h-2), it is reported that in the corrosion product layer formed under the activities of macrophages, which is the main cause of *in vivo* corrosion, the outer part contained mainly Ca/Mg salts while the inner part contained mainly $Mg(OH)_2$ [50]. It shows an agreement with the EDS analysis on the surface and cross section in this study, in which the surface of the layer contained Mg, Ca, O, P and C (figure 3.12 (d-2)) while $Mg(OH)_2$ presented mainly in the inner part of this layer (figure 3.12 (h-2)).

Figure 3.13 shows the change of the HAp coating formed at pH 7.8 after implantation. The initial distribution of the HAp crystals was frequent, shown in figure 3.13 (a), whereas the latter distribution became more sparsely after four weeks of implantation, as in figure 3.13 (b). Additionally, the HAp crystals in the outermost layer were thinned and shorten, as in figure 3.13 (b), (d) and (e), compared with the original crystals in figure 3.13 (a) and (c). It depicts that the HAp coating was dissolved by the body fluid of the rabbits during implantation. After twelve weeks of implantation, there was no notable change of the coating. It is attributed to the protection of the corrosion product layer covered the coating.

3.3.4. Discussion

The degradation process of an implanted material depends upon the host response which is controlled by the surface properties of the material, resulting in the latter changes in its structure, mechanical properties and performance [18], [46]. Based on the outstanding results of the sample coated at pH 7.8 shown in the cell culture test with the best cellular biocompatibility and corrosion resistance, this sample was selected to be implanted subcutaneously in the rabbit body. The uncoated sample was also implanted to compare. This implantation in rabbits aimed to give an insight into the feasibility and degradation behavior of the ZK60 alloy coated at the optimum condition of pH 7.8. However, the *in vivo* behavior of this sample in hard tissues should be further

examined even though this study pointed out that it showed good *in vitro* biocompatibility with the osteoblastic cells.

In the host response, the capsule tissue is created by the combination of macrophages, fibroblasts and a build-up extracellular matrix [48]. The formation of the capsule around the implant, or the fibrous encapsulation shown in Figure 3.10, separates the implant from the surrounding tissues and body fluid. The isolation of the fibrous capsule and the gas cavities, together with the formation of corrosion products as in figure 3.12, slowed down the corrosion of the implant samples [51]. The degradation of the implanted material is believed to be caused mainly by macrophages [50], [52]. When macrophages adhere to the surface of the implant, they secrete mediators of degradation (reactive oxygen and nitrogen species, degradative enzymes and acid hydrolases) into a privileged microenvironment which was induced between the cell membrane and the surface of the implant [53]. The local corrosion, typically pitting, occurred under this privileged microenvironment. It is stated that the local corrosion occurred in narrow regions with fixed positions of micro-Mg anodes and cathodes (such as impurities, second phases or intermetallic compounds) due to the limited diffusion of the body fluid, which was caused by the adhesion of human immune cells [54]. Therefore, Mg anodes were corroded vertically *in vivo* and caused deep pitting regions shown in figures 3.11 and 3.12. Xia et al. proved that HAp was degraded by macrophages [55]. Moreover, the HAp crystals formed by the employed chemical conversion method exhibit a nonstoichiometric composition with the incorporation of CO_3 in PO_4 sites and Na and/or Mg in Ca sites [56]. Therefore, HAp crystals were degraded *in vivo*, leading to the thinner and shorter crystals after four weeks of implantation, as in figure 3.13. Hiromoto *et al.* also reported that the HAp coating was dissolved locally during the subcutaneous implantation in transgenic mice [54].

Hydrogen gas evolution is an inevitable consequence as the samples were degraded. The initial hydrogen evolution led to the formation of gas cavities. It is reported that the gas cavities caused a decrease in the survival rate of rats [57]. However, in this study, the cavities showed no effects on the survival rate of the rabbits until twelve weeks post-surgery, except for the swelling at the implantation site and discomfort to the rabbits in their daily activities. The volume of hydrogen gas can be reduced because hydrogen gas saturates the adjacent tissues, exchanges with dissolved gasses (nitrogen, oxygen and carbon dioxide) from the adjacent tissues and blood vessels, and diffuses through the skin [58]. While hydrogen gas was exchanged from the inside to the outside of the gas cavities, the samples were continuing to be corroded and further hydrogen gas was evolved. In figure 3.10 (a) and (b), after four weeks of implantation, gas cavities were observed

obviously in both types of the implanted samples although the HAp coating is expected to delay the initial corrosion of the coated sample. The corrosion of the uncoated sample was occurred immediately after implantation, whereas the corrosion of the coated sample was supposed to initiate from the defects of the HAp coating which either already exists or caused during the implantation process, in addition to the activities of the immune cells. In figure 3.10 (c) and (d), the difference in the size of the gas cavities between the uncoated and coated samples was noticeable after twelve weeks of implantation. The significant reduction of gas around the coated sample indicates that the corrosion rate of this sample was delayed remarkably and lower than the exchange rate of hydrogen gas. This decrease in the corrosion rate is attributed to the corrosion protection from the remained HAp coating and the corrosion product layer. $Mg(OH)_2$ can be absorbed poorly in the digestive system and degraded by the acid in form of H_2O_2 released by neutrophils and macrophages [57]. It means that further corrosion of the coated sample can take place.

Hence, with the preferred surface conditions, higher corrosion resistance and a notable reduction of gas cavities at the implantation site, the sample coated at pH 7.8 was presumed to reduce the inflammation level and limit the clinical concerns caused by the high corrosion rate of the uncoated ZK60. However, further investigation related to foreign body reaction should be studied.

3.4. Conclusion

In vitro biocompatibility was studied on several calcium phosphate coatings formed on ZK60 alloy using MC3T3-E1 pre-osteoblasts. The type, surface morphology and corrosion protectiveness of the coatings governed the morphology, adhesion and proliferation of the cells. Among those surface factors, the morphology of the coating is more dominant for cell adhesion and proliferation than its corrosion protectiveness. Compared with the seeding density, the cell density increased about twice on the samples coated at pH 6.5 and 7.8, whereas decreased to about 26.4% on the sample coated at pH 10.2 after 72h. The cells were more elongated and had larger nucleus area on the pH 7.8 coating than on the pH 6.5 coating but shrunk severely on the pH 10.2 coating. The sample coated at pH 7.8 showed the best cellular biocompatibility.

In vivo degradation behavior of the samples that were uncoated and coated at pH 7.8 was studied by the subcutaneous implantation in rabbits. Gas cavities were formed around both types of the samples due to their corrosion after four weeks of implantation. Compared with the uncoated sample, the volume of gas cavities reduced significantly around the sample coated at pH 7.8 after twelve weeks due to its higher corrosion resistance. Pitting was the main corrosion mechanism that

occurred in the rabbit body. The HAp coating was also degraded during implantation, shown by the sparse distribution of the thinned and shortened HAp crystals.

In general, the sample coated at pH 7.8 showed the best cellular biocompatibility and improved notably the corrosion resistance of ZK60 alloy both *in vitro* and *in vivo*. Therefore, ZK60 alloy coated at 7.8 can be a degradable implant for clinical use.

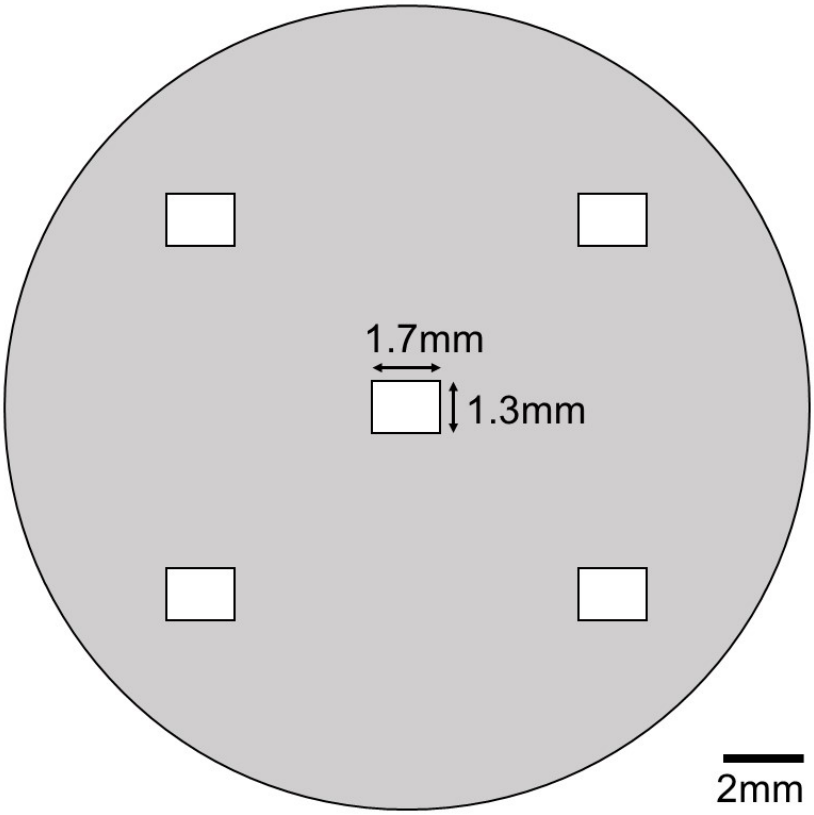

Fig. 3.1: Five places to count cells on each sample after the cell culture test.

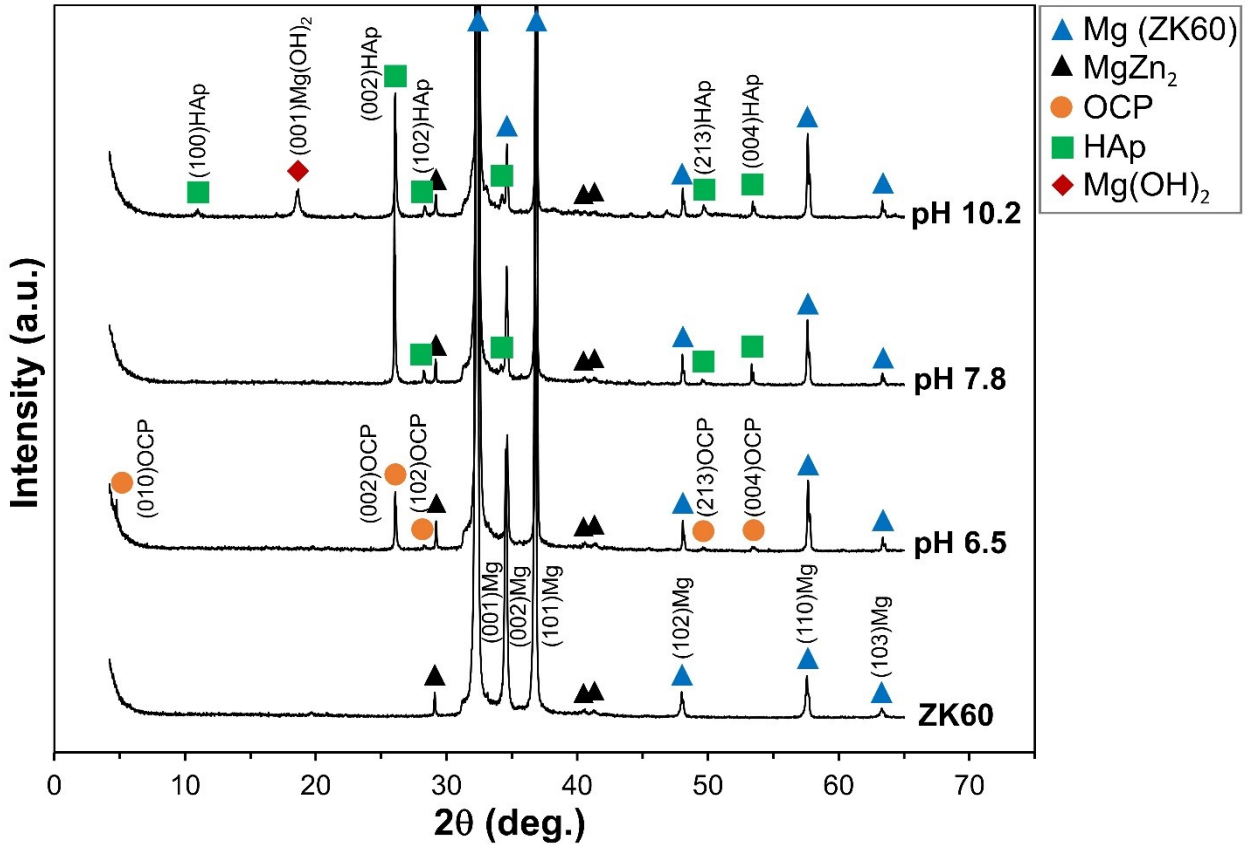

Fig. 3.2: XRD diffraction patterns of the uncoated and coated samples [22].

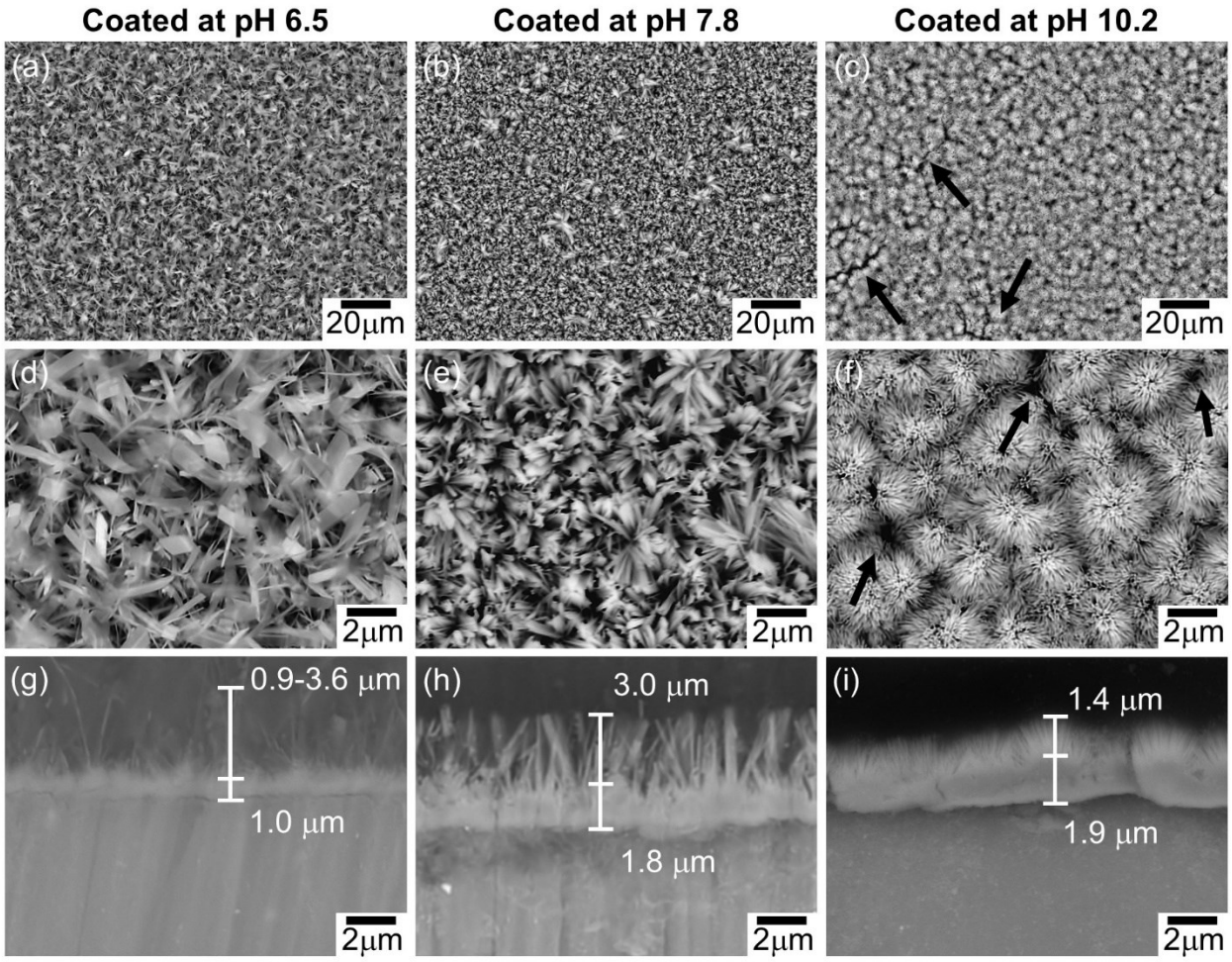

Fig. 3.3: Surface and cross-section SEM images of the samples coated at pH 6.5 ((a), (d) and (g)), at pH 7.8 ((b), (e) and (h)) and at pH 10.2 ((c), (f) and (i)) [22].

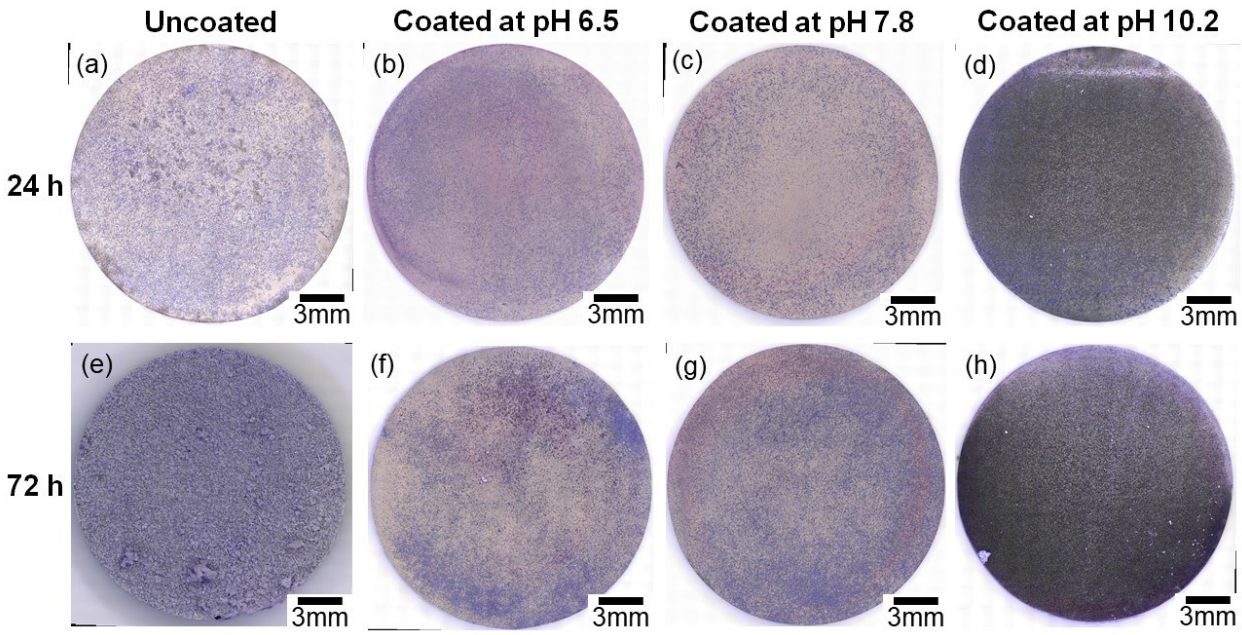

Fig. 3.4: OM images of the samples after 24h ((a) to (d)) and 72h ((e) to (h)) of the cell culture test.

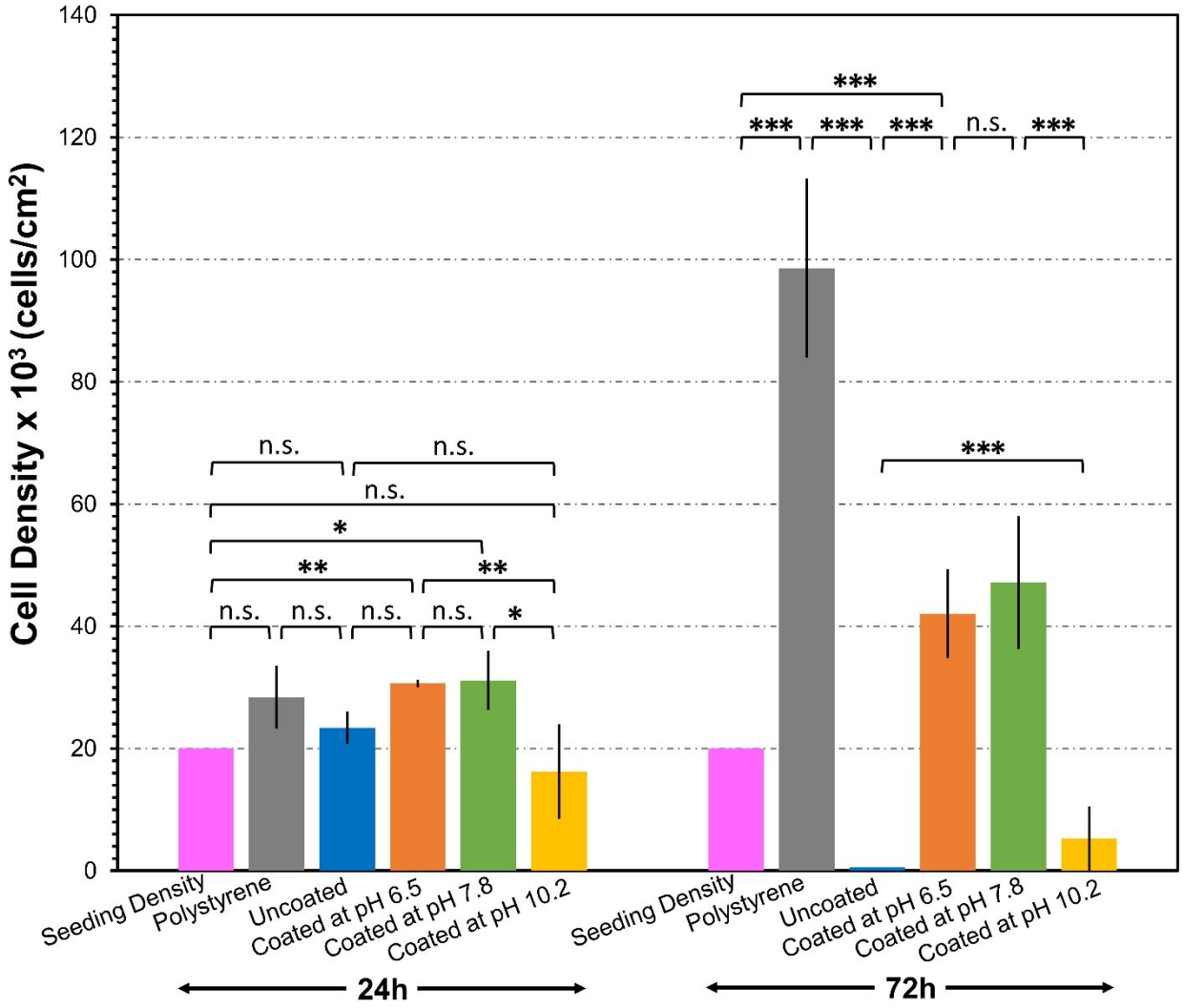

Fig. 3.5: MC3T3-E1 cell density on different types of samples. n.s.: not significant, *: $p \leq 0.1$, **: $p \leq 0.05$, ***: $p \leq 0.001$.

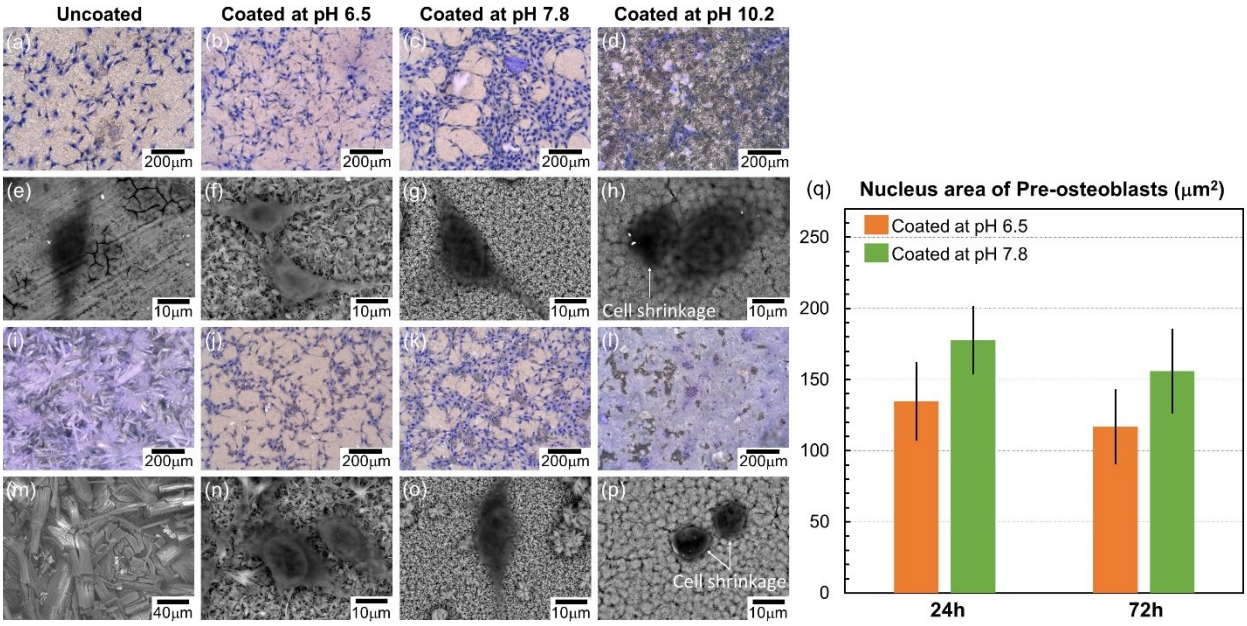

Fig. 3.6: OM ((a) to (d) and (i) to (l)) and SEM ((e) to (h) and (m) to (p)) images of cell morphology on the samples uncoated ((a), (e), (i) and (m)), coated at pH 6.5 ((b), (f), (j) and (n)), coated at pH 7.8 ((c), (g), (k) and (o)) and coated at pH 10.2 ((d), (h), (l) and (p)) after 24h ((a) to (h)) and after 72h ((i) to (p)). (q) the nucleus area of the cells adhered on the sample coated at pH 6.5 and 7.8 after 24h and 72h.

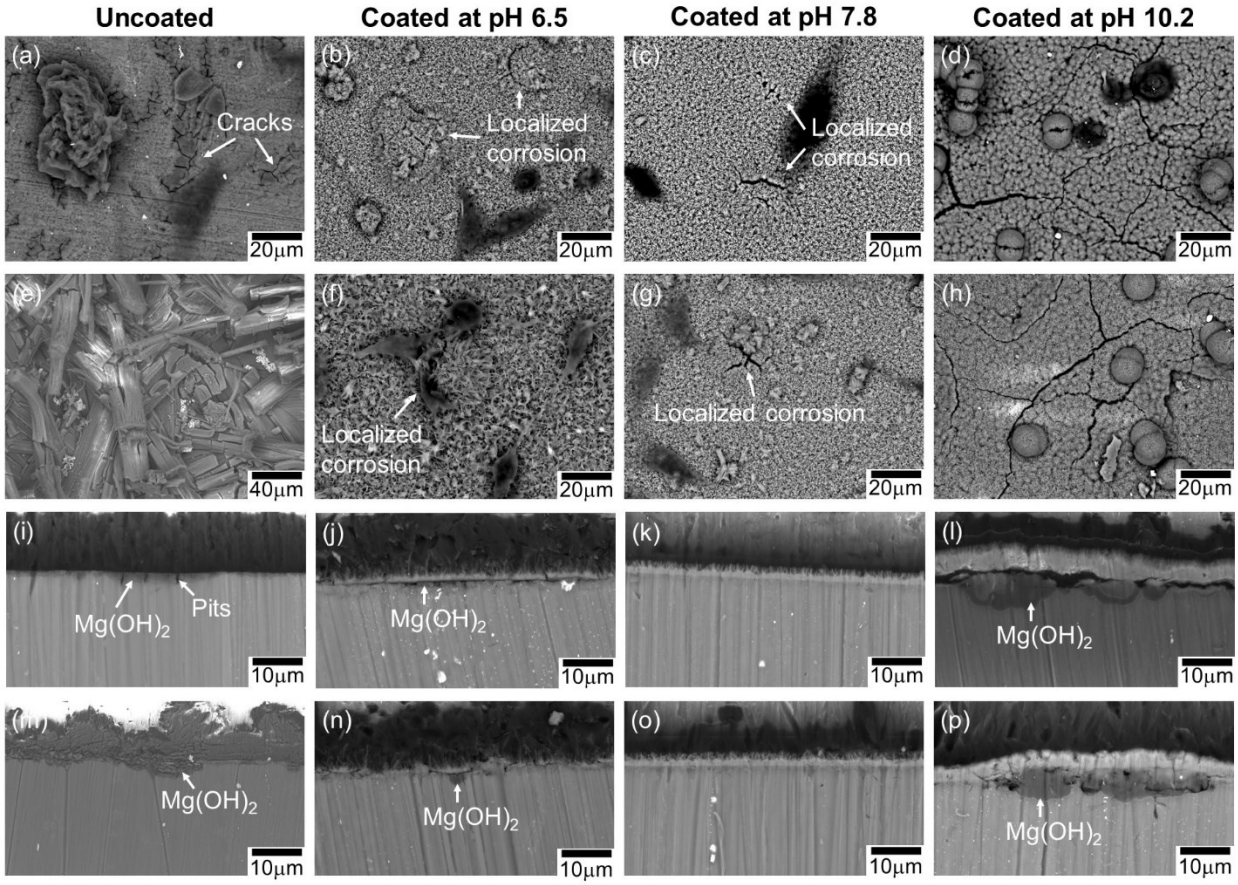

Fig. 3.7: Surface ((a) to (h)) and cross-sectional ((i) to (p)) backscattered SEM micrographs of all the samples uncoated ((a), (e), (i) and (m)), coated at pH 6.5 ((b), (f), (j) and (n)), coated at pH 7.8 ((c), (g), (k) and (o)) and coated at pH 10.2 (d), (h), (l) and (p)) after 24h ((a) to (d) and (i) to (l)) and 72h ((e) to (h), (m) to (p)).

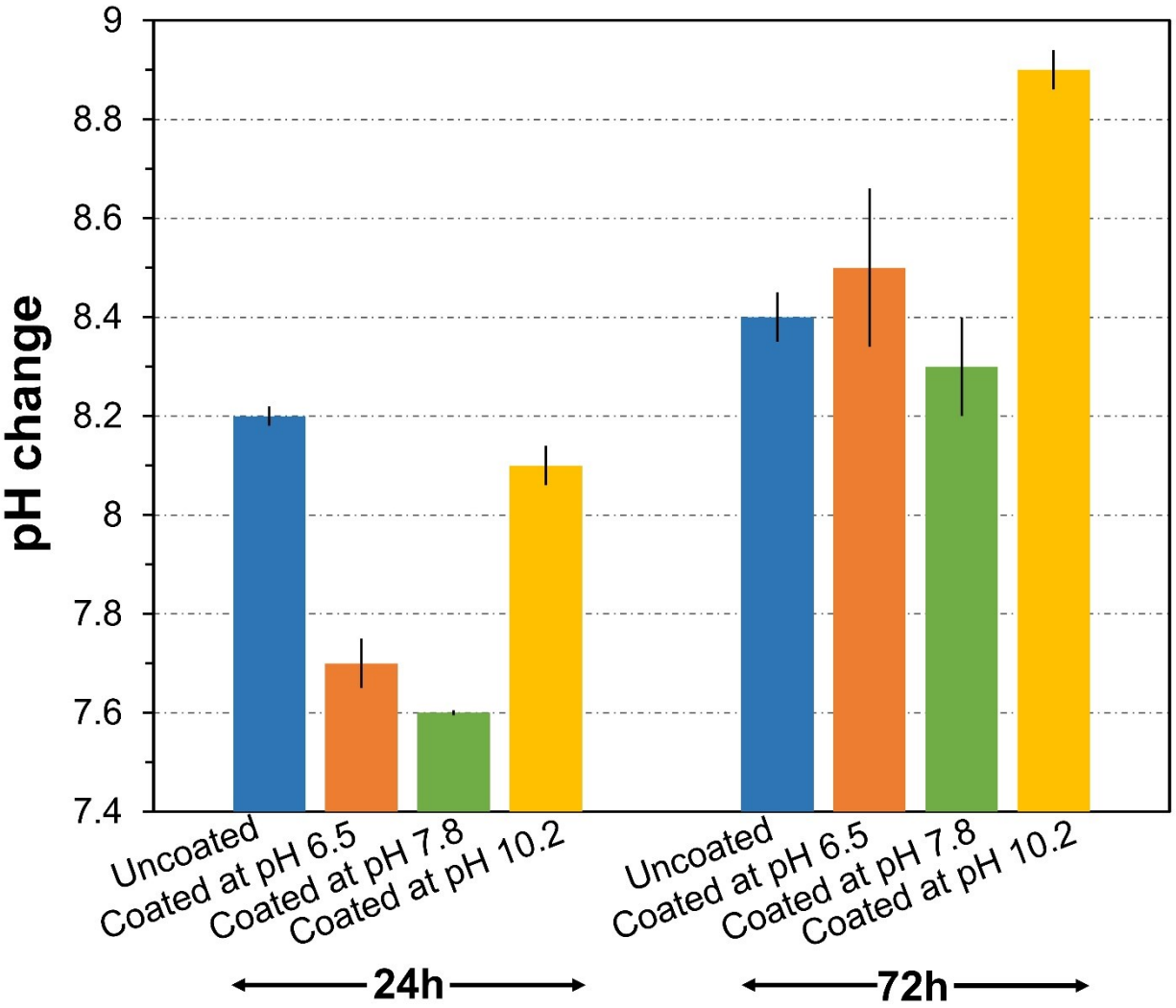

Fig. 3.8: pH change of the medium for all the samples after 24 h and 72h culture.

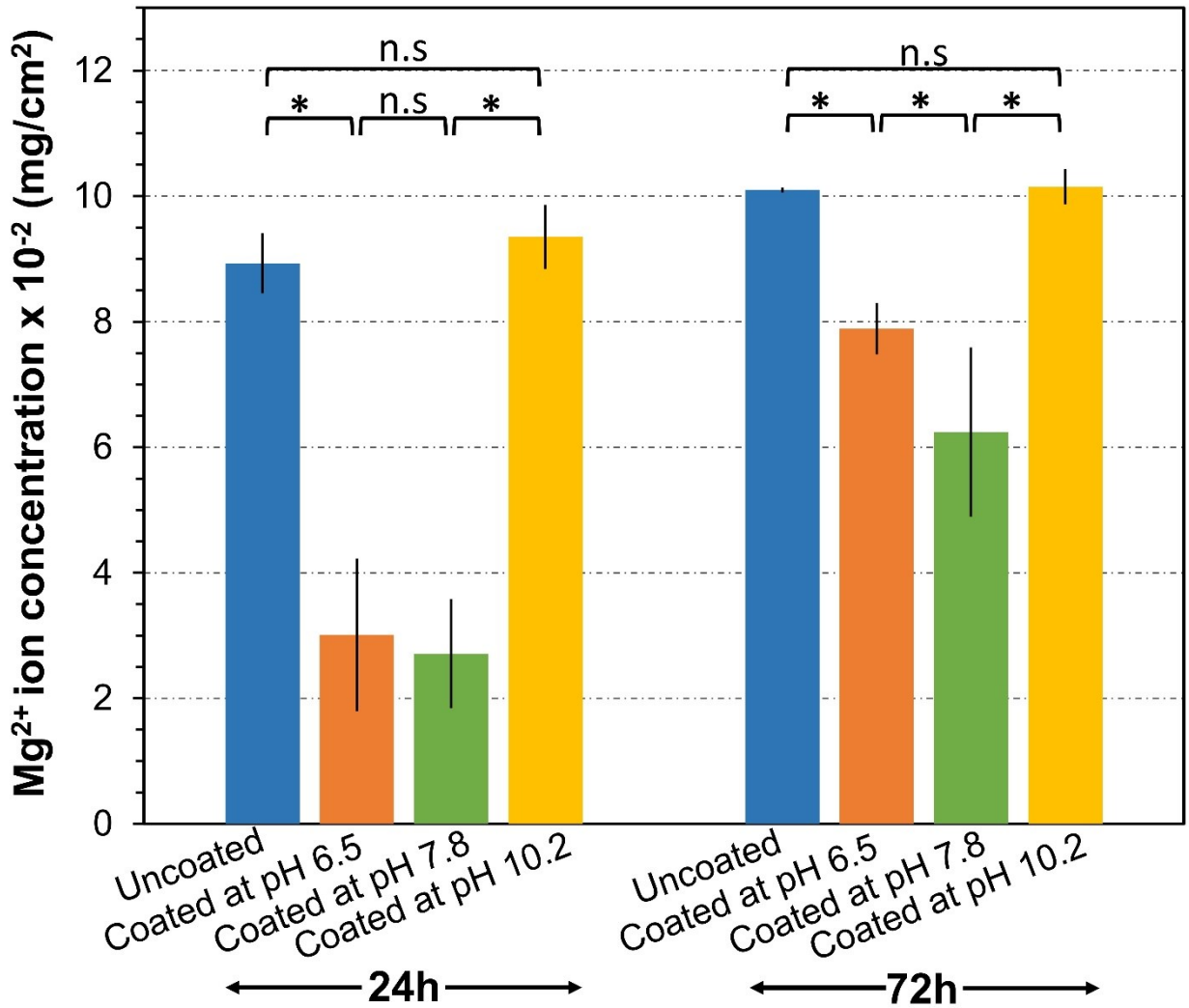

Fig. 3.9: Mg^{2+} ion concentration of the medium for all the samples after 24h and 72h culture. n.s.: not significant, *: $p \leq 0.05$.

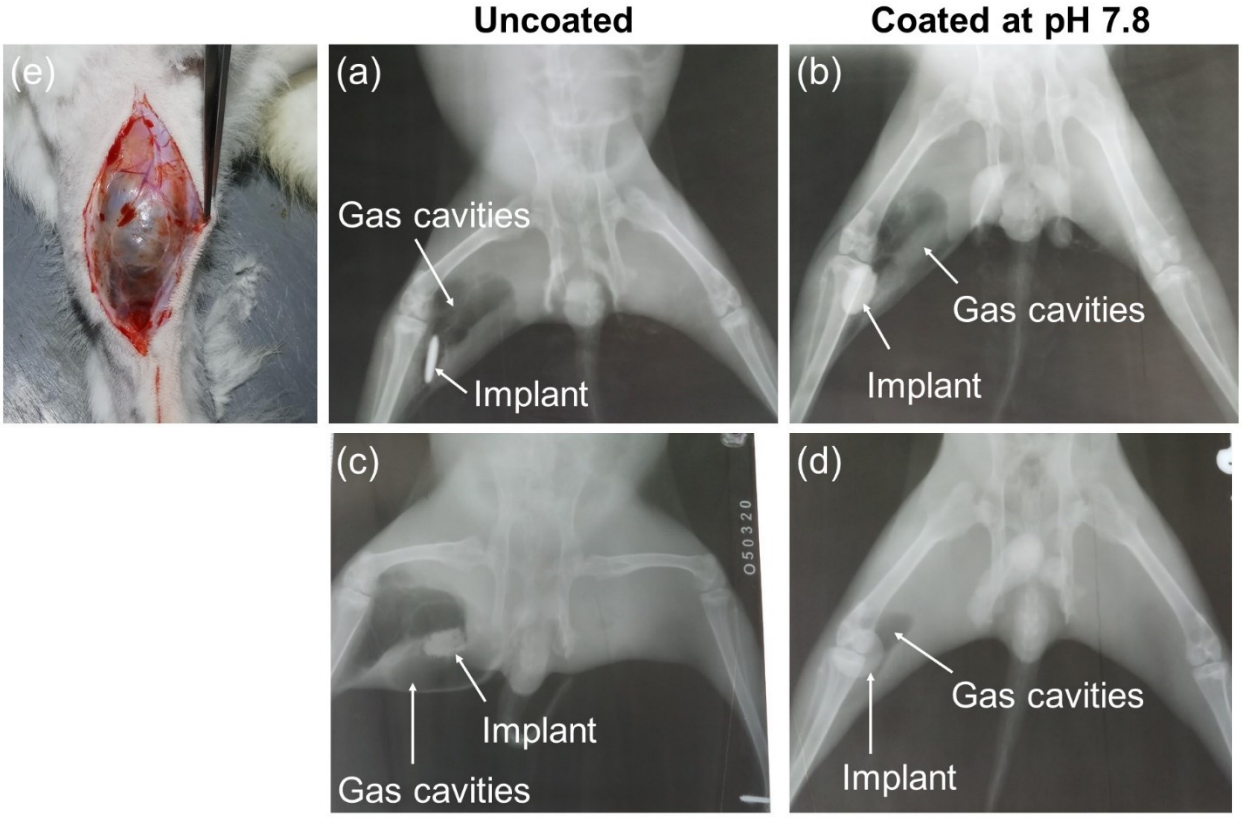

Fig. 3.10: Radiographs of the samples: uncoated ((a) and (c)) and coated at pH 7.8 ((b) and (d)) at four weeks ((a) and (b)) and twelve weeks ((c) and (d)) post-surgery. Subcutaneous appearance of gas cavity at the implantation site of the uncoated sample at four weeks post-surgery (e).

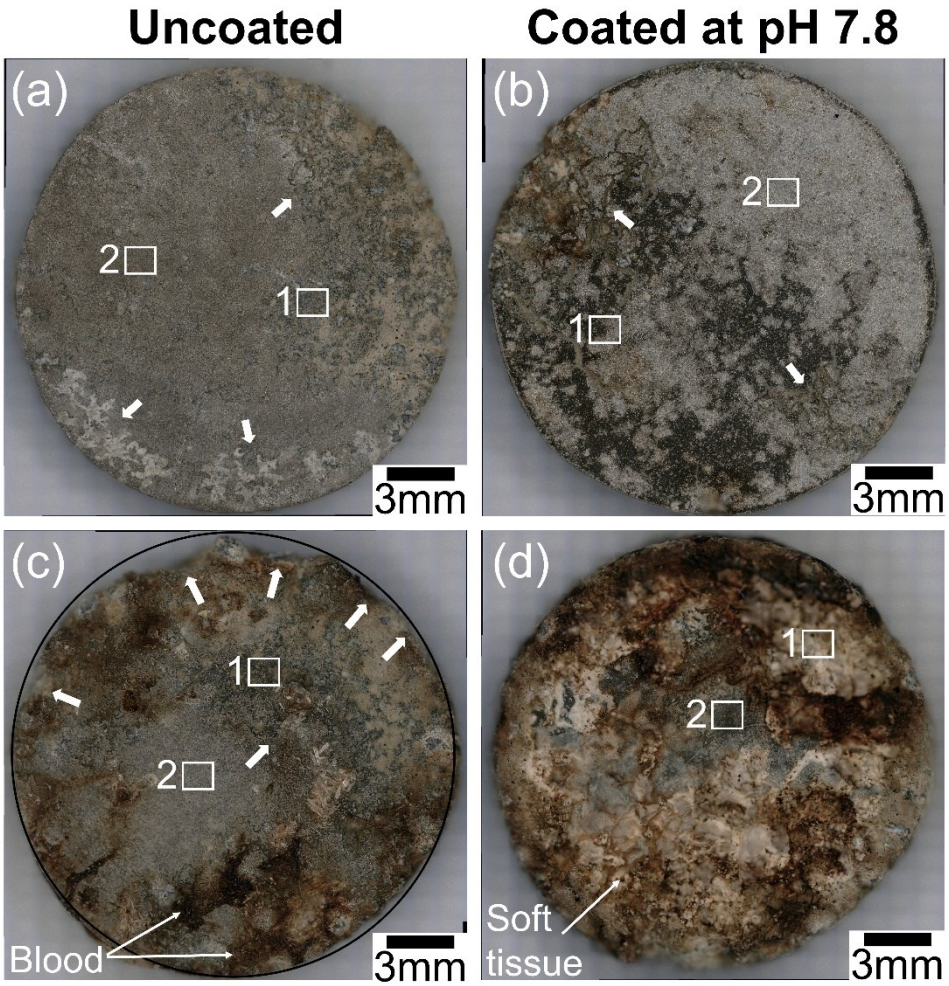

Fig. 3.11: Microscopy images of the sample: uncoated ((a) and (c)) and coated at pH 7.8 ((b) and (d)) at four weeks ((a) and (b)) and twelve weeks ((c) and (d)) post-surgery. White arrows indicate the visible corrosion areas. The black circle corresponds to the original shape of the uncoated sample before implantation. White squares indicate the areas which are subsequently analyzed by SEM.

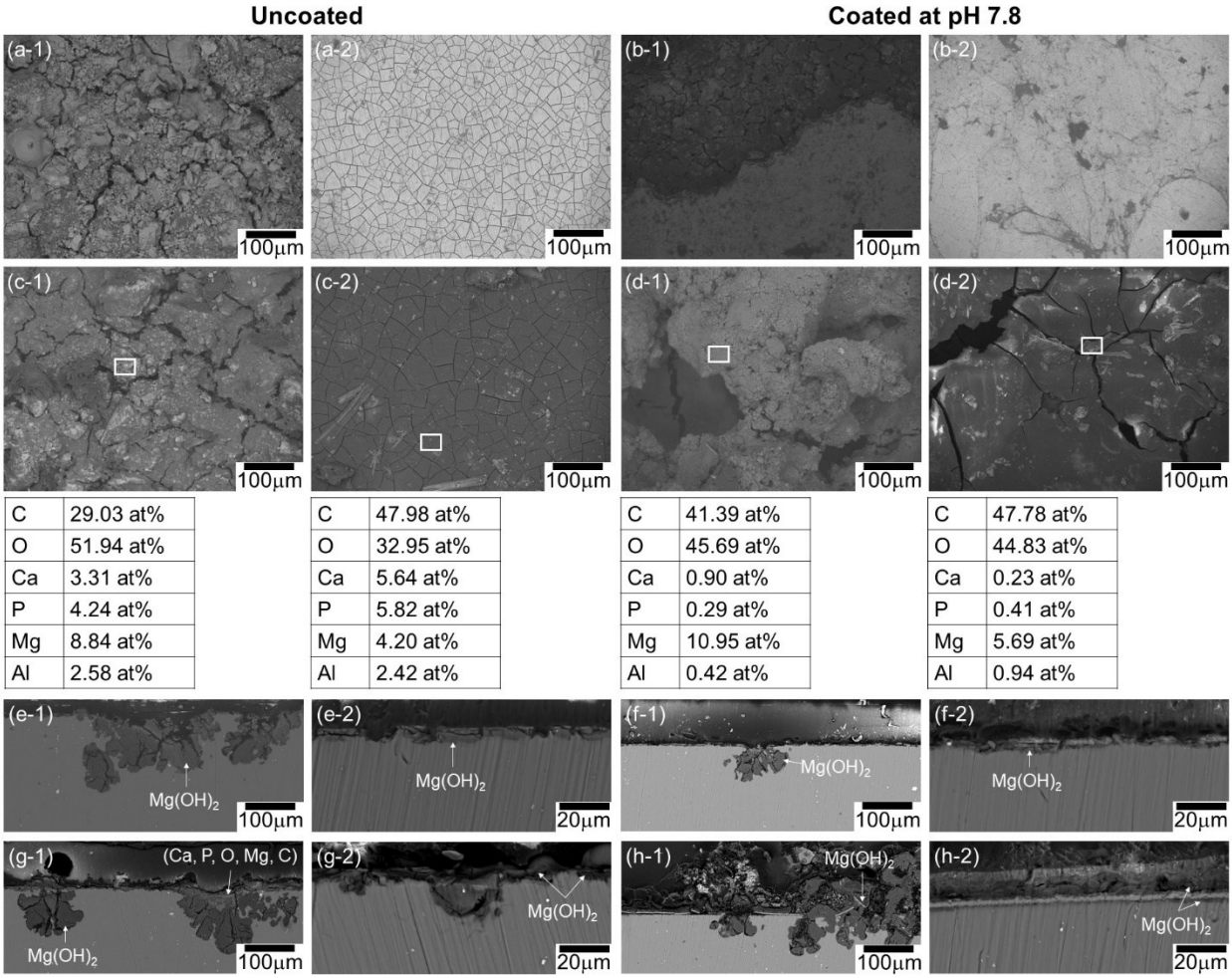

C	29.03 at%
O	51.94 at%
Ca	3.31 at%
P	4.24 at%
Mg	8.84 at%
Al	2.58 at%

C	47.98 at%
O	32.95 at%
Ca	5.64 at%
P	5.82 at%
Mg	4.20 at%
Al	2.42 at%

C	41.39 at%
O	45.69 at%
Ca	0.90 at%
P	0.29 at%
Mg	10.95 at%
Al	0.42 at%

C	47.78 at%
O	44.83 at%
Ca	0.23 at%
P	0.41 at%
Mg	5.69 at%
Al	0.94 at%

Fig. 3.12: Surface and cross-sectional backscattered SEM images of the sample uncoated ((a), (c), (e) and (g)) and coated at pH 7.8 ((b), (d), (f) and (h)) at four weeks ((a) to (d)) and twelve weeks ((e) to (h)) post-surgery.

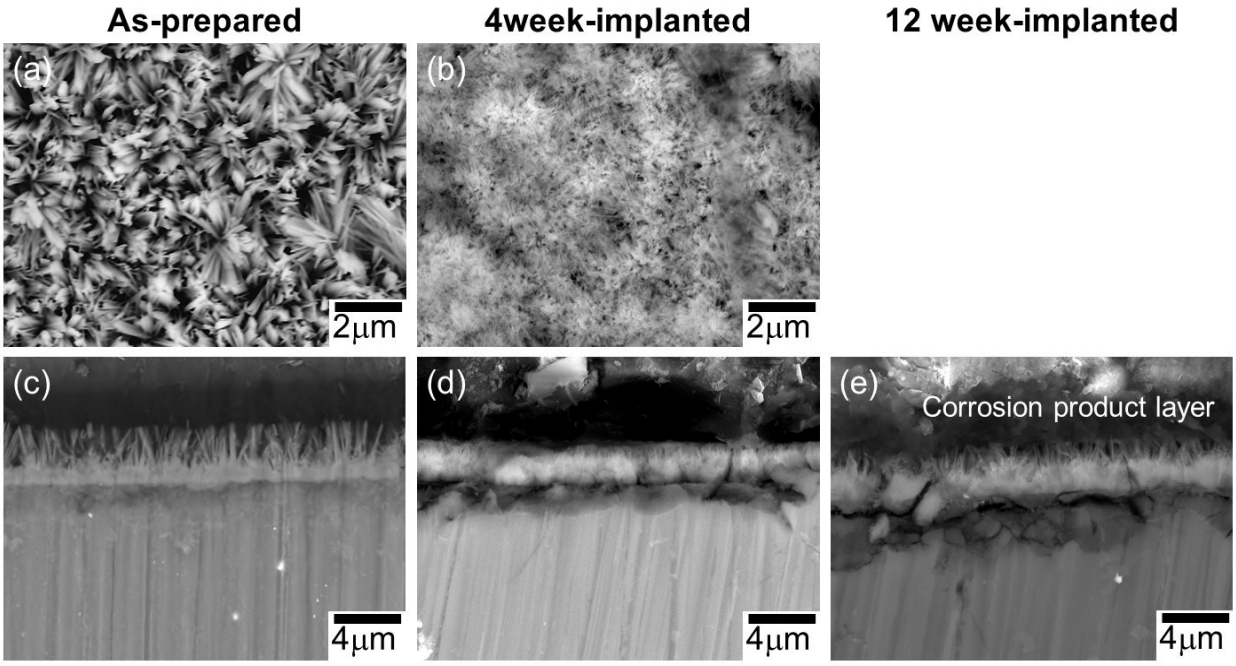

Fig. 3.13: Change of the HAp coating formed at pH 7.8 during implantation: the as-prepared coating ((a) and (c)), the coating after four weeks ((b) and (d)) and twelve weeks (e) of implantation.

References

[1] M. Niinomi, M. Nakai, J. Hieda, Development of new metallic alloys for biomedical applications, Acta Biomaterialia. 8 (2012) 3888–3903. https://doi.org/10.1016/j.actbio.2012.06.037.

[2] S. Kamrani, C. Fleck, Biodegradable magnesium alloys as temporary orthopaedic implants: a review, Biometals. 32 (2019) 185–193. https://doi.org/10.1007/s10534-019-00170-y.

[3] X.N. Gu, N. Li, Y.F. Zheng, L. Ruan, In vitro degradation performance and biological response of a Mg–Zn–Zr alloy, Materials Science and Engineering: B. 176 (2011) 1778–1784. https://doi.org/10.1016/j.mseb.2011.05.032.

[4] Z.G. Huan, M.A. Leeflang, J. Zhou, L.E. Fratila-Apachitei, J. Duszczyk, In vitro degradation behavior and cytocompatibility of Mg–Zn–Zr alloys, J Mater Sci: Mater Med. 21 (2010) 2623–2635. https://doi.org/10.1007/s10856-010-4111-8.

[5] J. Chen, L. Tan, K. Yang, Effect of heat treatment on mechanical and biodegradable properties of an extruded ZK60 alloy, Bioactive Materials. 2 (2017) 19–26. https://doi.org/10.1016/j.bioactmat.2016.12.002.

[6] G. Mani, M.D. Feldman, D. Patel, C.M. Agrawal, Coronary stents: A materials perspective, Biomaterials. 28 (2007) 1689–1710. https://doi.org/10.1016/j.biomaterials.2006.11.042.

[7] G. Song, Control of biodegradation of biocompatable magnesium alloys, Corrosion Science. 49 (2007) 1696–1701. https://doi.org/10.1016/j.corsci.2007.01.001.

[8] D. Zhao, F. Witte, F. Lu, J. Wang, J. Li, L. Qin, Current status on clinical applications of magnesium-based orthopaedic implants: A review from clinical translational perspective, Biomaterials. 112 (2017) 287–302. https://doi.org/10.1016/j.biomaterials.2016.10.017.

[9] R. Radha, D. Sreekanth, Insight of magnesium alloys and composites for orthopedic implant applications – a review, Journal of Magnesium and Alloys. 5 (2017) 286–312. https://doi.org/10.1016/j.jma.2017.08.003.

[10] H. Zhou, L. Yang, U. Gbureck, S.B. Bhaduri, P. Sikder, Monetite, an important calcium phosphate compound–Its synthesis, properties and applications in orthopedics, Acta Biomaterialia. 127 (2021) 41–55. https://doi.org/10.1016/j.actbio.2021.03.050.

[11] X.-J. Ji, L. Gao, J.-C. Liu, R.-Z. Jiang, F.-Y. Sun, L.-Y. Cui, S.-Q. Li, K.-Q. Zhi, R.-C. Zeng, Z.-L. Wang, Corrosion resistance and antibacterial activity of hydroxyapatite coating induced by ciprofloxacin-loaded polymeric multilayers on magnesium alloy, Progress in Organic Coatings. 135 (2019) 465–474. https://doi.org/10.1016/j.porgcoat.2019.06.048.

[12] M. Kazemzadeh-Narbat, J. Kindrachuk, K. Duan, H. Jenssen, R.E.W. Hancock, R. Wang, Antimicrobial peptides on calcium phosphate-coated titanium for the prevention of implant-associated infections, Biomaterials. 31 (2010) 9519–9526. https://doi.org/10.1016/j.biomaterials.2010.08.035.

[13] G.Y. Liu, J. Hu, Z.K. Ding, C. Wang, Bioactive calcium phosphate coating formed on micro-arc oxidized magnesium by chemical deposition, Applied Surface Science. 257 (2011) 2051–2057. https://doi.org/10.1016/j.apsusc.2010.09.050.

[14] S. Hiromoto, A. Yamamoto, High corrosion resistance of magnesium coated with hydroxyapatite directly synthesized in an aqueous solution, Electrochimica Acta. 54 (2009) 7085–7093. https://doi.org/10.1016/j.electacta.2009.07.033.

[15] M. Tomozawa, S. Hiromoto, Microstructure of hydroxyapatite- and octacalcium phosphate-coatings formed on magnesium by a hydrothermal treatment at various pH values, Acta Materialia. 59 (2011) 355–363. https://doi.org/10.1016/j.actamat.2010.09.041.

[16] C. Knabe, R. Gildenhaar, G. Berger, W. Ostapowicz, R. Fitzner, R.J. Radlanski, U. Gross, Morphological evaluation of osteoblasts cultured on different calcium phosphate ceramics, Biomaterials. 18 (1997) 1339–1347. https://doi.org/10.1016/S0142-9612(97)00078-1.

[17] M. Kamitakahara, Y. Uno, K. Ioku, Behavior of osteoblast-like cells on calcium-deficient hydroxyapatite ceramics composed of particles with different shapes and sizes, J Mater Sci: Mater Med. 25 (2014) 239–245. https://doi.org/10.1007/s10856-013-5063-6.

[18] K. Anselme, M. Bigerelle, Role of materials surface topography on mammalian cell response, International Materials Reviews. 56 (2011) 243–266. https://doi.org/10.1179/1743280411Y.0000000001.

[19] S. Samavedi, A.R. Whittington, A.S. Goldstein, Calcium phosphate ceramics in bone tissue engineering: A review of properties and their influence on cell behavior, Acta Biomaterialia. 9 (2013) 8037–8045. https://doi.org/10.1016/j.actbio.2013.06.014.

[20] Y. Fujishiro, T. Sato, A. Okuwaki, Coating of hydroxyapatite on metal plates using thermal dissociation of calcium-EDTA chelate in phosphate solutions under hydrothermal conditions, J Mater Sci: Mater Med. 6 (1995) 172–176. https://doi.org/10.1007/BF00120295.

[21] S. Hiromoto, M. Tomozawa, Hydroxyapatite coating of AZ31 magnesium alloy by a solution treatment and its corrosion behavior in NaCl solution, Surface and Coatings Technology. 205 (2011) 4711–4719. https://doi.org/10.1016/j.surfcoat.2011.04.036.

[22] L.T. Trang, N. Quang Cao, S. Hiromoto, M. O, E. Kobayashi, Formation and corrosion behavior of calcium phosphate coating layers on ZK60 alloy coated at various pH conditions by chemical conversion method, Surface and Coatings Technology. 444 (2022) 128639. https://doi.org/10.1016/j.surfcoat.2022.128639.

[23] Y. Tanaka, S. Nakayamada, Y. Okada, Osteoblasts and osteoclasts in bone remodeling and inflammation, Curr Drug Targets Inflamm Allergy. 4 (2005) 325–328. https://doi.org/10.2174/1568010054022015.

[24] M. Capulli, R. Paone, N. Rucci, Osteoblast and osteocyte: Games without frontiers, Archives of Biochemistry and Biophysics. 561 (2014) 3–12. https://doi.org/10.1016/j.abb.2014.05.003.

[25] S.C. Manolagas, Birth and death of bone cells: basic regulatory mechanisms and implications for the pathogenesis and treatment of osteoporosis, Endocr Rev. 21 (2000) 115–137. https://doi.org/10.1210/edrv.21.2.0395.

[26] A. Rutkovskiy, K.-O. Stensløkken, I.J. Vaage, Osteoblast Differentiation at a Glance, Med Sci Monit Basic Res. 22 (2016) 95–106. https://doi.org/10.12659/MSMBR.901142.

[27] D.G. Castner, B.D. Ratner, Biomedical surface science: Foundations to frontiers, Surface Science. 500 (2002) 28–60. https://doi.org/10.1016/S0039-6028(01)01587-4.

[28] R.G.M. Breuls, T.U. Jiya, T.H. Smit, Scaffold Stiffness Influences Cell Behavior: Opportunities for Skeletal Tissue Engineering, Open Orthop J. 2 (2008) 103–109. https://doi.org/10.2174/1874325000802010103.

[29] D.P. Dowling, I.S. Miller, M. Ardhaoui, W.M. Gallagher, Effect of Surface Wettability and Topography on the Adhesion of Osteosarcoma Cells on Plasma-modified Polystyrene, J Biomater Appl. 26 (2011) 327–347. https://doi.org/10.1177/0885328210372148.

[30] L. Tang, P. Thevenot, W. Hu, Surface Chemistry Influences Implant Biocompatibility, Current Topics in Medicinal Chemistry. 8 (2008) 270–280. https://doi.org/10.2174/156802608783790901.

[31] S. Metwally, U. Stachewicz, Surface potential and charges impact on cell responses on biomaterials interfaces for medical applications, Materials Science and Engineering: C. 104 (2019) 109883. https://doi.org/10.1016/j.msec.2019.109883.

[32] K. Anselme, M. Bigerelle, B. Noel, E. Dufresne, D. Judas, A. Iost, P. Hardouin, Qualitative and quantitative study of human osteoblast adhesion on materials with various surface roughnesses, Journal of Biomedical Materials Research. 49 (2000) 155–166. https://doi.org/10.1002/(SICI)1097-4636(200002)49:2<155::AID-JBM2>3.0.CO;2-J.

[33] C.K. Mann, J.H. Yoe, Spectrophotometric Determination of Magnesium with Sodium 1-Azo-2-hydroxy-3-(2,4-dimethylcarboxanilido)-naphthalene-1´-(2-hydroxybenzene-5-sulfonate), Anal. Chem. 28 (1956) 202–205. https://doi.org/10.1021/ac60110a016.

[34] D. Ratge, K.P. Kohse, H. Wisser, Measurement of magnesium in serum and urine with a random access analyzer by use of a modified xylidyl blue-1 procedure, Clinica Chimica Acta. 159 (1986) 197–203. https://doi.org/10.1016/0009-8981(86)90052-5.

[35] P. Jevtić, L.J. Edens, L.D. Vuković, D.L. Levy, Sizing and shaping the nucleus: mechanisms and significance, Current Opinion in Cell Biology. 28 (2014) 16–27. https://doi.org/10.1016/j.ceb.2014.01.003.

[36] C.L. Liu, Y.J. Wang, R.C. Zeng, X.M. Zhang, W.J. Huang, P.K. Chu, In vitro corrosion degradation behaviour of Mg–Ca alloy in the presence of albumin, Corrosion Science. 52 (2010) 3341–3347. https://doi.org/10.1016/j.corsci.2010.06.003.

[37] H. Rubin, Magnesium: The missing element in molecular views of cell proliferation control, BioEssays. 27 (2005) 311–320. https://doi.org/10.1002/bies.20183.

[38] F. Seuss, S. Seuss, M.C. Turhan, B. Fabry, S. Virtanen, Corrosion of Mg alloy AZ91D in the presence of living cells, Journal of Biomedical Materials Research Part B: Applied Biomaterials. 99B (2011) 276–281. https://doi.org/10.1002/jbm.b.31896.

[39] S. Hiromoto, T. Yamazaki, Micromorphological effect of calcium phosphate coating on compatibility of magnesium alloy with osteoblast, Science and Technology of Advanced Materials. 18 (2017) 96–109. https://doi.org/10.1080/14686996.2016.1266238.

[40] A.L. Boskey, M. Maresca, W. Ullrich, S.B. Doty, W.T. Butler, C.W. Prince, Osteopontin-hydroxyapatite interactions in vitro: inhibition of hydroxyapatite formation and growth in a gelatin-gel, Bone and Mineral. 22 (1993) 147–159. https://doi.org/10.1016/S0169-6009(08)80225-5.

[41] B. Feng, J. Weng, B.C. Yang, S.X. Qu, X.D. Zhang, Characterization of titanium surfaces with calcium and phosphate and osteoblast adhesion, Biomaterials. 25 (2004) 3421–3428. https://doi.org/10.1016/j.biomaterials.2003.10.044.

[42] C. Combes, C. Rey, Adsorption of proteins and calcium phosphate materials bioactivity, Biomaterials. 23 (2002) 2817–2823. https://doi.org/10.1016/S0142-9612(02)00073-X.

[43] L. Wang, G.H. Nancollas, Calcium Orthophosphates: Crystallization and Dissolution, Chem. Rev. 108 (2008) 4628–4669. https://doi.org/10.1021/cr0782574.

[44] C.-H. Choi, S.H. Hagvall, B.M. Wu, J.C.Y. Dunn, R.E. Beygui, C.-J. "CJ" Kim, Cell interaction with three-dimensional sharp-tip nanotopography, Biomaterials. 28 (2007) 1672–1679. https://doi.org/10.1016/j.biomaterials.2006.11.031.

[45] T.P. Kunzler, C. Huwiler, T. Drobek, J. Vörös, N.D. Spencer, Systematic study of osteoblast response to nanotopography by means of nanoparticle-density gradients, Biomaterials. 28 (2007) 5000–5006. https://doi.org/10.1016/j.biomaterials.2007.08.009.

[46] C. Li, C. Guo, V. Fitzpatrick, A. Ibrahim, M.J. Zwierstra, P. Hanna, A. Lechtig, A. Nazarian, S.J. Lin, D.L. Kaplan, Design of biodegradable, implantable devices towards clinical translation, Nat Rev Mater. 5 (2020) 61–81. https://doi.org/10.1038/s41578-019-0150-z.

[47] J.M. Anderson, A. Rodriguez, D.T. Chang, Foreign body reaction to biomaterials, Seminars in Immunology. 20 (2008) 86–100. https://doi.org/10.1016/j.smim.2007.11.004.

[48] A. Carnicer-Lombarte, S.-T. Chen, G.G. Malliaras, D.G. Barone, Foreign Body Reaction to Implanted Biomaterials and Its Impact in Nerve Neuroprosthetics, Frontiers in Bioengineering and Biotechnology. 9 (2021). https://doi.org/10.3389/fbioe.2021.622524.

[49] Z. Sheikh, P.J. Brooks, O. Barzilay, N. Fine, M. Glogauer, Macrophages, Foreign Body Giant Cells and Their Response to Implantable Biomaterials, Materials. 8 (2015) 5671–5701. https://doi.org/10.3390/ma8095269.

[50] J. Zhang, S. Hiromoto, T. Yamazaki, J. Niu, H. Huang, G. Jia, H. Li, W. Ding, G. Yuan, Effect of macrophages on in vitro corrosion behavior of magnesium alloy, Journal of Biomedical Materials Research Part A. 104 (2016) 2476–2487. https://doi.org/10.1002/jbm.a.35788.

[51] N.I. Zainal Abidin, B. Rolfe, H. Owen, J. Malisano, D. Martin, J. Hofstetter, P.J. Uggowitzer, A. Atrens, The in vivo and in vitro corrosion of high-purity magnesium and magnesium alloys WZ21 and AZ91, Corrosion Science. 75 (2013) 354–366. https://doi.org/10.1016/j.corsci.2013.06.019.

[52] C. Chu, L. Liu, S. Rung, Y. Wang, Y. Ma, C. Hu, X. Zhao, Y. Man, Y. Qu, Modulation of foreign body reaction and macrophage phenotypes concerning microenvironment, Journal of Biomedical Materials Research Part A. 108 (2020) 127–135. https://doi.org/10.1002/jbm.a.36798.

[53] P.M. Henson, The Immunologic Release of Constituents from Neutrophil Leukocytes: II. Mechanisms of Release During Phagocytosis, and Adherence to Nonphagocytosable Surfaces, The Journal of Immunology. 107 (1971) 1547–1557. https://www.jimmunol.org/content/107/6/1547 (accessed June 10, 2022).

[54] S. Hiromoto, M. Inoue, T. Taguchi, M. Yamane, N. Ohtsu, In vitro and in vivo biocompatibility and corrosion behaviour of a bioabsorbable magnesium alloy coated with octacalcium phosphate and hydroxyapatite, Acta Biomaterialia. 11 (2015) 520–530. https://doi.org/10.1016/j.actbio.2014.09.026.

[55] Z. Xia, T. Zhu, J. Du, Q. Zheng, L. Wang, S. Li, C. Chang, S. Fang, Macrophages in degradation of collagen/hydroxylapatite(CHA), beta-tricalcium phosphate ceramics (TCP) artificial bone graft: An in vivo study, Chinese Medical Journal. 107 (1994) 845–849. https://doi.org/10.5555/cmj.0366-6999.107.11.p845.01.

[56] N. Ohtsu, S. Hiromoto, M. Yamane, K. Satoh, M. Tomozawa, Chemical and crystallographic characterizations of hydroxyapatite- and octacalcium phosphate-coatings on magnesium synthesized by chemical solution deposition using XPS and XRD, Surface and Coatings Technology. 218 (2013) 114–118. https://doi.org/10.1016/j.surfcoat.2012.12.037.

[57] D. Noviana, D. Paramitha, M.F. Ulum, H. Hermawan, The effect of hydrogen gas evolution of magnesium implant on the postimplantation mortality of rats, Journal of Orthopaedic Translation. 5 (2016) 9–15. https://doi.org/10.1016/j.jot.2015.08.003.

[58] J. Kuhlmann, I. Bartsch, E. Willbold, S. Schuchardt, O. Holz, N. Hort, D. Höche, W.R. Heineman, F. Witte, Fast escape of hydrogen from gas cavities around corroding magnesium implants, Acta Biomaterialia. 9 (2013) 8714–8721. https://doi.org/10.1016/j.actbio.2012.10.008.

Chapter 4:

Mechanical Integrity during Degradation of Calcium Phosphate coated ZK60 alloy

4.1. Introduction

To be successfully used as an orthopedic implant, biomaterials are desired to have good biocompatibility, suitable mechanical strength, corrosion resistance and maintain mechanical integrity during the bone healing process. Biodegradable Magnesium (Mg) alloys have gained increasing attention in temporary orthopedic implant applications because of their ability to dissolve in physiological environment, light weight and avoid stress shielding effect [1], [2], [3]. Especially, Mg-Zn-Zr (ZK) alloy exhibits suitable mechanical properties and contains bio-safe alloying elements. It is reported that Mg-Zn-Zr (ZK) alloys exhibited good biocompatibility [4], [5]. Thus, ZK alloys are suitable biomaterials for implantation. However, Mg is an active metal with a highly electronegative potential so Mg alloys are degraded easily in erosive conditions [6]. This poor corrosion resistance leads to harmful reactions, such as hydrogen gas evolution, local pH increase, loss of mechanical integrity or fracture of implant devices. Hence, it is important to increase the poor corrosion resistance of ZK alloys.

In addition to the demand of higher corrosion resistance, the implant is also required to maintain its mechanical integrity in the initial stage of the healing process. Afterward, the mechanical integrity deteriorates with the degradation of the implant, whereas, the healed bone is gradually gained its normal strength. This behavior is illustrated in Figure 4.1 [7].

Hydroxyapatite (HAp) surface coating is an effective method to both improve corrosion resistance and maintain the mechanical integrity of ZK alloys. Also, HAp coating can enhance biocompatibility of the alloys since HAp is a well-known mineral found in human bone and teeth [8]. In our previous studies, HAp was successfully coated on Mg-6 wt% Zn-0.5 wt% Zr (ZK60) alloy by applying a chemical conversion method at pH 7.8 [9], [10]. The high corrosion rate and biocompatibility of the alloy were improved significantly by the HAp coating. However, the effects of this HAp coating on the mechanical integrity of ZK60 alloy during degradation process have not been investigated yet.

Therefore, this study was carried out to examine the influence of the HAp coating on the mechanical integrity of ZK60 alloy. The degradation of the samples was performed in Hanks solution after several time periods. Compression tests were then conducted to measure mechanical strengths of the degraded samples.

4.2. Experiment procedure

4.2.1. Materials preparation

Commercially extruded ZK60 rods with 31 mm in diameter (Osaka Fuji Industry, Japan) were machined into a rectangular prism with a dimension of 5x5x10 mm^3. The chemical composition of the alloy is shown in Table 4.1. All the surfaces of the samples were ground using abrasive SiC papers up to #4000 grit, cleaned with ethanol, then dried completely for HAp coating process. A ground sample was polished carefully with colloidal silica to observe the distribution of second phases in the alloy, shown in Fig. 4.2.

A chemical conversion coating method was applied to introduce a HAp coating layer on the surfaces of the ZK60 samples. The treatment solution was prepared as the following: (1) mix a same volume of 0.5 mol/L ethylenediaminetetraacetic acid calcium disodium salt hydrate ($C_{10}H_{12}CaN_2Na_2O_8$, Ca-EDTA) solution and 0.5 mol/L potassium dihydrogen phosphate (KH_2PO_4) solution; (2) adjust pH value of the solution to 7.8 by adding 1 mol/L NaOH solution. The treatment solution then heated up. When its temperature reached 90 ^{0}C, the samples were immersed in. The coating treatment was progressed by keeping the temperature stably at 90 ^{0}C during a 2-hour period. After retrieved from the coating solution, the samples were rinsed quickly in distilled water, dried completely at room temperature and stored in a vacuum environment for further analysis and investigation.

Table 4.1: Chemical composition of ZK60 alloy (mass%)

Mg	Zn	Zr	Al	Mn	Si	Ca
Bal.	6.19	0.591	<0.001	0.003	<0.001	0.002
Fe	Ni	Cu	Pb	Sn	Others	
0.002	<0.001	0.003	<0.001	<0.001	<0.3	

4.2.2. Mechanical integrity tests

Both the uncoated and HAp-coated samples were immersed into Hank's solution, whose chemical composition was shown in Table 4.2. The ratio of the total volume of the Hank's solution and the total surface area of the sample was about 50 ml/1 cm^2. The samples were exposed in Hank's solution at a temperature of 37 ^{0}C for 0, 3, 7, 14, 21 and 28 days. After those prescribed immersion periods, the samples were retrieved from the testing solution, cleaned by distilled water and dried in air.

Compression tests were conducted to investigate mechanical integrity of the immersed samples. A strain rate of 1 mm/min was applied for all the samples. Autograph AG-X plus (Shimazdu corporation, Japan) was used. The compression tests were repeated three time for each type of the samples.

Table 4.2: Chemical composition of Hank's solution used in immersion tests

Reagent	Concentration (g/L)	Reagent	Concentration (g/L)
NaCl	8	$MgSO_4.7H_2O$	0.2
KCl	0.4	$NaHCO_3$	0.35
$Na_2HPO_4.H_2O$	0.06	$CaCl_2$	0.14
KH_2PO_4	0.06		

Since the corrosion of the substrate generates Mg ions into Hank's solution, corrosion level of the samples after immersion was carried out by quantifying the released Mg ion concentration. It is given that the initial Mg ions in Hank's solution is about 2 mg/L. Mg ion concentrations released from day 0 to 14 of the immersion tests were quantified by a colorimetric method using xylidyl blue-I [11]. Xylidyl blue-I reacts with Mg^{2+} ions and combine into a water soluble chelate that can be absorbed by light with a wavelength of 520 nm. A test kid (Magnesium B-test Wako, FUJIFILM Wako, Japan) was used to provide xylidyl blue-I. A microplate spectrophotometer (Thermo Scientific, Multiskan Go) was used to measure the absorbance at 520 nm of the chelate of xylidyl blue-I and Mg.

Furthermore, the coating layer and corrosion products formed on the samples after the immersion tests were also removed to investigate surface roughness of the samples after immersion by using a mixture solution of $AgNO_3$ (17 g/L) and CrO_3 (200 g/L). One-shot 3D measuring macroscope (VR-3000, Keyence) was used in this investigation.

4.2.3. Materials characterization

X-ray diffractometry (XRD; Mini Flex, Rigaku) using Cu-K_α radiation was used to characterize the crystal phase of the calcium phosphate coating. A field-emission scanning electron microscope (FE-SEM; JSM-7200F, JEOL) equipped with an energy dispersion X-ray spectrometer (EDS) were utilized to analyze the surface morphology and cross-sectional structure of the coated and immersed specimens. For the cross-sectional observation, both as-coated specimens and immersed specimens were embedded in epoxy resin, grounded with abrasive papers with grits up to #4000 and then cleaned with ethanol.

The experimental processes in this chapter were summarized and illustrated in figure 4.3.

4.3. Results and Discussion

4.3.1. Formation of hydroxyapatite coating

Figure 4.4 (a) shows the XRD diffraction patterns of the uncoated and coated ZK60 alloy Compare to the uncoated sample, the sample coated at pH 7.8 showed the characteristic peak of $(002)_{HAp}$ at about 26^0 (the powder diffraction file of HAp No. 00-009-0432), indicating the formation of HAp layer. Moreover, the diffraction peak from $(001)_{Mg(OH)2}$ was observed at about 18^0 (the powder diffraction file of $Mg(OH)_2$ No. 7-239), suggesting that $Mg(OH)_2$ was formed together with the HAp coating.

Figs. 4.4 (b), (c) and (d) show the surface and cross-sectional SEM images of the HAp coating. The formed coating contains a dense inner layer and a porous outer layer. Leaf-shaped HAp crystals in the outer layer formed radically from the dome-shaped inner layer. Due to this formation, displacement was present among agglomerates of the outermost HAp crystals. In Fig. 4.4 (b), the displacement was pointed out by yellow arrows. The coating has a thickness of approximately 2 μm. The existence of the $Mg(OH)_2$ layer, which was also confirmed by EDS, was observed between the HAp layer and substrate, as shown in Fig. 4.4 (c). This shows an agreement with the previous study [9].

The XRD and SEM results suggest that the HAp coating formed in a similar manner to the calcium phosphate coatings in previous studies [9], [12]. In the initial stage after the exposure of the substrate, corrosion of Mg occurs and hydroxyl ions are generated, leading to a rapid increase of local pH environment. Such rapid local pH increase initiates the dominated and frequent nucleation of HAp, associated with the formation of small amount of $Mg(OH)_2$ as an intermediate layer during the coating duration. The initial HAp forms in dome-shaped precipitates and grew to be a dense inner layer. Afterward, this dense HAp layer moderates the Mg corrosion, resulting in the less frequent formation of HAp. Later, leaf-shaped HAp grows from the dome-shaped precipitates. The distance among the dome-shaped precipitates conditions the growth space for the outermost HAp in the radial direction. This explains for the displacement, pointed out by the yellow arrows in Fig. 4.4 (c).

Additionally, in the XRD patterns of the uncoated ZK60 alloy, in Fig. 4.6 (a), several peaks originated from Mg-Zn second phases were detected in addition to XRD peaks of Mg. The peak with the highest intensity was detected at about 23^0 and other peaks were around 40^0 and 51^0. The

result suggests for a relatively high-volume fraction of the second phases of Mg and Zn in the alloy. Fig. 4.2 shows the size and distribution of the second phase in the ZK60 alloy. The second phase is coarse with diameter of up to about 23 μm and distributes relatively uniformed inside the Mg matrix. Ding *et al.* proved that the coarse size and high volume fraction of the second phases existing in the alloy cause defects of the HAp coating [13]. Typically, the formation of the HAp coating on the second phase particles is retarded, suggesting for the non-uniform growth of the coating, as shown in Fig. 4.2 (b).

4.3.2. Degradation in Hank's solution

Figure 4.5 depicts the accumulated concentration of Mg ions released in Hanks' solution in 14 days. Mg ions are generated when Mg is corroded; therefore, the Mg concentration in the testing solution is representative of the corrosion rate of the alloy. After 3 days of immersion, the HAp-coated sample showed a slightly higher corrosion than the uncoated sample. It means that the corrosion initiation of the coated sample was faster than the uncoated sample. After that, the corrosion rate of the coated sample reduced while that of the uncoated sample increased notably. At day 14 of the immersion test, the coated sample showed a significantly lower corrosion rate than the uncoated sample. The result means that the corrosion of the coated sample was suppressed remarkably after the initial corrosion.

Cross-sectional back-scattered SEM images of the HAp coated samples immersed in Hanks solution were shown in Figure 4.6. Fig. 4.6 (a-) reveals examples of defects presenting in the HAp coating. Fig. 4.6 (a-1) depicts the non-uniformed distribution from the surface image and Fig. 4.6 (a-2) depicts micro-sized cracks from the cross-sectional image of the coating. The chemical composition of point #1 and #2 in Fig. 4.6 (c-1), (d-2), (e-1) and (f-1) was analyzed by EDS and presented in Table 4.3.

The corrosion occurred on the coated sample after 3 days immersion in Hanks solution was shown in Figs. 4.6 (b-1) and (b-2). When the coated sample was immersed into the testing solution, corrosion initiated at the defect sites of the coating [9], [16]. The very thin $Mg(OH)_2$ intermediate layer existing between the HAp coating and the substrate, shown in Fig. 4.4, was then dissolved easily when it contacted with the testing solution which contains Cl^- ions [17]. Later, the substrate was corroded. Localized corrosion was formed and grew vertically, in Fig. 4.6 (b-1). Contemporarily, the dissolution of the $Mg(OH)_2$ intermediate layer propagated horizontally, suggesting the occurrence of filiform corrosion, in Fig. 4.6 (b-2). The filiform corrosion could lead to detachment of the coating from the substrate, leading to further corrosion [9]. Following the

occurrence of corrosion was the formation of $Mg(OH)_2$ corrosion product. As the immersion time increased, localized corrosion occurred more severely to form pits as shown in Figs. 4.6 (c-1), (d-1), (d-2), (e-1), (e-2), (f-1) and (f-2).

The faintly higher Mg ion concentration of the coated sample after 3 days immersed in the Hanks solution compared to the uncoated sample in Fig. 4.5 is believed due to the difference in the corrosion initiation of the samples, which is illustrated in Fig. 4.7. In the case of the coated sample, through cracks existing inside the HAp coating, the testing solution dissolved the $Mg(OH)_2$ intermediate layer and Mg ions were generated as a result (from day 0 to day 3). After the dissolution of this intermediate layer, the substrate was further corroded. Consequently, a new layer of $Mg(OH)_2$ was formed as a corrosion product (up to day 14). This layer later acted as a corrosion protective layer in a short time. Hence, the generation of Mg ions was prevented at this stage. On the other hand, the uncoated sample is naturally covered by a $MgO/Mg(OH)_2$ layer with a thickness of a few hundred nanometers, which is significantly thinner than the intermediate layer of the coated sample [9], [12], [18]. Therefore, the dissolution of this nature layer generated a small amount of Mg ions. After that, the alloy was suffered from initial corrosion leading to the formation of $Mg(OH)_2$ corrosion product which could retard further corrosion for a short time. These events occurred for the first three days of immersion. In the next stage from day 3 to day 14, the $Mg(OH)_2$ corrosion product was dissolved, resulting a great amount of Mg ions released in the testing solution.

Table 4.3: EDS analysis of the coated sample after several immersion periods in Hanks solution

at %	(c-1) – day 7		(d-2) – day 14		(e-1) – day 21		(f-1) – day 28	
	point #1	point #2	point #1	point #2	point #1	point #2	point #1	point #2
Mg	13.87	30.29	12.36	37.31	27.22	24.97	26.29	33.62
Ca	0.13	3.38	0.04	0.01	5.12	0.95	0.43	0.07
O	35.75	57.86	24.67	48.54	39.73	60.08	58.89	55.57
P	0.44	4.46	0.23	0.11	0.20	2.46	1.51	0.27
C	49.69	3.62	62.58	13.73	17.20	11.27	11.78	9.86

EDS analysis detected that in addition to $Mg(OH)_2$, other corrosion products were also formed. They can be calcium phosphate compounds, salts of Mg/Ca and CO_3^{2-}/PO_4^{3-} [19], [20]. Moreover, from 7 days of immersion, the corrosion products were observed to be formed inside the pits, as revealed in Fig. 4.6 (c-1), (d-1), (e-1), (e-2) and (f-1). These corrosion products can act as corrosion barriers to retard the further corrosion [9]. It explains for the slow-down of corrosion

rate of the coated sample after the initial stage of corrosion; meanwhile, corrosion of the uncoated sample progressed severely.

As the immersion periods prolonged, pitting developed deeper, shown in Figs. 4.6 (c-1), (d-1), (e-1) and (f-1). The depth of pits was up to several hundred micrometers after 28 days of immersion, in Fig. 4.6 (f-1). Additionally, the HAp layer was observed along the curve of the pit, shown in Fig. 4.6 (f-3), suggesting the substrate was protected from corrosion to some extent by the remaining coating.

4.3.3. Mechanical integrity investigation

Figure 4.8 shows the change of mechanical properties of the samples after various immersion intervals. Figs. 4.8 (a) and (b) show stress-strain (SS) curves of the uncoated and coated samples, respectively. Figs. 4.8 (c), (d) and (e) show the comparison of ultimate compressive strength (UCS), yield strength at 0.2% and elongation to fracture; respectively, between the uncoated and coated samples. It could be seen that the UCS of both types of the samples decreased as the immersion time increased, as shown in Fig. 4.8 (c). From 0 to 14 days of immersion, the UCS decreased slightly. The initial decreasing rate of the uncoated sample is faintly higher than the rate of the coated sample, in Fig. 4.8 (c-1). In comparison, from day 14 to day 28 of immersion, the UCS of both sample types declined with a higher rate, compared to the initial decreasing rate. Based on the average values, the later decreasing rate of the coated sample is about double the rate of the uncoated sample, in Fig. 4.8 (c-2). However, due to standard deviation, the difference between these rates of the uncoated and coated samples is negligible. After 28 days of immersion, the UCS of the uncoated sample reduced by 29.02±4.67 % to 391.52±18.3 MPa while the UCS of the coated sample reduced by 32±4.94 % to 368.28±18.2 MPa.

In comparison to the UCS, compressive yield strength (CYS) and elongation to fracture just showed a common decreasing trend with an increase in the immersion time. The CYS of the uncoated reduced by about 10.86 % to 181.46±4.06 MPa while the CYS of the coated sample reduced by about 20.14 % to 155.95±9.08 MPa. Elongation to fracture of the uncoated sample reduced by about 1.6 % to 10.36±0.1 %; whereas, that of the coated sample reduced by about 1.39 % to 10.26±0.7 %. The differences between the uncoated and coated samples varied between the immersion periods.

Figure 4.9 shows the macro images of fracture occurred on the compressed samples. For the samples immersed from day 0 to day 3, the fracture occurred normally at the edge of the sample

with a 45^0 degree according to Schimid's law: $\tau=\sigma cos(\phi)cos(\lambda)$. However, due to the occurrence of corrosion, the fracture occurred in abnormal directions which passed through severe corroded areas. This is obviously observed in the images, pointed out by yellow circles, of the samples immersed in the corrosion solution from day 14 and 28. This shows an agreement with the sudden change of the decreasing rate of the UCS from day 14 to 28.

Figure 4.10 reveals the SEM fracture morphology of the samples after 14 to 28 days of immersion. Figs. 4.10 (a-) to (c-) were captured from the uncoated samples immersed after 14 days in Fig. 4.9 (d-1), 21 days in Fig. 4.9 (e-2) and 28 days in Fig. 4.9 (f-1). Similarly, Figs. 4.9 (d-) to (f-) were capture from the coated samples immersed after 14, 21 and 28 days in Figs. 4.9 (i-2), (j-2) and (k-3), respectively. The yellow arrows carried out the crack initiation found on the fracture surface on the samples. It could be seen that the cracks were initiated mainly at the localized corrosion, especially at pitting. Figs. 4.9 and 4.10 indicate that severe corrosion, typically deep pitting, was the main cause of failure for the compressed samples.

Figure 4.11 shows the trace of pitting and filiform corrosion that occurred on the immersed samples after removing the corrosion products and/or the HAp coating. Figure 4.12 demonstrates the maximum pit height measured from the images in Fig. 4.11. It could be seen that the coated sample has slightly deeper pits than the uncoated sample. The result suggests that the coated sample is somewhat more susceptible to crack than the uncoated sample. However, this did not show clear effects on the UCS and elongation, with exception of the CYS.

In general, localized corrosion, shows an important impact on the mechanical integrity of the sample because cracks are usually initiated at the deep pits. The HAp coating showed a notable improvement in corrosion resistance of ZK60 alloy. However, the coating exhibited insignificant effect to the mechanical integrity of the alloy under compression tests; meanwhile, a previous study reported that the HAp coating decreased slightly the mechanical integrity under tensile tests [16]. This is because tensile samples are more susceptible to cracks than compressed samples. Additionally, the occurrence of stress corrosion cracking is difficulty observed in the fracture of the samples because ZK60 alloy is a brittle material, shown in the fracture morphology in Fig. 4.10. Interestingly, after 28 days of immersion, the remained mechanical strength of the coated sample, UCS=368.28±18.2 MPa and CYS=155.95±9.08 MPa, are much higher than those values of human cortical bone, UCS=150-205 MPa and CYS=115.06±16.36 MPa [21]. It is noted that the corrosion of Mg alloys under *in vitro* environment occurs several times faster than that under *in vivo* environment [22]. Also, the HAp coating improved cellular biocompatibility of the alloy [10].

Thus, the HAp coated ZK60 alloy can be an excellent candidate for biodegradable load-bearing implant.

4.4. Conclusion

In this study, the influence of the HAp coating on the mechanical integrity of ZK60 alloy after several immersion periods in Hanks solution was investigated. The results were concluded as the following:

(1) By chemical conversion coating method, a HAp coating was introduced on the substrate surface. This coating contained a dense inner layer and a porous outer layer with agglomerates of leaf-like HAp particles. Defects, such as cracks, were observed in the coating. A very thin $Mg(OH)_2$ intermediate layer was also formed between the substrate and HAp coating.

(2) The initial stage of corrosion that occurred on the uncoated and coated samples was different. As the immersion time increased, the coated sample showed a significant reduction of corrosion rate, compared to the uncoated sample. Corrosion products played important role in the retardance of corrosion.

(3) In general, the mechanical strength of the samples reduced as the immersion time increased. When mechanical stress was applied, cracks were initiated mainly at deep pits. Although the coated sample had deeper pits than the uncoated did, the difference in mechanical strength between the uncoated and coated sample was negligible. It is concluded that the HAp coating showed almost no effects on mechanical integrity of the ZK60 alloy.

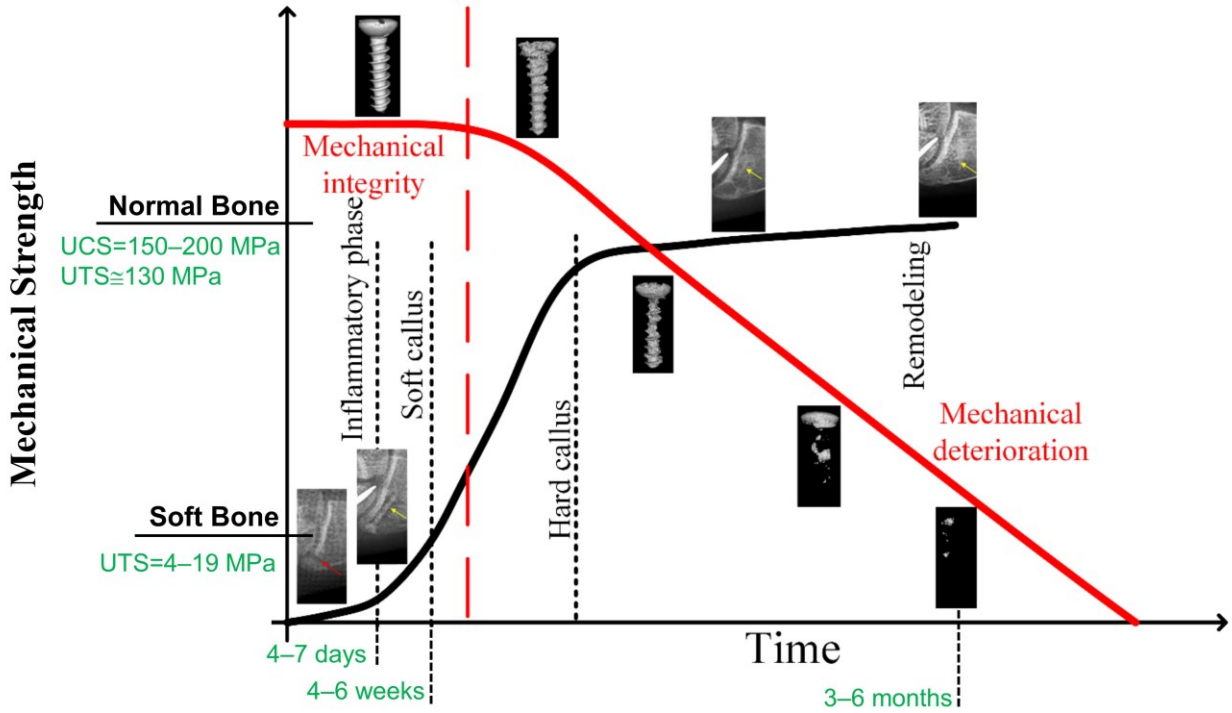

Fig. 4.1: Illustration of mechanical integrity behavior of ideal implant biomaterials during the bone healing process [7], [21].

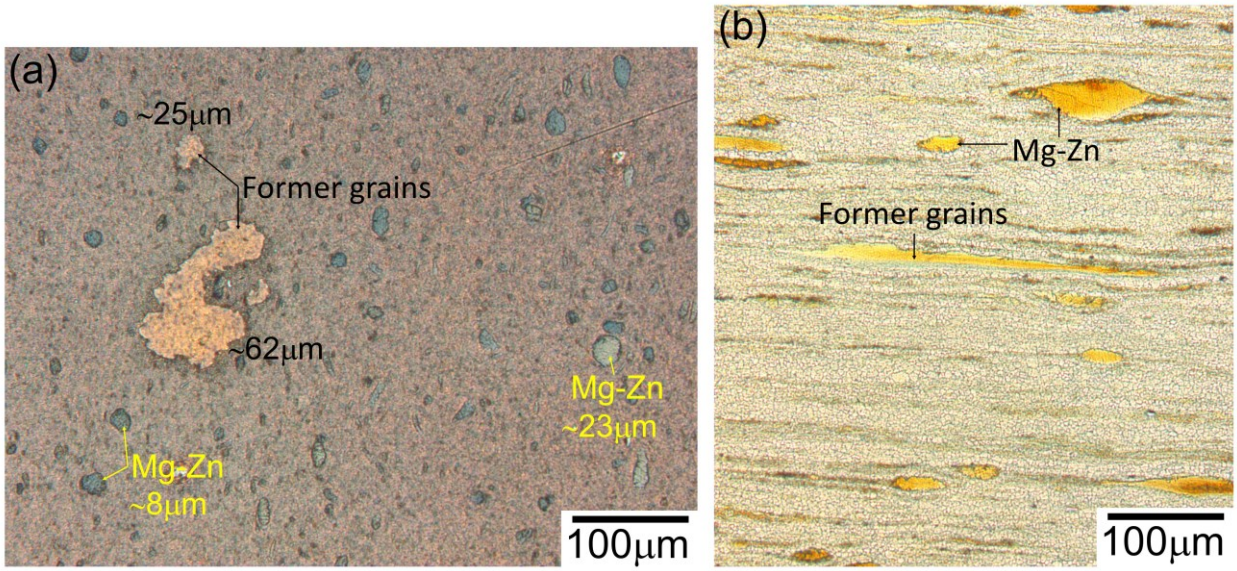

Fig. 4.2: Optical microscope images show (a) cross section and (b) longitudinal section of the as-extruded ZK60 rod.

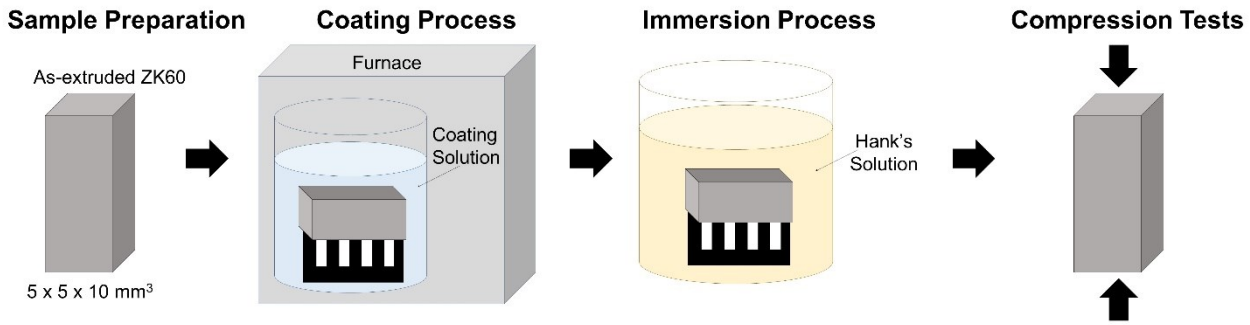

Fig. 4.3: Experimental schematic in this study.

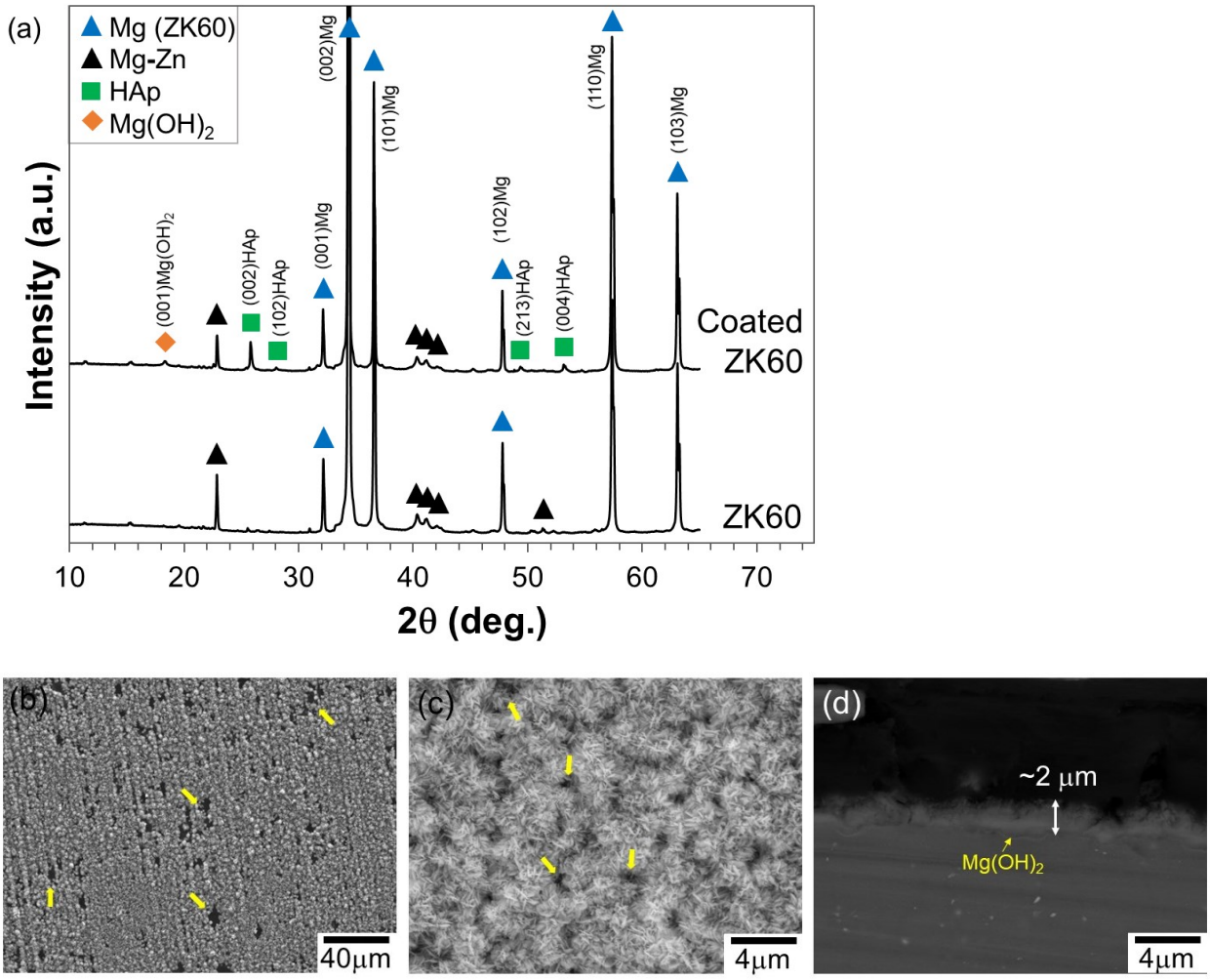

Fig. 4.4: (a) XRD diffraction patterns of the uncoated and coated ZK60 alloy. (b) Surface and (c) cross-sectional SEM images of the formed coating on the substrate.

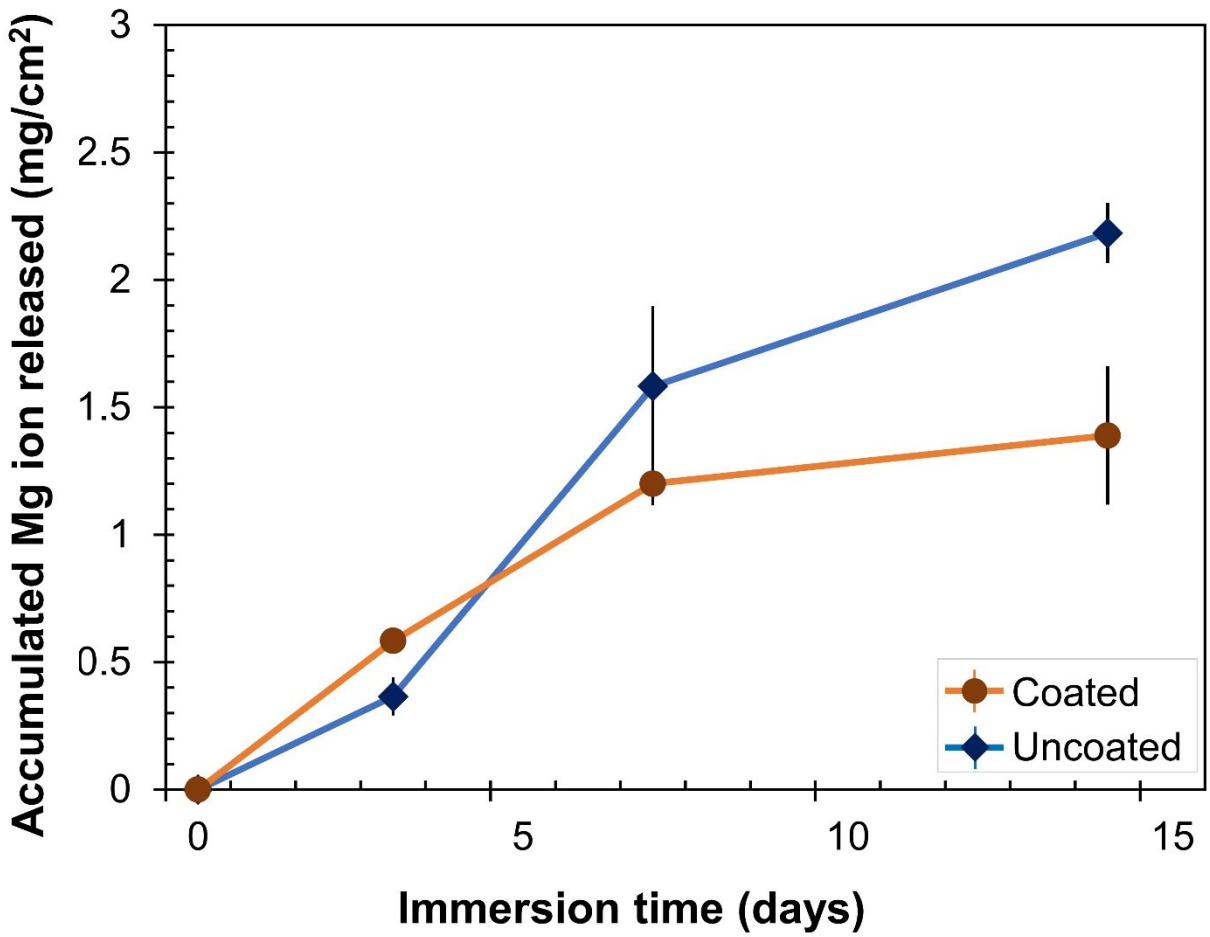

Fig. 4.5: Accumulated concentration of released Mg ions in Hank's solution up to day 14th of the immersion tests. The presented values equal to the mean ± standard deviation (n=3).

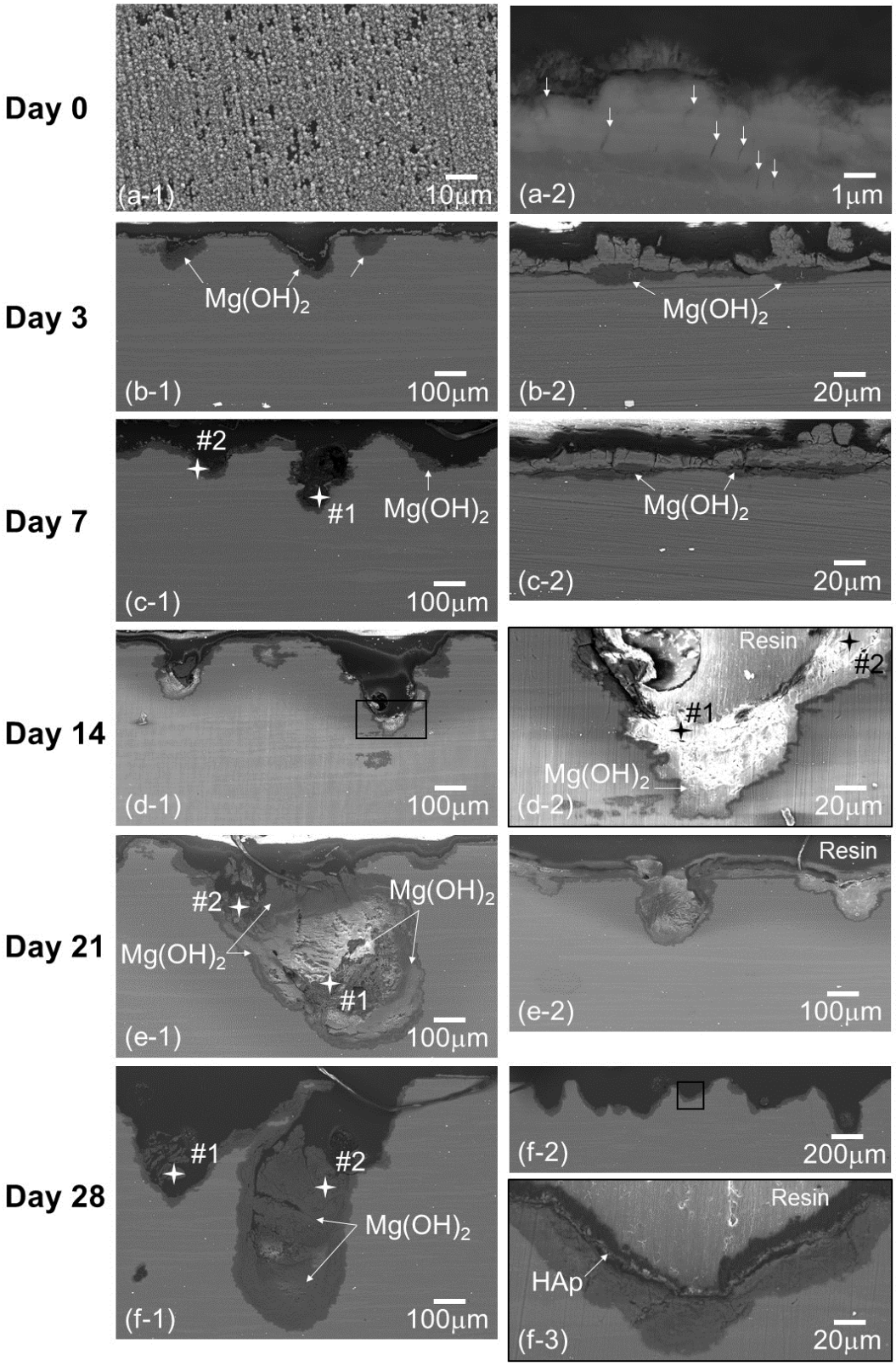

Fig. 4.6: (a-1) Examples of defects on the HAp coating. (a-2) to (f-3) Cross-sectional back-scattered SEM images of the HAp coated samples after different immersion times.

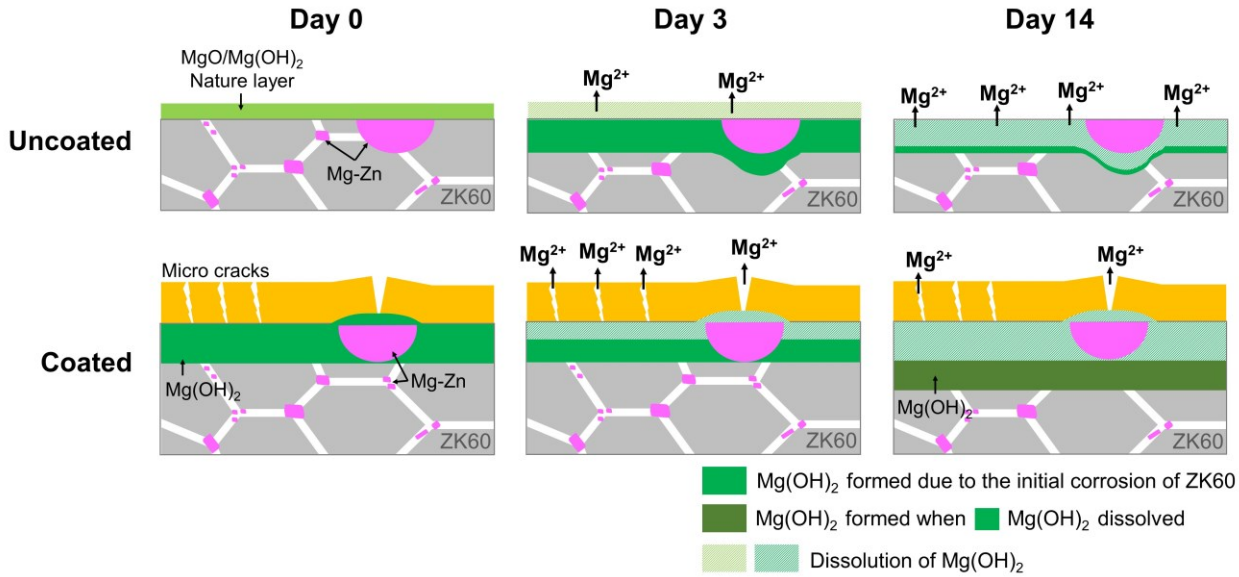

Fig. 4.7: Illustration of the difference in corrosion initiation of the uncoated and coated samples.

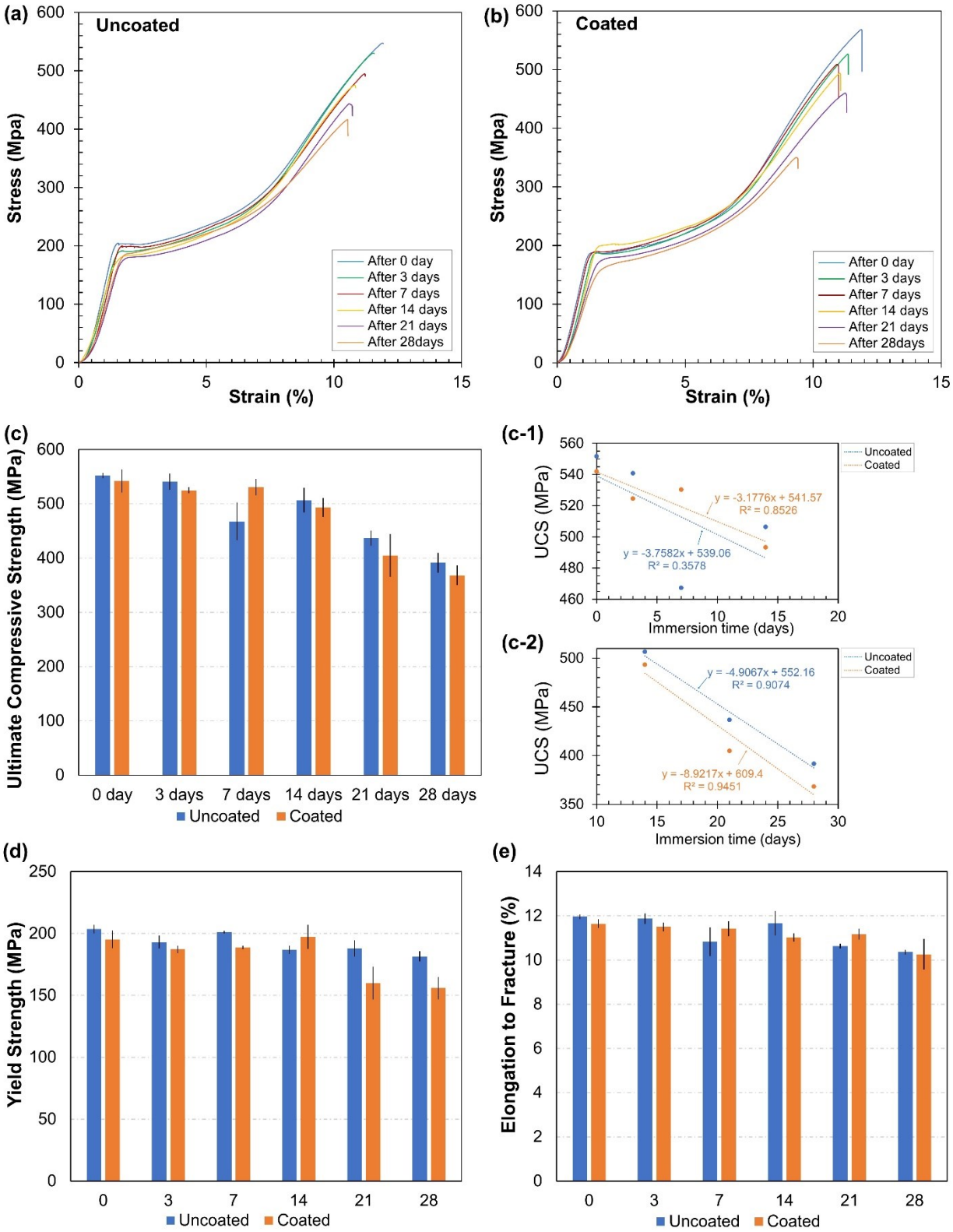

Fig. 4.8: (a) Stress-strain curve of the uncoated samples, (b) Stress-strain curve of the coated samples, (c) Ultimate compressive strength, (c-1) The decreasing rate of UCS from day 0 to 14, (c-2) The decreasing rate of UCS from day 14 to 28, (d) Compressive yield strength and (e) Elongation to fracture

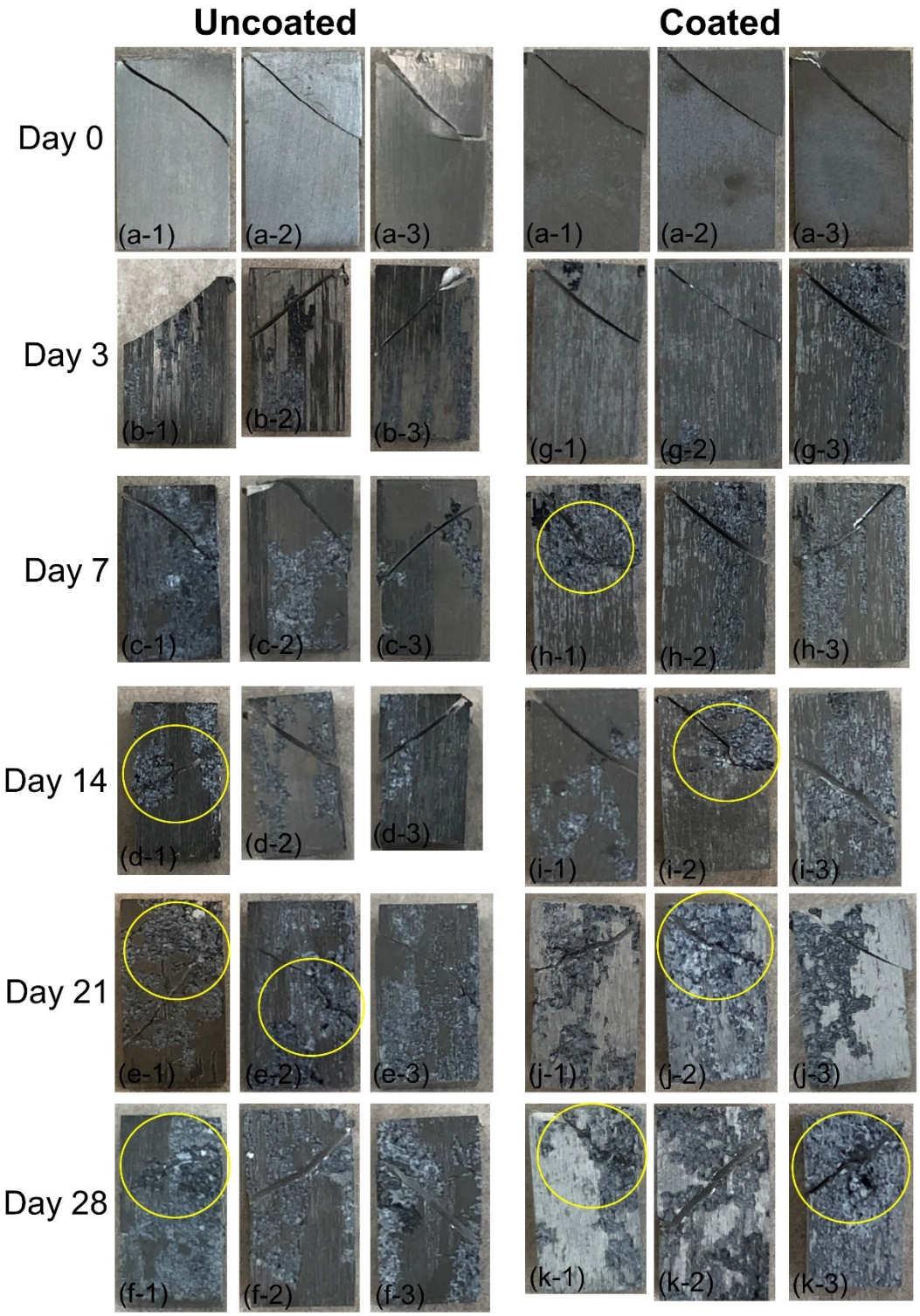

Fig. 4.9: Macro images of the occurrence of fracture in the compressed samples after 0 to 28 days immersion in Hank's solution. Yellow circles pointed out abnormal fracture directions passed through severe corroded areas.

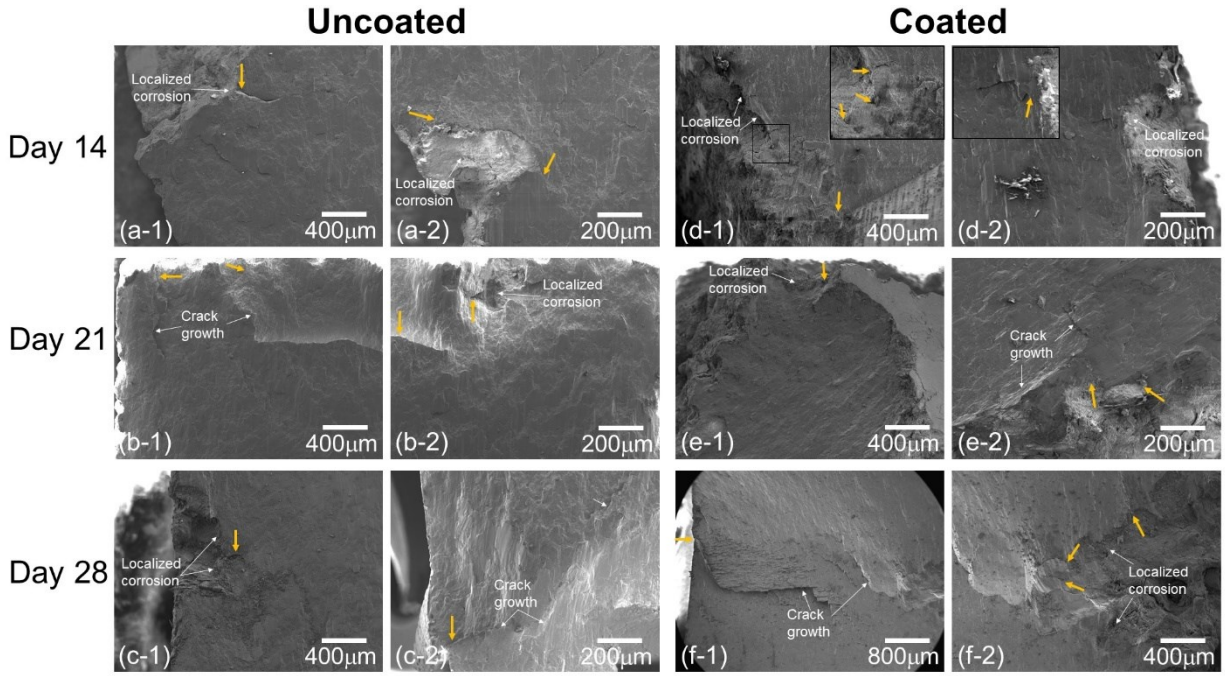

Fig. 4.10: SEM images of fracture morphology of the uncoated and coated samples after 14 to 28 days of immersion in Hank's solution. Yellow arrows pointed out crack initiation.

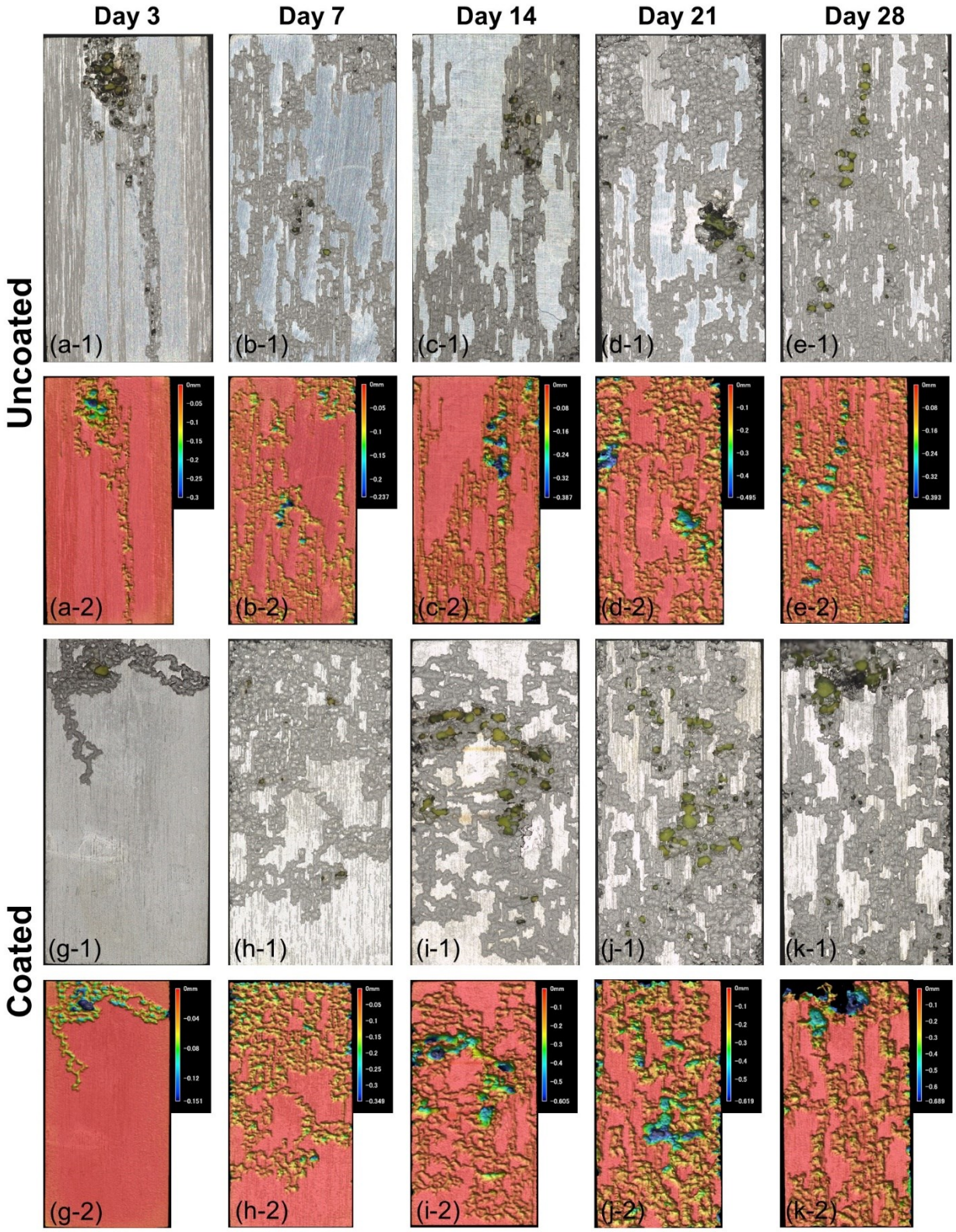

Fig. 4.11: (a-1) to (k-1) Macro images after removing corrosion products and/or the HAp coating and (a-2) to (k-2) 3D microscope images of the surface roughness with the color scale of the uncoated samples (a-1) to (e-2) and the coated sample (g-1) to (k-2).

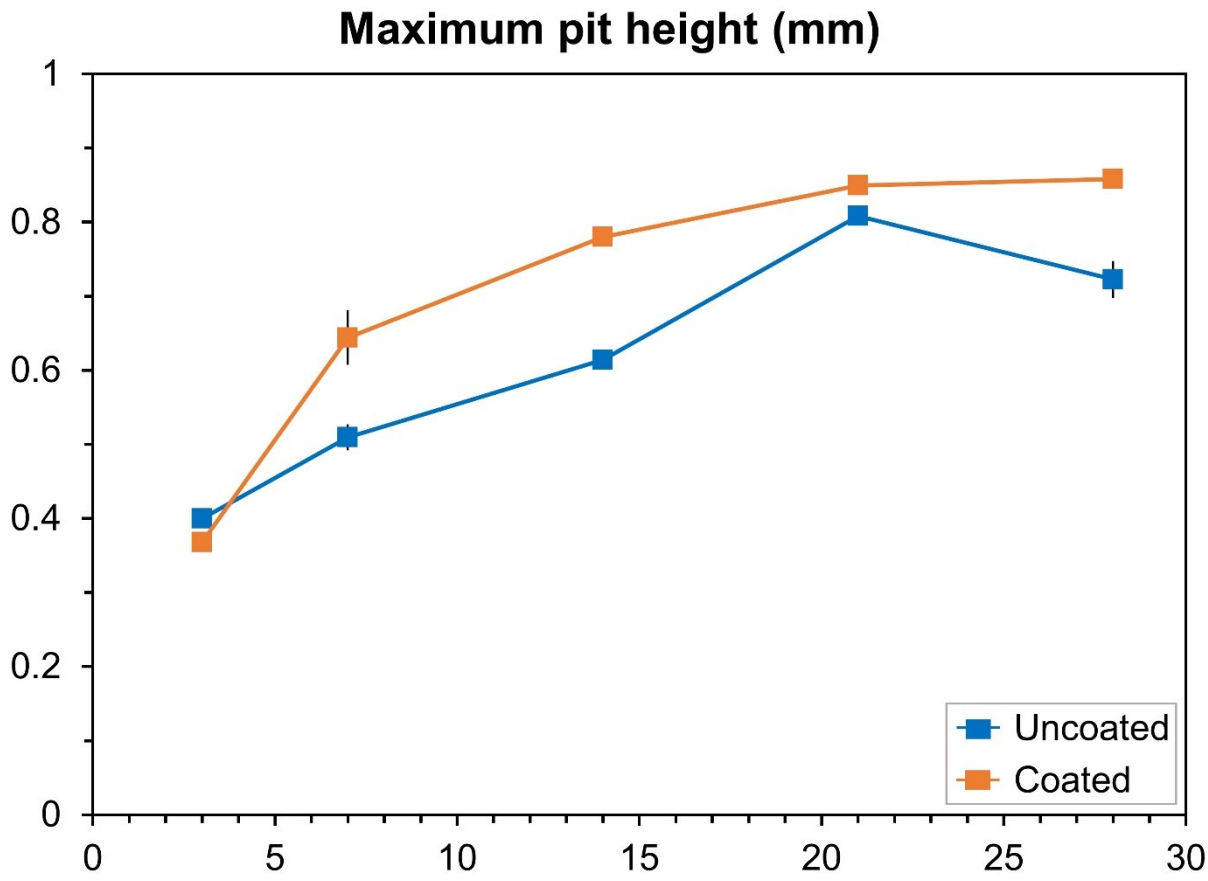

Fig. 4.12: Maximum pit height measured on the uncoated and coated samples shown in Fig. 4.11.

References

[1] M.P. Staiger, A.M. Pietak, J. Huadmai, G. Dias, Magnesium and its alloys as orthopedic biomaterials: A review, Biomaterials. 27 (2006) 1728–1734. https://doi.org/10.1016/j.biomaterials.2005.10.003.

[2] H. Zhou, B. Liang, H. Jiang, Z. Deng, K. Yu, Magnesium-based biomaterials as emerging agents for bone repair and regeneration: from mechanism to application, Journal of Magnesium and Alloys. 9 (2021) 779–804. https://doi.org/10.1016/j.jma.2021.03.004.

[3] S. Kamrani, C. Fleck, Biodegradable magnesium alloys as temporary orthopaedic implants: a review, Biometals. 32 (2019) 185–193. https://doi.org/10.1007/s10534-019-00170-y.

[4] Z.G. Huan, M.A. Leeflang, J. Zhou, L.E. Fratila-Apachitei, J. Duszczyk, In vitro degradation behavior and cytocompatibility of Mg–Zn–Zr alloys, J Mater Sci: Mater Med. 21 (2010) 2623–2635. https://doi.org/10.1007/s10856-010-4111-8.

[5] X.N. Gu, N. Li, Y.F. Zheng, L. Ruan, In vitro degradation performance and biological response of a Mg–Zn–Zr alloy, Materials Science and Engineering: B. 176 (2011) 1778–1784. https://doi.org/10.1016/j.mseb.2011.05.032.

[6] G.L. Makar, J. Kruger, Corrosion of magnesium, International Materials Reviews. 38 (1993) 138–153. https://doi.org/10.1179/imr.1993.38.3.138.

[7] I. Antoniac, M. Miculescu, V. Mănescu (Păltânea), A. Stere, P.H. Quan, G. Păltânea, A. Robu, K. Earar, Magnesium-Based Alloys Used in Orthopedic Surgery, Materials. 15 (2022) 1148. https://doi.org/10.3390/ma15031148.

[8] A. Szcześ, L. Hołysz, E. Chibowski, Synthesis of hydroxyapatite for biomedical applications, Advances in Colloid and Interface Science. 249 (2017) 321–330. https://doi.org/10.1016/j.cis.2017.04.007.

[9] L.T. Trang, N. Quang Cao, S. Hiromoto, M. O, E. Kobayashi, Formation and corrosion behavior of calcium phosphate coating layers on ZK60 alloy coated at various pH conditions by chemical conversion method, Surface and Coatings Technology. 444 (2022) 128639. https://doi.org/10.1016/j.surfcoat.2022.128639.

[10] L.T. Trang, H.V. Le, S. Hiromoto, O. Minho, E. Kobayashi, N.V. Nguyen, N.Q. Cao, In vitro cellular biocompatibility and in vivo degradation behavior of calcium phosphate-coated ZK60 magnesium alloy, Biomed. Mater. 18 (2023) 035003. https://doi.org/10.1088/1748-605X/acbf16.

[11] C.K. Mann, J.H. Yoe, Spectrophotometric Determination of Magnesium with Sodium 1-Azo-2-hydroxy-3-(2,4-dimethylcarboxanilido)-naphthalene-1′-(2-hydroxybenzene-5-sulfonate), Anal. Chem. 28 (1956) 202–205. https://doi.org/10.1021/ac60110a016.

[12] M. Tomozawa, S. Hiromoto, Growth mechanism of hydroxyapatite-coatings formed on pure magnesium and corrosion behavior of the coated magnesium, Applied Surface Science. 257 (2011) 8253–8257. https://doi.org/10.1016/j.apsusc.2011.04.087.

[13] D.N. Pham, S. Hiromoto, M. O, E. Kobayashi, Influence of substrate microstructure on hydroxyapatite coating and corrosion behavior of coated MgZn alloys, Surface and Coatings Technology. 421 (2021) 127414. https://doi.org/10.1016/j.surfcoat.2021.127414.

[14] M. Tomozawa, S. Hiromoto, Microstructure of hydroxyapatite- and octacalcium phosphate-coatings formed on magnesium by a hydrothermal treatment at various pH values, Acta Materialia. 59 (2011) 355–363. https://doi.org/10.1016/j.actamat.2010.09.041.

[15] N.Q. Cao, H.M. Le, K.M. Pham, N.V. Nguyen, S. Hiromoto, E. Kobayashi, In Vitro Corrosion and Cell Response of Hydroxyapatite Coated Mg Matrix in Situ Composites for Biodegradable Material Applications, Materials. 12 (2019) 3474. https://doi.org/10.3390/ma12213474.

[16] S. Hiromoto, K. Doi, Effect of polyethylene glycol modification on the corrosion behavior of hydroxyapatite-coated AZ31 Mg alloy under tensile deformation, Corrosion Science. 212 (2023) 110931. https://doi.org/10.1016/j.corsci.2022.110931.

[17] G. Song, A. Atrens, Understanding Magnesium Corrosion—A Framework for Improved Alloy Performance, Advanced Engineering Materials. 5 (2003) 837–858. https://doi.org/10.1002/adem.200310405.

[18] R.C. Phillips, J.R. Kish, Nature of Surface Film on Matrix Phase of Mg Alloy AZ80 Formed in Water, Corrosion. 69 (2013) 813–820. https://doi.org/10.5006/0938.

[19] D. Tie, F. Feyerabend, N. Hort, R. Willumeit, D. Hoeche, XPS Studies of Magnesium Surfaces after Exposure to Dulbecco's Modified Eagle Medium, Hank's Buffered Salt Solution, and Simulated Body Fluid, Advanced Engineering Materials. 12 (2010) B699–B704. https://doi.org/10.1002/adem.201080070.

[20] S. Zhang, Y. Bi, J. Li, Z. Wang, J. Yan, J. Song, H. Sheng, H. Guo, Y. Li, Biodegradation behavior of magnesium and ZK60 alloy in artificial urine and rat models, Bioactive Materials. 2 (2017) 53–62. https://doi.org/10.1016/j.bioactmat.2017.03.004.

[21] E.F. Morgan, G.U. Unnikrisnan, A.I. Hussein, Bone Mechanical Properties in Healthy and Diseased States, Annu Rev Biomed Eng. 20 (2018) 119–143. https://doi.org/10.1146/annurev-bioeng-062117-121139.

[22] F. Witte, J. Fischer, J. Nellesen, H.-A. Crostack, V. Kaese, A. Pisch, F. Beckmann, H. Windhagen, In vitro and in vivo corrosion measurements of magnesium alloys, Biomaterials. 27 (2006) 1013–1018. https://doi.org/10.1016/j.biomaterials.2005.07.037.

Chapter 5:

General Conclusion

This doctoral thesis focuses on investigating the effects of the calcium phosphate coating layer on three aspects (corrosion resistance, biocompatibility and mechanical integrity) of ZK60 alloy for orthopaedic applications.

The contents of each chapter in this thesis are summarized as the following:

Chapter 1: A literature review on the evolution of metallic biomaterials, development of Mg alloys for biomedical applications and their recent challenges has been discussed. Also, the strategies, purposes and research methodology of this thesis were stated.

Chapter 2: The formation and corrosion protectiveness of calcium phosphate coating layers depend on the coating conditions and the type of Mg substrate. Therefore, this study aimed to investigate the formation of the calcium phosphate coating layers on Mg-6mass% Zn-0.5mass%Zr (ZK60) alloy over a wide pH range of pH 6.5 to 10.2. Immersion tests with Mg^{2+} ion quantification were performed to study the degradation behavior of ZK60 coated with different types of calcium phosphate. It was found that the morphology and types of the calcium phosphate coating layers were controlled by pH conditions. At pH 6.5, an octacalcium phosphate (OCP) single phase layer was formed. At pH 7.0, an OCP+hydroxyapatite (HAp) mixture layer was formed. A HAp single layer and a HAp layer with an intermediate $Mg(OH)_2$ layer were formed at pH 7.8 and 10.2, respectively. The coating layers provided good corrosion protection but at different levels. The specimen coated at pH 7.8 possessed the best corrosion resistance. On this specimen, biocompatible hydroxyapatite (HAp) was deposited as a corrosion product after the immersion.

Chapter 3: To be successfully applied in clinical use, cell compatibility is necessary to be investigated because it indicates some extent of the reactions of human cells when they interact with the surface of the implant materials. However, the cell compatibility on different Ca-P layers coated on ZK60 alloy has seldom been investigated. Therefore, in this chapter, the effects of several Ca-P coatings formed at pH 6.5, 7.8 and 10.2 on cell behavior were examined by using an osteoblastic cell line MC3T3-E1. Osteoblasts could not survive on the samples that were uncoated and coated at pH 10.2; meanwhile, cells proliferated well on the samples coated at pH 6.5 and 7.8. Cells exhibited the best morphology on the sample coated at pH 7.8. The results also showed that the surface factors, including the coating type, morphology and corrosion protection, controlled strongly the cell adhesion, morphology and proliferation. Among those factors, the coating morphology is the most dominant factor. Later, a subcutaneous implantation in rabbits proved that the HAp coating formed at pH 7.8 reduced notably the degradation rate of ZK60 alloy. Pitting was the main cause of the implant degradation. The HAp coating also degraded during implantation. The results suggest the feasibility of biomedical use of the ZK60 alloy coated at pH 7.8.

Chapter 4: The influence of the HAp coating formed at pH 7.8 on the mechanical integrity of ZK60 alloy was studied. Mechanical strengths of the uncoated and coated samples deteriorated with an increase in the degradation time. Pitting was the main reason of this deterioration because deep pits acted as stress risers for crack initiation. The HAp coating reduced effectively the degradation rate of the alloy. Corrosion products were also an important factor to retard the degradation. Although the occurrence of pitting was slightly more severe on the coated sample than on the uncoated sample, the deterioration of the mechanical integrity of both types of the samples showed no differences. Thus, the HAp coating showed no meaningful effects on the mechanical integrity of ZK60 alloy.

Chapter 5: Summarization of the main findings in each chapter.

In conclusion, the results indicate that the HAp-coated ZK60 alloy, which was treated at pH 7.8 in the chemical conversion method, is a perspective biomaterial for temporary orthopaedic implantation.

Acknowledgement

First of all, I would like to express my deepest thanks to my supervisor, Assoc. Prof. Equo Kobayashi for his strong support, sound advice and guidance throughout my five-year program at the Tokyo Institute of Technology. In addition to academic support, Equo-sensei with his wife also care for and support me mentally so that I can enjoy my life in Japan and always be motivated forward. I deeply appreciated that.

I would like to express my sincere thanks to Dr. Sachiko Hiromoto at National Institute for Materials Science for kindly accepting me as an internship student and strongly support for my experiments, analysis data and manuscript's writing as well.

I would like to thank Prof. Tada, Prof. Fujii, Prof. Shi and Assoc. Prof. Muraishi for their comments and advice during my defence so that I can improve my thesis.

I also would like to thank Dr. Cao Quang Nguyen, Dr. Pham Ngoc Dinh and other members of Equo Kobayashi Laboratory for their kindness and help in both research and daily matters. Thanks to them, I enjoy and understand more about Japanese culture and people.

Last but not least, I would like thanks my beloved family and all of my friends. Thanks to them, I can go through the hardest times, get over the loneliness and be enjoyable.